



Optimisation of Noble Metal Nanoparticle Biosynthesis by both a Prokaryotic and Eukaryotic Host

Michael Kitching, B.sc.

PhD Thesis

Submitted September 25th, 2015

School of Biotechnology

Dublin City University

Under the Supervision of Prof. Paul Cahill and Dr. Enrico Marsili

September 2015

Declaration

I hereby certify that this material, which I now submit for assessment on the program of study leading to the award of Ph.D. is entirely my own work, that I have exercised reasonable care to ensure that the work is original and does not to the best of my knowledge breach any law of copyright, and has not been taken from the work of others save and to the extent that such work has been cited and acknowledged within the text of my work.

I.D. 58304271

Date:

Signed:

Science is a way of thinking much more than it is a body of knowledge. - Carl Sagan

Sometimes a scream is better than a thesis.- Manfred Eigen

As scientists, we step on the shoulders of science, building on the work that has come before us - aiming to inspire a new generation of young scientists to continue once we are gone- Stephen Hawking

Acknowledgements

I would like to acknowledge the Irish Research Council, for awarding me the IRC EMARK Initiative Scholarship to fund my PhD project.

I would like to thank my supervisors Prof. Paul Cahill, Dr. Enrico Marsili and Dr. Dermot Brougham for their supervision, guidance and patience throughout this project.

I would like to acknowledge my 3 month visit to the Singapore Centre on Life Science Engineering and Assistant Pro Cao Bin for his advice at the start of my project.

I would like to thank my colleague and friend, Monica Epifanio for her advice and support throughout my time in the laboratory.

I would like to thank my friends John Lawlor and Keith Connolly for their moral support, and to Les Lawlor for giving me the inspiration to obtain a PhD.

I would like to thank Claire Molony and Gillian Casey of the Vascular Biology and Therapeutics Laboratory, for teaching me how to isolate RNA and analyse by Q-RT PCR.

I would also like to thank Joseph Mackle, who taught me the basics of cell culture, microscopy and the helped me in the administration in the latter parts of my PhD.

I would like to thank Michael May, who trained me in the use of the SEM-EDX. I also would like to thank Patrick Chang and Brenton Cavanagh from the RCSI who guided me in the use of TEM.

Also I would like to thank Prof. Phillip Moriarty, and his PhD student Alex Summerfield, who allowed me to visit Nottingham University and helped with the atomic force microscopy of my nanoparticles and the data analysis. Also I would like to thank Emily Smith for analyzing my samples by XPS.

I'd like to thank our collaborators Saikumar Inguva, who advised on the sample preparation for XRD and who performed the XRD analyses of the nanoparticles, and Meghana Ramani who helped analyse the FTIR, XPS and XRD data.

Special thanks to my mother Carmel and my grandfather Michael for supporting me through my entire education both morally and financially, so I could reach this point.

Publications

Kitching, M., Meghana, R., and Marsili, E. (2014). Fungal Biosynthesis of Gold Nanoparticles. *Microbial Biotechnology*. DOI: 10.1111/1751-7915.12151 .

Epifanio, M., Inguva, S., Kitching, M., Mosnier, J.P. and Marsili, E. (2015). Effects of atmospheric air plasma treatment of graphite and carbon felt electrodes on the anodic current from *Shewanella* attached cells. *Bioelectrochemistry*. DOI: 10.1016/j.bioelechem.2015.03.011

Kitching, M., Butler, R. and Marsili, E. (2015). Microbial Bioelectrosynthesis of Hydrogen- Scale Up. *Microbial Biotechnology*. In preparation.

Kitching, M., Summerfield, A., Meghana, R., Epifanio, M., Brougham, D. and Marsili, E. Application of Electrochemical Potential to a *Shewanella* sp. Improves the Size Distribution of Biosynthesized Silver Nanoparticles. *RSC Advances*. In preparation.

Kitching, M., Cahill, P. and Marsili, E. Biosynthesis of Gold Nanoparticles by Vascular Cells. In preparation.

Susta, D., Kitching, M., Marsili, E. and Sujoy, D.K (2014). The Effect of Detergent on AuNPs synthesized by Fungal Protein Extract. In preparation.

Selected Presentations

Society for Industrial Microbiology and Biotechnology (SIMBT) Annual Meeting.

Hyatt Regency, St Louis, Missouri, USA. July 2014.

Title: They got potential: Bioelectrochemical Synthesis of Silver Nanoparticles by a *Shewanella* sp. Biofilm

Eurobiofilm 2013 Conference.

Ghent, Ghent University, September 2013.

Title: Bioelectrochemical Synthesis of Silver Nanoparticles by a *Shewanella oneidensis* MR1 biofilm.

Society for General Microbiology, Irish Regional Meeting.

University College Cork, November 2012.

Title: Biosynthesis of Gold Nanoparticles by *Shewanella loihica* PV4.

Abstract

The aims of this work were to explore novel biosynthetic methods to produce metal nanoparticles (MNPs) with short synthesis time and focussed particle size distribution. Current methods for the synthesis of MNPs use potentially hazardous compounds or extreme synthesis conditions, which raises concerns about their environmental impact, in-vivo toxicity and cost of synthesis. MNP biosynthesis in microorganisms have been attempted to lower the environmental impact and cost of nanoparticle and nanomaterials. Although microbial biosynthesis is inexpensive and does not involve the use of exogenous capping ligands/dispersing agents for MNP stabilization, it produces a nanoparticle population with a broad particle size distribution that is unsuitable for practical applications without further refinements.

In this thesis, the problems of wide size distribution and slow synthesis kinetics, in bacterial, fungal and mammalian cell hosts are addressed. The introduction (Chapter 1) provides a broad introduction on nanoscience and nanotechnology, including an overview of MNP chemical synthesis methods. Chapter 2 describe the material and experimental methods relevant to this work. Chapter 3 reports MNP biosynthesis in the dissimilatory metal reducing microorganism *Shewanella* sp., and discusses the effect of mild electrochemical reducing potential on the biosynthesis rate and silver nanoparticles (AgNPs) size and distribution in *Shewanella* biofilms grown on carbon electrodes. Results show that the optimal reducing potential is -0.2 V vs. Ag/AgCl. AgNPs synthesis was slower at higher potential (0 V vs. Ag/AgCl), while electroplating was the prevalent process at -0.4 vs. Ag/AgCl. The particle size at -0.2 V vs. Ag/AgCl was 61 ± 1 nm.

In Chapter 4, the mechanism of AuNP biosynthesis was studied in the fungi *Rhizopus oryzae*. Previous studies showed that redox enzymes located on the cell surface reduce Au^{3+} ions to AuNPs. A purified cell surface protein extract was used to generate small, uniform AuNPs. Since protein extraction may influence protein structure and the resulting AuNP size and shape, the modulatory effects of DTT, SDS and Triton X-100 extraction buffers on protein extraction and AuNP biosynthesis by the protein extracts were examined. Results show that 1% v/v Triton X-100 produces AuNPs with the best size distribution (19 ± 1 nm), crystallinity and antimicrobial activity.

Finally, the biosynthesis of gold nanoparticles (AuNPs) using mammalian vascular endothelial and smooth muscle cells was examined *in vitro* in Chapter 5. Cell culture conditions such as phosphate buffer and foetal bovine serum (FBS) concentration were optimised as well as initial Au concentration. The AuNPs produced under optimal conditions were semi crystalline in nature. The average particle sizes were $23 \pm 2\text{nm}$ for endothelial cells and $23 \pm 4\text{nm}$ for smooth muscle cells, respectively. Results suggest that the production of reactive oxygen species during oxidative stress reduced the Au^{3+} ions, although there may also be some Au^{3+} reducing activity in the secretome.

Taken together, these studies suggest that MNPs size distribution is an inherent problem of the biosynthetic process, and that MNP mean size is influenced by reducing potential, protein structure, and cell type. Crystallinity of the MNPs is dependent on the temperature of the synthesis, rather than the cell type, reducing potential or protein structure. Further the protein capping ligands uncovered in this study is predominantly proteins, although their identity is not yet clear. The use of fungal protein extracts is the most ideal strategy for MNP biosynthesis, specifically Triton X-100 protein cell extract, due to the low cost of synthesis compared to the mammalian cell culture, smaller size compared to the bioelectrochemical synthesis and repeatability. Bioelectrochemical synthesis is a promising alternative, however further optimisation is required to lower MNP size and size distribution. Bovine aortic smooth muscle cells produced a high concentration of AuNPs, may be an ideal eukaryotic host for the production of biocompatible AuNPs for in-vivo use, however a comprehensive toxicity study of these AuNPs is required.

Acronyms

AHL	Acyl-homoserine lactone
AMC	Activated methyl cycle
AgNP	Silver nanoparticle
AuNP	Gold nanoparticle
AuNR	Gold nanorod
BAEC	Bovine aortic endothelial cell
BASMC	Bovine aortic smooth muscle cell
BES	Bioelectrochemical synthesis
BSO	Buthionine sulphoximine
CA	Chronoamperometry
CC	Carbon cloth
CE	Columbic efficiency
CF	Carbon felt
CNT	Carbon Nanotube
CV	Cyclic voltammetry
DAPI	4',6-diamidino-2-phenylindole
DET	Direct electron transfer
DHE	Dihydro-ethidium
DHR	Dihydrorhodamine
DI	Deionised
DMRB	Dissimilar metal reducing bacteria
DPD	4,5-dihydroxy-2,3-pentanedione
DPV	Differential Pulse Voltammetry
EC	Electrochemical cell
ECM	Extracellular matrix
EDX	Energy dispersive x-ray analysis
EET	Extracellular Electron Transfer
EPS	Extracellular polymeric matrix
HE	Hydroethidine
FBS	Fetal bovine serum
Fcc	Face centred cube
FTIR	Fourier transform infra-red spectroscopy
GSH	Reduced glutathione

GSSG	Oxidised glutathione
HCAEC	Human coronary artery endothelial cells
HCY	Homocysteine
HVSMC	Human vascular smooth muscle cells
HO-1	Heme-oxygenase-1
HRTEM	High resolution transmission electron microscopy
ITO	Indium Tin Oxide
mAb	Monoclonal antibody
LA	Luria agar
LB	Luria Broth
L-NAME	N ^G -nitro- L-arginine methyl ester
MET	Mediated electron transfer
MFC	Microbial fuel cell
MIC	Minimum inhibitory concentration
MNP	Metal Nanoparticle
MnSOD	Manganese superoxide dismutase
<i>mtrCAB</i>	Metal respiratory complex CAB
MWCNT	Multi walled carbon nanotube
NADH	Nicotinamide adenine dinucleotide
NADPH	Nicotinamide adenine dinucleotide phosphate
NO	Nitric oxide
<i>omcA</i>	Outer membrane cytochrome A
PAEC	Porcine aortic endothelial cells
PBS	Phosphate buffered saline solution
P/S	Penicillin/Streptomycin
PVP	poly(vinylpyrrolidone)
ROS	Reactive oxygen species
SAED	Selected area electron diffraction
SDS	Sodium dodecyl sulphate
SEM	Scanning electron microscope
siRNA	Small interfering RNA
SPR	Surface plasmon resonance
SRH	S-ribosylhomocysteine
SWCNT	Single Wall Carbon Nanotube

TEM	Transmission Electron Microscopy
TNF α	Tumour necrosis factor α
VEC	Vascular endothelial cell
VSMC	Vascular smooth muscle cell
XANES	X-ray absorption near edge structure analysis
XPS	X-ray photoelectron spectroscopy
XRD	X-ray diffraction spectroscopy

Units and Constants

% v/v	Concentration volume per volume
% w/w	Concentration weight per weight
% w/v	Concentration weight per volume
°C	Degrees Celsius
°C.min ⁻¹	Degree per minute
C	Coulombs
cm	Centimetres
F	Faraday Constant (96,485 C/mole)
g/L	Grams per litre
mA	MilliAmps
ml	Millilitres
mV	Millivolts
h	Hours
µA	Microamps
mA	Milliamps
mg/ml	Milligrams per millilitre
mM	Millimolar
M	Molar
min	Minutes
ng	Nanogram
nm	Nanometres
nM	Nanomolar
OD _{xxxnm}	Optical density at xxx nm
Ω	Ohms
s	Seconds
V	Volts

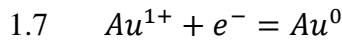
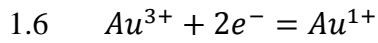
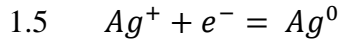
Chemical Equations and Formula

$$1.1 \quad D_H = \frac{kT}{6\pi\eta D}$$

$$1.2 \quad n\lambda = 2d\sin\theta$$

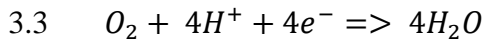
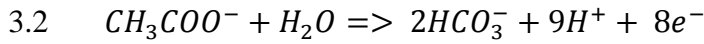
$$1.3 \quad D = \frac{0.9\lambda}{\beta_{hkl}\cos\theta}$$

$$1.4 \quad \beta_{hkl} = \sqrt{(\beta_{hkl}^{meas})^2 - (\beta_{hkl}^{instr})^2}$$



$$2.1 \quad \text{Cell density} = \text{Ave. Cell count} \times 10,000 \times \text{dilution factor}$$

$$3.1 \quad OmcA_{bound} = \left[\frac{[OmcA_{free}^n]}{K_d + [OmcA_{free}^n]} \right] \times \text{Max} + \text{Min}$$



$$3.4 \quad J = \frac{D_A}{\gamma} \Delta A$$

$$3.5 \quad E = E_f^0 \left(\frac{A}{B} \right) + \frac{RT}{F} \ln \frac{[B]_0}{[A]_0}$$

$$3.6 \quad e^- = \frac{C}{F}$$

$$4.1 \quad Abs = 0.539(\text{Protein Conc.}) + 0.1178$$

$$5.1 \quad Eff. = \frac{\#Cy5 \text{ containing cells}}{\#DAPI \text{ stained Nuclei}} \times 100\%$$

Contents

List of Figures	19
Chapter 1: Introduction	23
1.1 Nanoscience	23
1.2 Metal Nanoparticles.....	28
1.2.1 Gold Nanoparticles.....	28
1.1.2 Silver Nanoparticles	31
1.2 Metal Nanoparticle Characterisation.....	33
1.2.1 UV- visible Spectrophotometry.....	33
1.2.2 Dynamic Light Scattering	34
1.2.3 Transmission Electron Microscopy	34
1.2.4 Scanning Electron Microscopy	35
1.2.5 Atomic Force Microscopy	36
1.2.5 Energy Dispersive X-Ray Spectroscopy	37
1.2.6 X-ray Diffraction	38
1.2.7 X-ray Photoelectron Spectroscopy	40
1.3 Conventional Synthetic Methods for the Production of Metal Nanoparticles.....	41
1.3.1 Lithography	41
1.3.2 Inert Gas Condensation.....	42
1.3.3 Electrochemical Oxidation	42
1.3.4 Laser Ablation	42
1.3.5 Chemical Reduction	43
1.3.6 Sol-gel Synthesis.....	44
1.4 Biosynthesis of Metal Nanoparticles	44
1.4.1 Bioaccumulation/Biosorption	48
1.4.2 Metal ion Induced Changes in Gene and Protein Expression	48
1.4.3 Bioreduction.....	49
1.4.4 Nanocrystal Formation and Capping	52
1.5 Problems with Metal Nanoparticle Biosynthesis.....	59
1.6 Aims of the thesis.....	60

Chapter 2: Materials and Methods	62
2.1 Cell Culture and Biomass Preparation	62
2.1.1 Microbial Cell Culture.....	62
2.1.2 Establishment of the Shewanella Biofilm	63
2.1.3 Fungal Cell Cultivation and Protein Extraction	64
2.1.5 Mammalian Cell Culture	64
2.1.6 Mammalian Cell Subculture.....	66
2.1.7 Cell counting	66
2.1.7 Long Term Cell Storage	67
2.2 Electrochemistry	68
2.2.1 Electrochemical Cell Set up.....	69
2.2.2 Cyclic Voltammetry	70
2.2.3 Differential Pulse Voltammetry	71
2.2.4 Chronoamperometry	71
2.3 Nanoparticle Biosynthesis.....	71
2.3.1 Bioelectrochemical Synthesis of Silver Nanoparticles	71
2.3.2 Fungal Cell Surface Protein Synthesis of AuNPs	72
2.3.3 Mammalian Cell AuNP Biosynthesis	72
2.4 MNP Characterisation.....	73
2.4.1 Isolation of MNPs.....	73
2.4.2 U.V. visible spectrophotometry	73
2.4.3 Dynamic Light Scattering	74
2.4.4 Transmission Electron Microscopy	74
2.4.5 Atomic Force Microscopy.....	74
2.4.6 High resolution TEM and Selected area electron diffraction.....	75
2.4.7 Base Piranha etching.....	75
2.4.8 Fourier transformed infra-red spectroscopy (FTIR).....	75
2.5 Cell Analysis and Biochemical Analysis	75
2.5.1 Biofilm Fixation and Dehydration	76
2.5.2 Biofilm Carbon Coating.....	76
2.5.3 Scanning electron microscopy and Energy Diffraction X-ray Spectroscopy.....	76
2.5.4 Phase Contrast Microscopy.....	76
2.5.5 Fluorescent Microscopy	77
2.5.6 Oxidative stress assay	77

2.5.7	BCA Protein Assay	77
2.5.8	Protein concentrator.....	78
2.6	MNP activity.....	78
2.6.1	Anti-bacterial assay.....	78
2.7	<i>Data Analysis</i>	79
2.8	Media Recipes.....	79
2.8.1	Sterilisation and Glassware preparation.....	79
2.8.2	Luria Broth/Agar.....	80
2.8.3	M9 Medium.....	81
2.8.4	Modified M1 medium	81
2.8.5	Potato Dextrose Broth/Agar	82
2.8.6	100X Amino acid stock.....	82
2.8.7	100 X Vitamin Stock	83
2.8.8	100 X Mineral stock.....	83
2.8.9	5X M9 salt stock	84
Chapter 3: Bioelectrochemical Synthesis of Silver Nanoparticles.....		85
3.1	Introduction	85
3.1.1	Electroactive Bacteria	85
3.1.2	Extracellular Electron Transfer.....	86
3.1.3	Biofilm Formation	90
3.1.4	Bioelectrochemistry and Bioelectrochemical Reactors	93
3.1.5	Electrochemical Cell Set Up	93
3.1.6	Introduction Electrochemical Methods	98
3.1.7	Bioelectrochemical Synthesis.....	100
3.1.8	Aim of Chapter	101
3.2	Materials and Methods.....	101
3.2.1	Establishment of <i>Shewanella</i> Biofilm.....	101
3.2.2	Electrochemical Analysis of Biofilm	101
3.2.3	Bioelectrochemical Synthesis of Silver Nanoparticles	101
3.2.4	Electrode Analysis.....	102
3.3	Results.....	102
3.3.1	Biofilm Establishment	102
3.3.2	Silver Nanoparticle Bioelectrochemical Synthesis	106

3.3.3	Silver Nanoparticle Analysis.....	110
3.3.4	Biofilm Analysis	116
3.4	Discussion.....	118
3.5	Conclusions	121
3.6	Future work.....	122
Chapter 4:	Fungal Protein Extraction of Gold Nanoparticles	123
4.1	Introduction	123
4.1.1	Bacteria vs Fungi	123
4.1.2	<i>Rhizopus oryzae</i>	124
4.1.3	Protein Extraction	125
4.1.4	Aims.....	126
4.2	Materials and Methods.....	126
4.2.1	Fungal Cell Biomass Cultivation and Protein Extraction	126
4.2.2	Gold Nanoparticle Biosynthesis	126
4.2.3	Gold Nanoparticle Analysis	126
4.2.4	Antimicrobial Activity.....	127
4.3	Results.....	127
4.3.1	Protein Extraction	127
4.3.2	Gold Nanoparticle Synthesis	128
4.3.4	Gold Nanoparticle Analysis	128
4.35	Antimicrobial Activity of the Gold Nanoparticles	132
4.4	Discussion.....	133
4.5	Conclusions	136
4.6	Future Study.....	137
Chapter 5:	Vascular Cell Biosynthesis of Gold Nanoparticle.....	138
5.1	Introduction	138
5.1.1	Arterial Structure	138
5.1.2	Biosynthesis of AuNPs in Mammalian Cells, <i>in-vitro</i> and <i>in-vivo</i>	139
5.1.3	Oxidative Stress Response by Vascular Cells	140
5.1.6	Aims.....	144
5.2	Materials and Methods.....	144
5.2.1	Cell Culture.....	144

5.2.2	AuNP Biosynthesis.....	144
5.2.3	AuNP Isolation and Analysis.....	144
5.2.4	Pre-treatments.....	145
5.3	Results:.....	145
5.3.1	Optimisation.....	145
4.3.2	AuNP Characterisation	155
4.3.3	Mechanism of Synthesis	158
5.4	Discussion.....	161
5.5	Conclusions	163
5.6	Future Work.....	163
Chapter 6	Concluding Remarks.....	164
	Bibliography	166
	Appendices.....	184
	Appendix 1 Visit to Singapore Centre on Life Science Engineering	185
	Appendix 2 Materials and Regents	187

List of Figures

- 1.1 Graphene, precursor of carbonaceous nanomaterials such as fullerenes, single walled and multi walled carbon nanotubes
- 1.2 Various DNA structures
- 1.3 Different morphology of NPs, using AuNPs as an example
- 1.4 Visual demonstration of the size tunable properties of nanoparticles.
- 1.5 Multivalent interaction between a Vancomycin capped AuNP and a vancomycin resistant strain of *E. coli*.
- 1.6 Physical properties of AuNPs and illustration of AuNP-based detection systems
- 1.7 Processes involved in the synthesis of targeted peptide functionalized gold nanorods with PAA modification and the selective photothermal therapy
- 1.8 Absorption spectra of AuNPs and AgNPs.
- 1.9 Sample TEM of AuNPs prepared by *Rhizopus oryzae* protein extract
- 1.10 Sample SEM of Biofilm
- 1.11 Sample EDX of AuNPs
- 1.12 Sample XRD of AuNPs
- 1.13 Modes of operation for atomic force microscopy
- 1.14 X-ray scattering from atomic planes
- 1.15 Fabrication of micro discs using optical lithography
- 1.16 Schematic of the inert gas condensation instrument
- 1.17 Schematic formation of tin sulphide nanoparticles (SnS) by laser ablation
- 1.18 TEM image of biosynthesized magnetite nanoparticles arranged in magnetosomes in a magnetotactic bacterium and SEM of coccolithophoric algae showing calcite plate exoskeleton.
- 1.19 Antibacterial mechanisms of metal toxicity. (a) Metal ion inactivates enzyme through chemical modification, (b) up regulation of ROS (c) impairment of membrane function, (d) interference of nutrient uptake and (e) genotoxicity through DNA oxidation causing double strand breaks.
- 1.20 Defensive mechanism of microbial cells against heavy metals
- 1.21 AuNPs synthesized by *S. oneidensis*, AgNP synthesized by *S. oneidensis*, PdNPs synthesized by *D. desulfuricans* and Pd-AuNPs synthesized by *S. oneidensis*.
- 1.22 Mechanisms of Au reduction by *R. oryzae*

- 1.23 Proposed mechanism of AgNP and AuNP formation
- 1.24 Proposed mechanism of (a) AgNP formation and (b) AuNP formation in *Stenotrophomonas maltophilia*
- 2.1 Photograph of laminar flow hood used for microbial cell work.
- 2.2 Laminar flow hood used for mammalian cell culture experiments
- 2.3 Photograph of culture vessels (a) 6 well flask and (b) T75 flask
- 2.4 Illustration of cell counting grid of a haemocytometer
- 2.5 Electrochemical cell set up used for *Shewanella* sp. biofilm growth
- 2.6 *S. oneidensis* and *E. coli* grown on LB supplemented with 0.1g.L⁻¹ iron citrate
- 3.1 Mechanism of EET for *S. oneidensis*.
- 3.2 Diagram of the omcA/mtrcA cytochrome complex in *S. oneidensis*
- 3.3 Mediated electron transfer by *S. oneidensis*
- 3.4 SEM images of *S. oneidensis* nanowires and proposed structural model for these nanowires.
- 3.5 Illustration of the general mechanism of biofilm formation
- 3.6 Model of NO induction of biofilm formation in *S. oneidensis*
- 3.7 Operation principles of a MFC
- 3.8 Electrochemical cell set up for *Shewanella* sp. biofilm growth
- 3.9 Schematics of electrochemical designs used in BES reports. (a) Dual chamber electrochemical cell fitted with proton exchange membrane, (b) H type dual chamber membrane less bioelectrochemical reactor and (c) single chamber electrochemical reactor.
- 3.10 Electrochemical analysis of sterile electrochemical cell containing M1 growth medium
- 3.11 Chronamperometry, cyclic voltammetry and differential pulse voltammetry of *S. oneidensis* biofilm immediately and 24 hours post inoculation into a electrochemical cell.
- 3.12 DPV of biofilm after removal of spent media and injection of 100 mM HEPES, and prior to 1mM Ag addition
- 3.13 UV-visible spectra of the AgNPs produced by *S. oneidensis* MR-1 biofilms and abiotic control
- 3.14 UV-visible spectra of 100mM HEPES buffer incubated at 30 °C with 1 mM AgNO₃ for 100 min.

- 3.15 UV-visible spectra of the supernatant of a 2 OD_{600 nm} planktonic cell culture. incubated with 100 mM HEPES buffer, spiked with 1 mM AgNO₃
- 3.16 Charge transfer
- 3.17 Atomic force microscopy images and size distributions of AgNPs
- 3.18 Transmission electron images and size distributions of AgNPs
- 3.19 XRD analysis of AgNP
- 3.20 Wide scan XPS analysis of AgNP
- 3.21 High resolution XPS analysis of AgNP synthesized by *S. oneidensis* biofilms grown on a carbon felt electrode for 24 hours poised at various fixed potentials for 100 minutes at 30 °C and 150 rpm.
- 3.22 SEM images (1k X) of *S. oneidensis* biofilm grown on a carbon felt electrode
- 3.23 Relative weight of Ag deposited (measured by EDX) on CF electrode with biofilm (biotic) and without biofilm (abiotic) after 100 min
- 4.1 Mechanisms of Au reduction by *R. oryzae*
- 4.2 Sample BCA Standard curve
- 4.3 UV-Visible spectrophotometry of AuNPs synthesized by *R. oryzae* cell surface extracts
- 4.4 XRD of AuNPs synthesized by *R. oryzae* cell surface extracts
- 4.5 TEM, SAED and HR-TEM of AuNPs synthesized by fungal cell protein extracted prepared by various detergents.
- 4.6 Histogram of AuNP sizes produced by the different protein extracts
- 4.7 Growth curve of *E. coli* in M9 medium with 0.1 OD of AuNPs prepared by various protein extracts.
- 5.1 Arterial structure
- 5.2 General scheme of the response of VECs to oxidative stress imposed by H₂O₂
- 5.3 Glutathione synthesis and recycling
- 5.4 Media optimisation.
- 5.5 Effect of FBS concentration on AuNPs biosynthesis
- 5.6 Optimisation of Au for AuNP biosynthesis
- 5.7 Effect of Au(III) ions on BAEC cell lines.
- 5.8 Effect of Au(III) ions on BASMC cell lines.
- 5.9 Addition of 1 mM Ca and Mg to BAEC and BASMC culture.
- 5.10 Examination of cell associated AuNPs produced by BAECs and BASMCs.

- 5.11 Effect of the addition of 1 mM Ca and Mg ions to the AuNP biosynthesis experiment, BAEC.
- 5.12 Effect of the addition of 1 mM Ca and Mg ions to the AuNP biosynthesis experiment, BASMC.
- 5.13 TEM, SAED and HR-TEM of AuNPs produced by BASMCs and BAEC
- 5.14 Histogram of AuNP particle sizes
- 5.15 XRD of AuNPs for BAECs and BASMCS
- 5.16 FTIR of powered AuNPs produced by BAECs and BASMCs
- 5.17 Effect of salt concentration on AuNP biosynthesis by BAECs and BASMCs
- 5.18 Oxidative stress assay of Au against BAEC and BASMCs
- 5.19 Effect of BSO pretreatment on AuNP biosynthesis by BAECs and BASMCs
- 5.20 Effect of H₂O₂ pretreatment of AuNP biosynthesis by BAEC and BASMC

Chapter 1: Introduction

1.1 Nanoscience

Nanoscience focuses on the design, synthesis and utilization of nanomaterials. Nanomaterials do not have a strict definition in the literature, but is generally accepted that they are structures that possess at least one dimension under 100nm. Nanoscience is an interdisciplinary field of study that encompasses physics, chemistry and biology. Physicists are interested in the atomic and molecular properties of nanomaterials and their interaction with photons. Chemists are interested in the catalytic properties of nanomaterials such as gold nanoparticles. Biologists are especially interested as the components of cells such as the flagella, mtrCAB-omcA cytochrome complex in *Shewanella* sp. and gap junctions can be considered as nanomaterials under this definition (Whitesides, 2005). Further, biomedical researchers are interested in incorporating nanomaterials in the design of therapeutics and diagnostics as their small size allows the cell to uptake the nanomaterial for drug delivery and *in-vivo* or *in-vitro* imaging (Wang et al., 2009).

The precise origin of nanoscience is not known, Richard Feynman's inspirational lecture, *There's Plenty of Room at the Bottom*, to the American Physical Society in 1959 has made him the godfather of nanotechnology. Since then, research and commercial application of nanotechnology have been made possible due to the increased ability of researchers to analyse and manipulate matter at the nanoscale, using devices such as atomic force microscopes, scanning tunnelling microscopes and electron microscopes, among others. One famous example of nanoscience is the work of Don Eiglers group at IBM in the early nineties, who were able to move single Xe atoms at low temperatures to spell out the name of the company using scanning probe microscopy (Fig. 1.1).

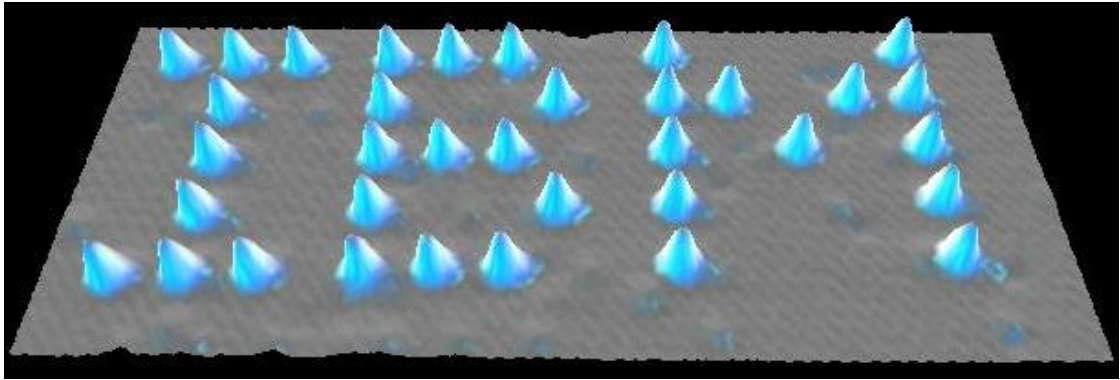


Figure 1.1: Manipulating matter at the nanoscale, Xe atoms arranged by scanning probe microscope by Don Eiglers group in IBM (idol.union.edu).

Carbonaceous nanomaterials, as the name implies, are materials that are comprised of a carbon backbone. The first characterised nanomaterials are fullerenes, also known as C_{60} or colloquially as “buckyballs”, where carbon atoms are arranged into a cage-like fused ring structure (Whitesides, 2005). Although fullerenes have been to date a disappointment in terms of applications, other carbonaceous nanomaterials show promises. Graphene is a flat monolayer of carbon atoms, which Fig. 1.2 shows is the building block of all carbon nanomaterials (Geim and Novoselov, 2007). Graphene has gained research interest due to its excellent electrical conductivity, mechanical strength and ease of functionalization (Shao et al., 2010). Carbon Nanotubes (CNTs) are layers of graphene wrapped up in cylindrical structure, and can be composed of a single layer, known as single wall CNTs (SWCNTs) or multiple layers of graphene known as multi walled CNT (MWCNTs) (Dai, 2002). As CNTs possess semiconductor properties at room temperature and can be easily functionalised, CNTs have been explored in recent years for potential application in nanoelectronics (Dai, 2002) or to functionalise electrodes for increased current output in microbial fuel cells (MFCs) (Kipf et al., 2013).

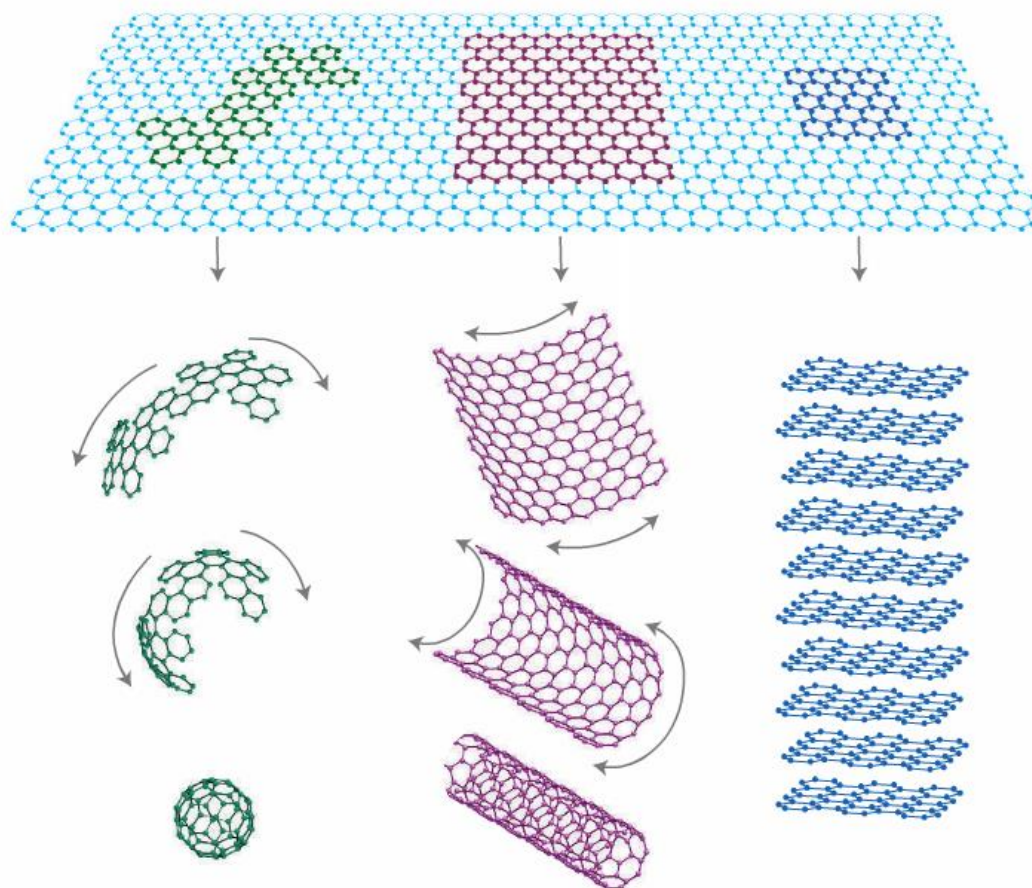


Figure 1.2: Graphene, a flat monolayer of carbon atoms, is used as a precursor to synthesize other carbonaceous nanomaterials such as fullerenes, which are spheres of carbon atoms (lower left) and carbon nanotubes (CNTs), which are open ended cylinders of carbon atoms which may be composed of one layer, which is termed single wall CNTs (lower middle) and multiple layers, termed multi walled CNTs (lower right) (Geim and Novoselov, 2007).

Our ability to study and manipulate nucleic acid has led to the use of DNA to construct functional nanomaterials, by the synthesis of a single DNA strand, which can self-assemble into structures, depending on the DNA sequence. The first DNA structures were relatively flexible branched junction structures and topological structures, which progressed to 2D lattice structures which are referred to as DNA tiles, which then could be used to assemble higher order periodic and aperiodic lattices and nanotubes. Fig 1.3 shows the various structures produced by folding single stranded DNA molecules to create 2D and 3D nanostructures, which is known as “DNA origami”.

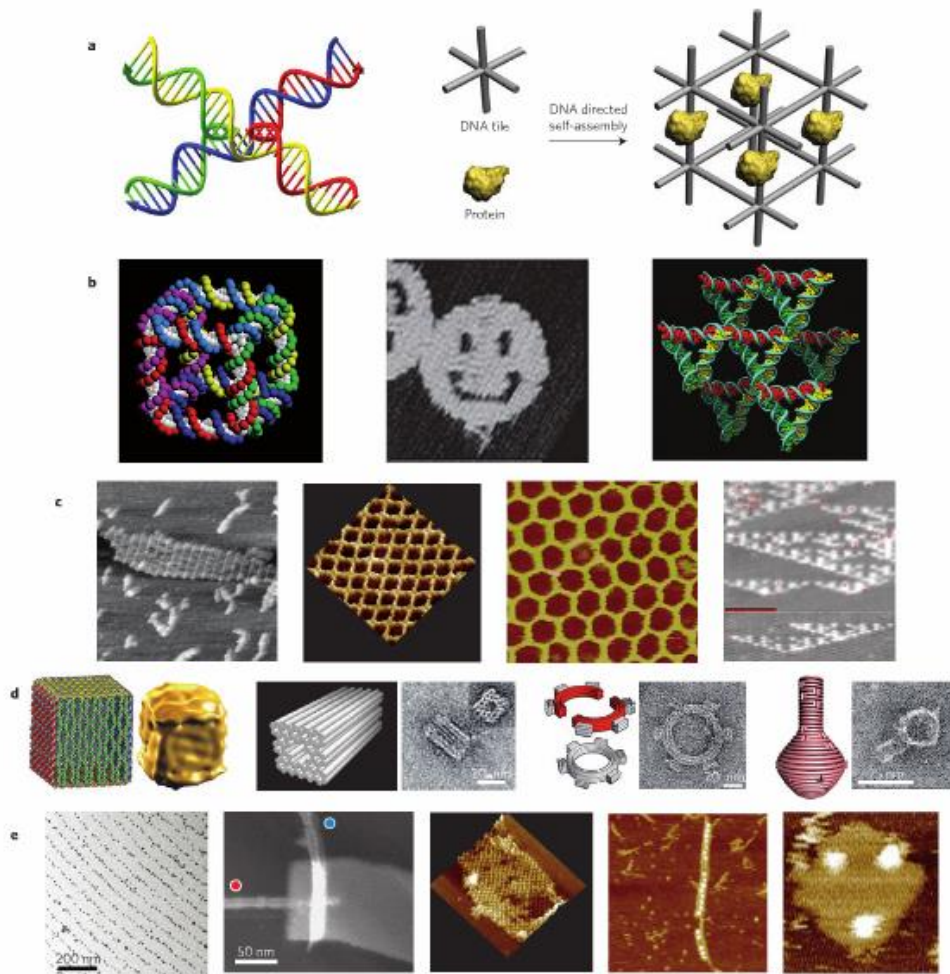


Figure 1.3: Various DNA structures, (a) immobile DNA junctions (left) to build 3D scaffolds that could be used to organize proteins (right) (b) first wire frame 3D cube (left), DNA origami (centre) and a 3D periodic structure composed of tensegrity triangles (right). (c) DNA periodic arrays composed of double-crossover tiles (left), 4×4 tiles (centre left), three-point star tiles (centre right) and double-crossover-tile-based algorithmic assembly of Sierpinski triangles (right). (d) Three-dimensional DNA origami: a hollow box (left pair of images), a multi-layer square nut (centre left pair), a square-toothed gear (centre right pair) and a nanofask (right pair). (e), DNA nanostructure-directed patterning of hetero-elements: double-crossover tiles for the organization of gold nanoparticle arrays (left), DNA origami for the assembly of carbon nanotubes (centre left), biotin–streptavidin protein patterning of 4×4 tiles (centre), aptamer- directed assembly of thrombin arrays on triple crossover tiles (centre right), and Snap-tag and His-tag mediated orthogonal decoration of DNA origami (right) (Pinheiro et al., 2011) .

However, the cost of DNA synthesis, the mechanically fragile nature of long DNA strands needed, and lack of analytical tools to detect defects in large DNA assemblies continues to be a challenge (Pinheiro et al., 2011) .

Nanoparticles (NPs) are the simplest nanomaterials. They can be composed of a metal-oxides (ceramic), semi-conductor materials, e.g. CdS, CdSe, silicon (quantum dots) noble metals such as gold, silver or platinum or composites such as gold-silver, gold palladium or gold magnetite and these take on a wide range of morphologies as seen in Fig. 1.4.

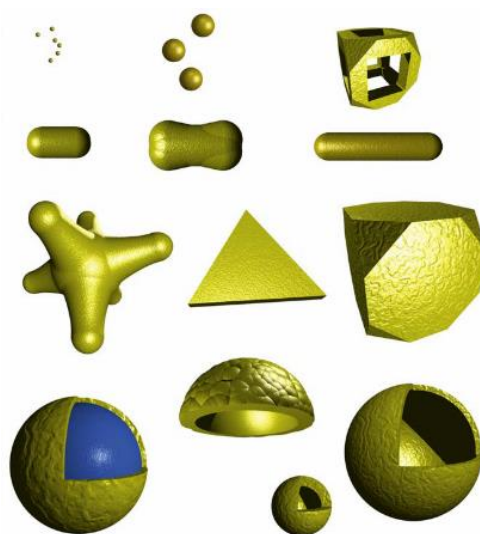


Figure 1.4: Different morphology of NPs, using AuNPs as an example. From top row left to right, small nanospheres (5nm), nanospheres (15nm), nanocages, short nanorods, “dog bone” nanorods, long nanorods, nanostars, nanotriangles, polyhedral, nanoshells with inert core, semi nanoshells and hollow capsules (Pissuwan et al., 2010)

In this project, we focus on the synthesis of metal nanoparticles (MNPs), as their unique size dependent optical properties, i.e. surface plasmon resonance (SPR), and their surface chemistry can be easily modified, allowing them to have a wide variety of application in research, commercial and industrial settings.

1.2 Metal Nanoparticles

Nanoparticles behave as a whole unit in terms of its transport and properties. Metal nanoparticles (MNPs), are nanometer sized assemblies of one or multiple metals. MNPs have size tuneable physicochemical properties, e.g., absorption and emission wavelength of semi-conductor NPs (quantum dots, QDs) (Fig 1.5), this arises from the quantum confinement of electrons, where size of the nanoparticle is equivalent to the de Broglie wavelength of the electron wave function (Andersen et al, 2002).



Figure 1.5: Visual demonstration of the size tuneable properties of nanoparticles. In this case the photo-fluorescent wavelength of CdS quantum dots can be altered by changing the nanoparticle diameter. The emission wavelength of the CdS NP can be increased from blue to red by decreasing nanoparticle size from $\sim 2\text{nm}$ to $\sim 6\text{nm}$ (left to right in Figure), which covers the visible range of the electromagnetic spectrum (nanotech-now.com).

Further, MNPs offer greater catalytic activity than their corresponding bulk materials due to the larger surface area to volume ratio. MNPs synthesized to date include gold, silver, palladium, platinum and composites such as gold-silver, gold-palladium to name a few examples. This section will focus on MNPs relevant to this thesis.

1.2.1 Gold Nanoparticles

Gold nanoparticles (AuNPs) are resistant to oxidation, biocompatible and stable in a wide range of environmental conditions, and so have been studied for therapeutic uses such as drug delivery and photo-thermal therapy due to their low cytotoxicity and ease of which their surface can be functionalised.

AuNP functionalization can occur through addition of a suitable ligand to the reaction vessel or the molecule may passively absorb on to the AuNP surface due to electrostatic interactions (Zhou et al., 2009). Antibiotics such as ciprofloxacin, streptomycin, gentamicin, neomycin, ampicillin, kanamycin and vancomycin have been conjugated to AuNPs (Pissuwan et al., 2010). Functionalization of antibiotics to AuNPs improves their activity. The minimum inhibitory concentration (MIC), i.e., the lowest concentration of an antimicrobial substance that inhibits microbial growth, of vancomycin to vancomycin resistant *Enterococcus faecalis* was lowered from $>128\mu\text{g/mL}$ to $4\mu\text{g/mL}$, when vancomycin was conjugated to AuNPs (Gu et al., 2003). This improvement in the antibiotic efficiency is likely due to the increased local concentration of vancomycin as shown in Fig.1.6.

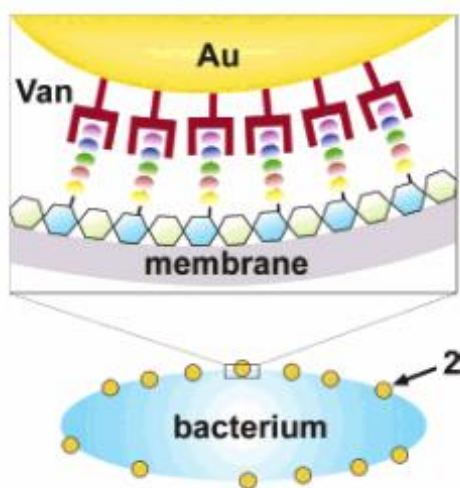


Figure 1.6: Multivalent interaction between Van-capped AuNPs and vancomycin resistant strain of *E. coli*. (2) Van-capped AuNPs on bacterial cell surface (Gu et al., 2003).

AuNPs physicochemical properties, such as surface plasmon resonance (SPR), conductivity and redox behaviour can be altered due to change in surrounding chemical environment. For example, the binding of an analyte to a specific receptor bound to the AuNP surface, such as an antigen binding to an antibody (Saha et al., 2012). This has lead researchers to utilise AuNPs as transducing agents in biological and chemical sensor technology (Fig. 1.7).

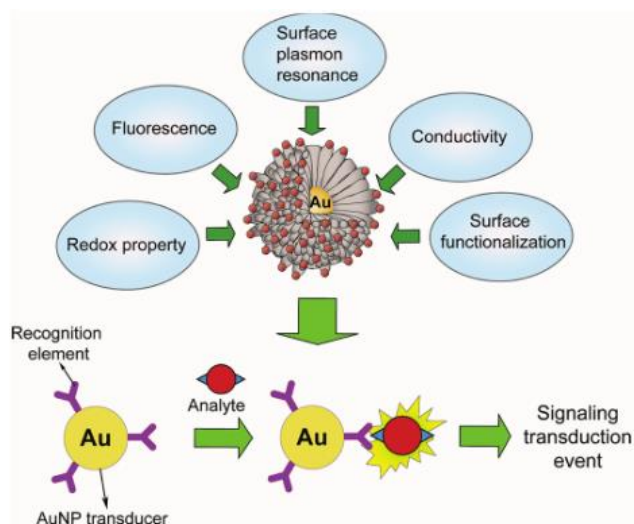


Figure 1.7: Physical properties of AuNPs and illustration of a AuNP-based detection system (Saha et al., 2012).

AuNPs have been incorporated in sensor design to detect alkali and alkaline earth metal ions, heavy metals, small organic molecules, detection of oligonucleotides and proteins with excellent sensitivity. For example when AuNPs-anti protein A IgG antibody conjugate were utilised as the detection reagent of an immunochromatographic strip, it was able to detect 25ng.mL^{-1} of protein A in less than 10 min (Huang, 2007). It is possible to detect as low as 50 fM of methicillin resistant *Staphylococcus aureus* (MRSA) DNA using an oligonucleotide specific for MRSA labelled AuNP (Storhoff et al., 2004).

The phenomenon of SPR has also been exploited in cancer therapy, as upon excitation, the surface plasmon release energy as heat. When concentrated on a target cell, such as a cancer cell, exciting the AuNPs causes localised heating which induces cell death. For this application, Au nanorods (AuNRs) are preferred due to the longer wavelength of the SPR, which means that the incident light can penetrate deeper into tissue. When illuminated with NIR, AuNRs increase the temperature of cell culture media by $15\text{ }^{\circ}\text{C}$ for 38nm sized AuNRs and $\sim 35\text{ }^{\circ}\text{C}$ for AuNRs that were 28 and 17 nm in size, respectively. Upon illumination with NIR laser irradiation for 2 minutes, the viability of HSC cells treated with AuNPs dropped from 100% to 20% and 30% for AuNRs with a length of 28 and 17 nm, respectively, while 38 nm AuNRs did not affect cell viability, possibly due to the lower temperature change

(Mackey et al., 2014). AuNRs labelled with anti Her-2 mAb were used for the photothermal therapy against a human malignant breast cancer (SK-BR-3) cell line triggered necrosis after 30 minutes of NIR treatment. The authors used a human hepatic tumor cell line (HepG2) as a control to show the specificity of the treatment (Wang et al., 2012).

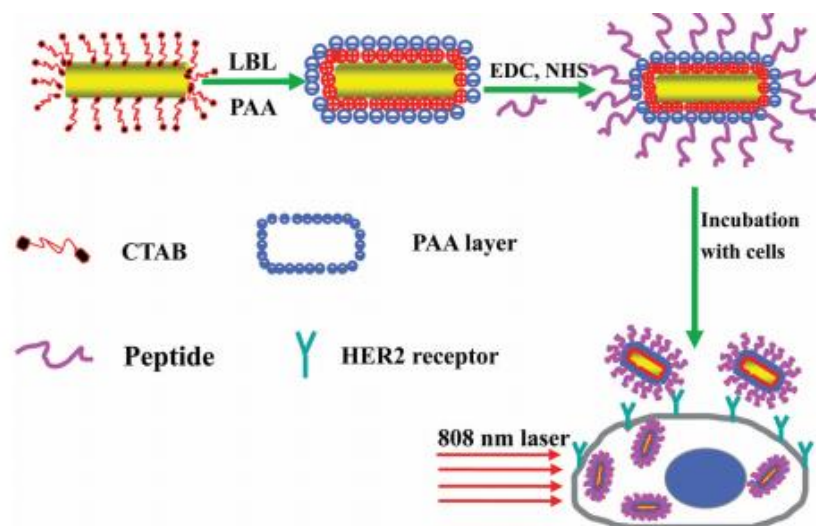


Figure 1.8: Processes involved in the synthesis of targeted peptide functionalized gold nanorods with polyacrylic acid (PAA) modification and the selective photothermal therapy. Cetyltrimethylammonium bromide (CTAB) capped gold nanorods were modified by a layer-by-layer (LBL) approach, the carboxyl groups of the PAA layer were activated by incubation 1-Ethyl-3-(3-dimethylaminopropyl) carbodiimide (EDC) and N-Hydroxysuccinimide (NHS), which allowed binding of the HER-2 peptide to the gold nanoparticle surface (Wang et al., 2012).

1.1.2 Silver Nanoparticles

Silver is an anti-microbial agent, and is effective against both planktonic cells and biofilms. Silver nanoparticles (AgNPs) have higher antimicrobial activity compared to silver salts due to the inhibitory effects of the salts and low stability (Mohanty et al., 2011) and AgNPs ensure continuous release of Ag ions from the NP (Kim et al., 2007). The anti-microbial mechanism of AgNPs is not clearly understood. The antimicrobial activity is dependent of the surface charge of the AgNPs. In fact, *E. coli* was not affected by zero valent AgNPs, while oxidised AgNPs showed a 90% decrease in intracellular ATP and cell survival levels (Kim et al., 2007). AgNPs have been found to generate free radicals that can cause membrane damage, release Ag

ions that can react with thiol groups of key enzymes and inactivate them. AgNPs may also react with DNA and cause problems with DNA replication and can interfere with protein phosphorylation and so can interrupt important intracellular signal transduction events (Prabhu and Poulouse, 2012) .

AgNPs have been found to accelerate wound healing, possibly due to the reduction of matrix metalloproteinase and increase in neutrophil activation. AgNPs can also inhibit interferon γ and tumour necrosis factor α (TNF α), which are also involved in inflammation (Prabhu and Poulouse, 2012) . Because of these properties companies such as Smith & Nephew plc utilized AgNPs in wound dressings such as ACTICOAT[®].

AgNPs also have been studied for their catalytic properties, for example spherical AgNPs of 37 and 26 nm in diameter reduce p-nitrophenol to p-aminophenol, using NaBH₄ as an electron donor with a catalytic rate constant of $2.6 \pm 0.4 \times 10^{-5} \text{ mol.m}^{-2}.\text{s}^{-1}$ and $1.6 \pm 0.1 \times 10^{-6} \text{ mol.m}^{-2}.\text{s}^{-1}$ (Santos et al., 2012) .

Table 1.1: Applications of AuNPs and AgNPs

Applications	References
AuNPs	
Drug delivery	(Ghosh et al., 2008; Pissuwan et al., 2010)
Gene delivery	(Ghosh et al., 2008)
Photothermal therapy	(Huang et al., 2007)
Antimicrobial	(Das et al., 2009)
Sensing	(Saha et al., 2012)
Degradation of recalcitrant pollutants	(Narayanan and Sakthivel, 2011)
AgNPs	
Antimicrobial	(Mohanty et al., 2011)
Anti inflammation	(Prabhu and Poulouse, 2012)
Catalyst	Salehi-Khojin et al., 2013

1.2 Metal Nanoparticle Characterisation

The physicochemical properties and potential cytotoxicity MNPs and their behaviour *in-vitro/ in-vivo* depend not only on the core metal, but also their size, shape, crystallinity, aggregation state and capping ligands. Therefore, thorough evaluation of these parameters is necessary to understand and predict the properties of the MNPs

1.2.1 UV- visible Spectrophotometry

MNPs interact strongly with light, due to the SPR, which for most MNPs occurs in the visible spectrum. In SPR analysis, a MNP sample is scanned from 700 to 350 nm and the absorbance is measured and plotted against wavelength. The presence of the MNPs is determined by peaks that correspond to their composition, e.g. gold nanoparticles (AuNPs) have a peak at ~520 nm and silver nanoparticles (AgNPs) ~420 nm. The position and the intensity of the peaks change due to MNP aggregation, size and shape. The height of the SPR peak corresponds to the concentration of the MNPs. Fig. 1.9 shows typical U.V. visible spectra for AuNPs and AgNPs.

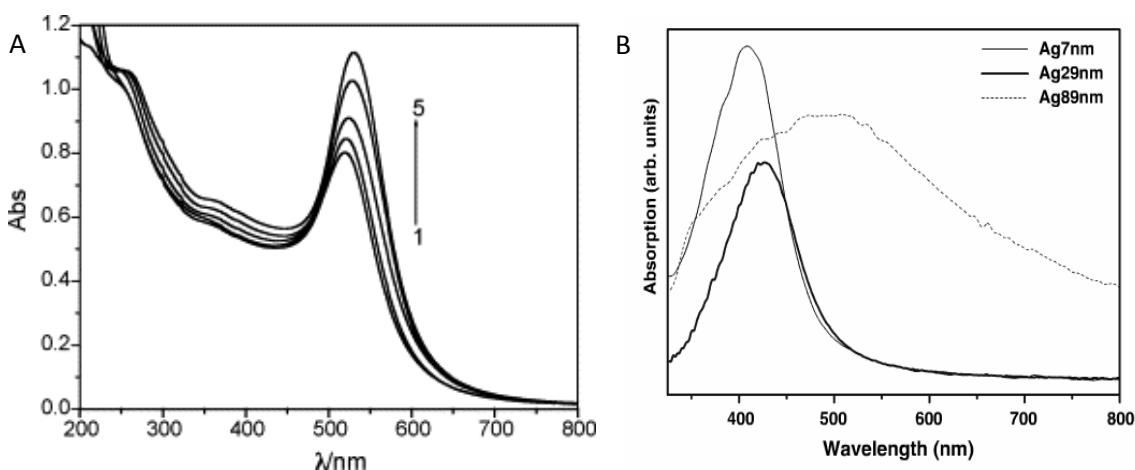


Figure 1.9: Absorption spectra of AuNPs (1: 12, 2: 19, 3: 24, 4: 33 and 5: 41nm) reported by (He et al., 2005) and AgNPs reported by (Martínez-Castañón et al., 2008).

1.2.2 Dynamic Light Scattering

Particles in suspension are constantly in motion (Brownian motion). As light scatters from the moving particle, its motion imparts randomness to the scattered light. When scattered light meets scattered light from a second particle, they either constructively or destructively interfere with each other-leading to time dependent fluctuations in the intensity of the measured light. The fluctuations are directly correlated with the speed of the MNP in suspension, and can be used to measure the particles diffusion constant. The particles diffusion constant can be used to calculate the hydrodynamic size of the MNP using the Stokes-Einstein equation (Eqn. 1.1).

$$D_H = \frac{kT}{6\pi\eta D} \quad (1.1)$$

Where D_{H+} is the hydrodynamic size of the particle, k is Boltzmanns constant, η is the solvent viscosity (e.g., water) and D is the diffusion constant.

1.2.3 Transmission Electron Microscopy

MNPs are too small to be observed using light microscopy, as the wavelength of visible light is too long (Rayleigh criterion). Instead of using light beams, transmission electron microscopy (TEM) illuminates a sample with an electron beam in a vacuum, increasing the resolution limit from 200 nm to 0.2 nm. Depending on the electron density of the sample, electrons will pass through or interact with the sample and scatter. Unscattered electrons pass through the sample and strike a fluorescent screen. The areas where the electrons have scattered are left darkened, (Fig. 1.10). Biological samples must first be fixed with glutaraldehyde or formaldehyde and dehydrated in a series of incubations with increasing ethanol concentration. Cells will not be visible under TEM without an appropriate stain such as osmium tetroxide that binds to lipids.

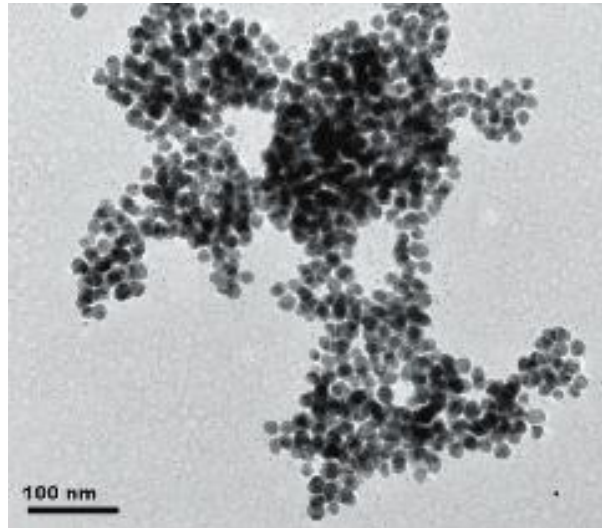


Figure 1.10: Sample TEM image of AuNPs prepared by *Rhizopus oryzae* protein extract (Sujoy Das et al., 2012)

1.2.4 Scanning Electron Microscopy

Similar to TEM, SEM uses a high energy electron beam to determine the surface morphology of a sample. When the incident beam interacts with the sample, the electrons are decelerated and produce secondary electrons, backscattered electrons and diffracted backscattered electrons and photons. The backscattered and secondary electrons are detected and used to build an image of the sample. As SEM uses backscattered and secondary electrons from a sample to construct an image, the resolution is not as high as TEM, and is usually used to analyse surface morphology. Fig. 1.11 shows that SEM may also be used to study biofilm formation.

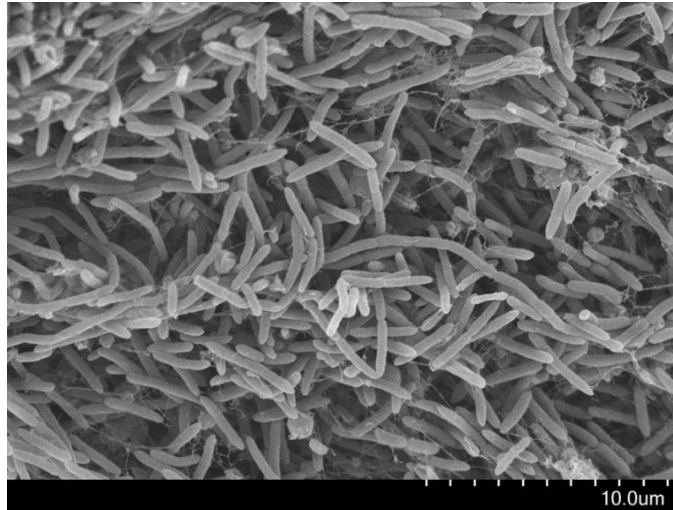


Figure 1.11: SEM of *Caldicellulosiruptor saccharolyticus* and *Caldicellulosiruptor owensensis* dual species biofilm (Pawar et al., 2015)

1.2.5 Atomic Force Microscopy

Atomic force microscopy analyses the topography of a sample, by examining the interaction between the cantilever tip and the sample surface. There are two modes of operation for AFM, depending on the nature of the interaction. In contact mode, the cantilever tip is in constant contact with the sample, while in non-contact mode the cantilever is vibrated at its natural frequency; interaction between the sample and the cantilever influences its vibrational frequency, and is affected by its distance. This change in vibrational frequency is detected by the AFM, and the cantilever position is raised to obtain the natural vibration frequency by a piezoelectric crystal. Both techniques require measuring the movement of the cantilever due to changes in the surface topography. Fig.1.12 shows how the cantilever tip movement is measured. The cantilever position is monitored by the reflection of a laser from the cantilever surface and then the information is sent to a computer, which is used to construct the topography of the sample. For MNP measurements, the sample is deposited on an atomically flat silica wafer.

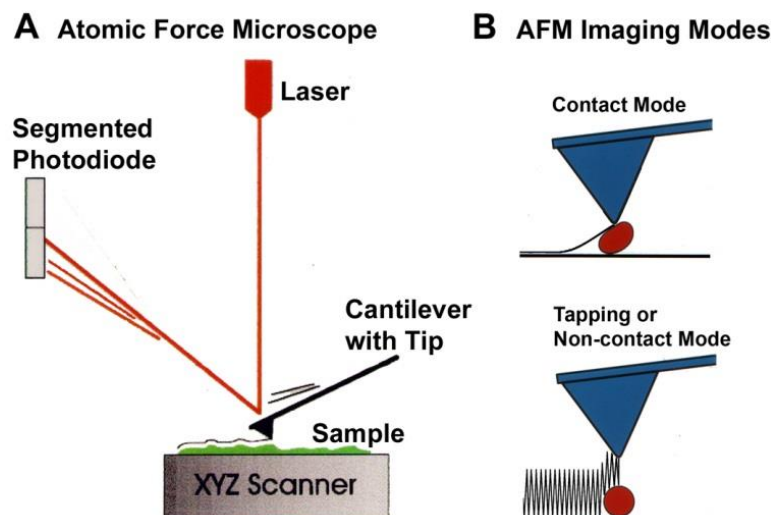


Figure 1.12: Modes of operation for atomic force microscopy (physics.csb.edu).

1.2.5 Energy Dispersive X-Ray Spectroscopy

In electron microscopy a solid sample when placed in the path of an electron beam. The incident electron beam excites the electrons in the inner shell of the atom, causing it to eject from the atom, creating an electron hole. Electrons from higher energy level shells then fills this hole, releasing energy in the form of X-ray photons. As this technique uses electron beams, it is usually included in the design of TEM and SEM microscopes. Fig 1.13 shows a representative energy dispersive x-ray spectra (EDX) form AuNPs produced by *Alternaria alternata* cell free extract. The peaks labelled C_k , O_k , N_k and Au_m represent X-ray radiation, characteristic from the excitation of these electron shells. From this we can determine that carbon, nitrogen, oxygen and gold are present in the sample.

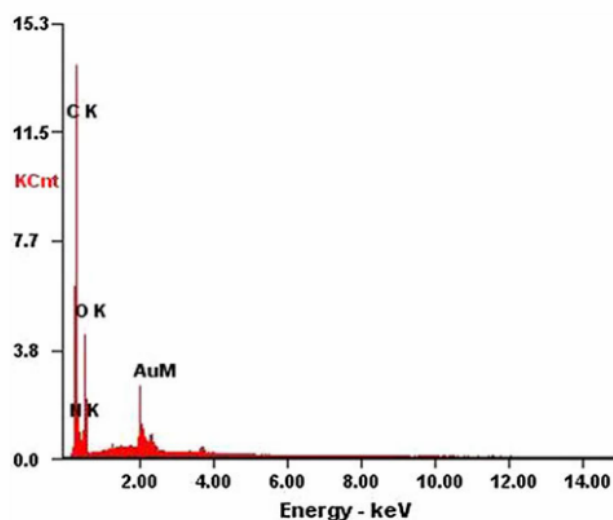


Figure 1.13: EDX spectrum of AuNPs produced by *Alternaria alternata* cell free extract (Sarkar et al., 2011).

1.2.6 X-ray Diffraction

Atoms periodically arranged in a crystal can diffract light as shown in Fig. 1.14. As the wavelength of X-rays is similar to distance between atoms, crystals illuminated with X-rays will cause X-ray diffraction and produce a diffraction pattern that is dependent on the crystal structure. Amorphous materials such as glass do not have a periodic array of atoms and so do not produce a diffraction pattern.

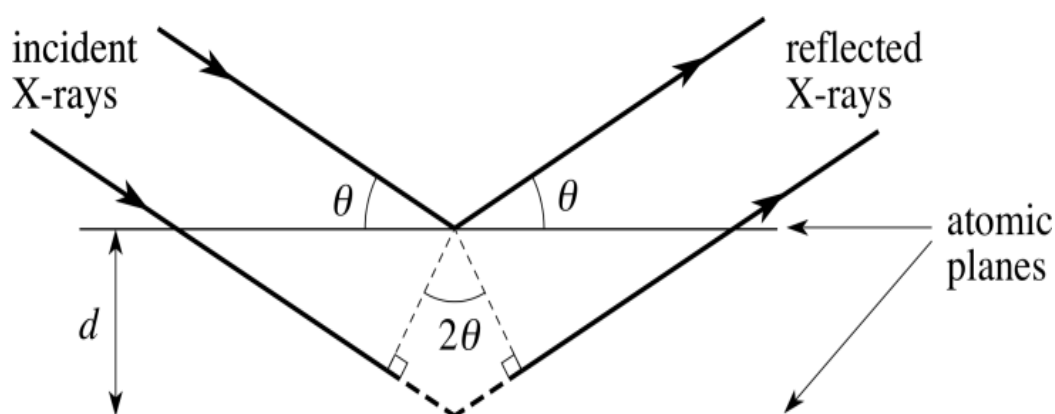


Figure 1.14: X-ray scattering from atomic planes.

Fig.115 shows XRD analysis of AuNPs produced by the cell free extract of *Penicillium* sp. 1-208, the peaks labelled (111), (200), (220) and (311) represent Au planes Au(111), Au(200), Au(220) and Au(311), respectively.

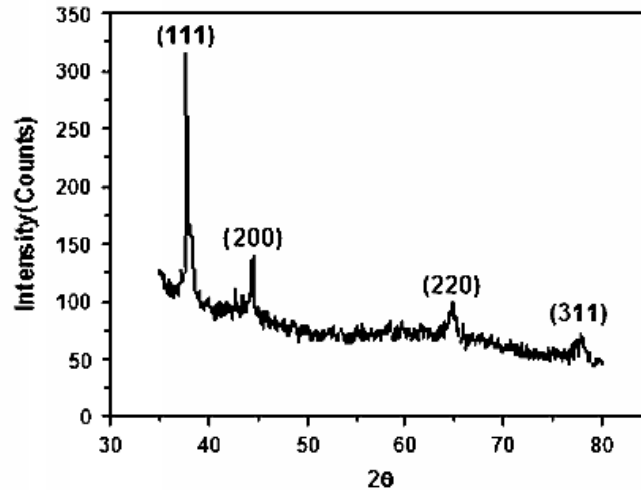


Figure 1.15: XRD of AuNPs produced by the cell free extract of *Penicillium* sp. 1-208 (Du et al., 2010).

Crystal size of the MNPs can be calculated first calculating the Bragg angle using Bragg's law (Eqn 1.2).

$$n\lambda = 2d\sin\theta \quad (1.2)$$

Where λ is the wavelength of the X-rays, θ is the Bragg's angle, which is the angle between the crystal surface and the incident X-ray and d is the spacing between atoms. N is an integer where constructive interference of the diffracted X-rays occurs.

This can then be used in the Scherrer equation shown in Eqn 1.3.

$$D = \frac{0.9\lambda}{\beta_{hkl}\cos\theta} \quad (1.3)$$

Where D is the average crystallite size and β_{hkl} can be calculated in Eqn 1.4.

$$\beta_{hkl} = \sqrt{(\beta_{hkl}^{meas})^2 - (\beta_{hkl}^{instr})^2} \quad (1.4)$$

Which is the 2θ full width at half maximum of the MNP plane after removal of the instrumental broadening; assuming Gaussian line profiles (Inguva et al., 2015).

1.2.7 X-ray Photoelectron Spectroscopy

In x-ray photoelectron spectroscopy (XPS) the sample illuminated by an X-ray beam, which causes excitation of the electrons in the inner shells of the atom, causing it to be ejected from the atom. As electron orbitals of different atoms possess different binding energies, measuring the kinetic energy of the ejected electrons gives the identity of the element and what it may be bound to. Fig 1.16 shows the biosynthesis of AuNPs in pear fruit extract, where Au $4f_{5/2}$, Au $4f_{7/2}$, C, N and O are detected (Ghodake et al., 2010).

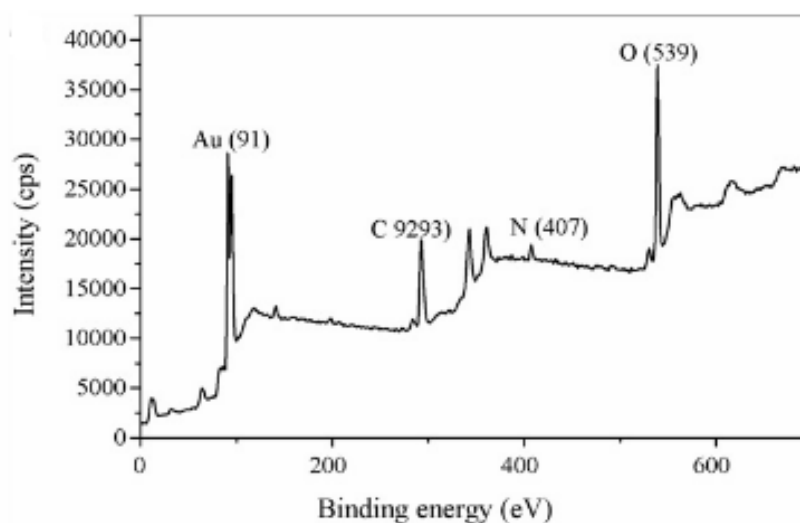


Figure 1.16: Sample XPS results of AuNPs produced by pear fruit extract (Ghodake et al., 2010).

1.3 Conventional Synthetic Methods for the Production of Metal Nanoparticles

There are two general approaches to synthesize MNPs, top down and bottom up. Top down utilises large macroscopic structures to control the nucleation nanoparticle, while bottom up utilizes physicochemical forces to control the size of the nanoparticle from its metal precursor salt in solution.

1.3.1 Lithography

Lithography controls the morphology of growing nanoparticles. An inert mould is imprinted with the desired nanoparticle morphology through various methods such as electron beam, polymer pen based printing, nanoimprint lithography or soft lithography. The etched mould acts as a template for nanoparticle growth, which allows for efficient control of the MNP size and shape and is used in nanoparticle arrays, however these processes are often expensive and laborious (Huang et al., 2012).

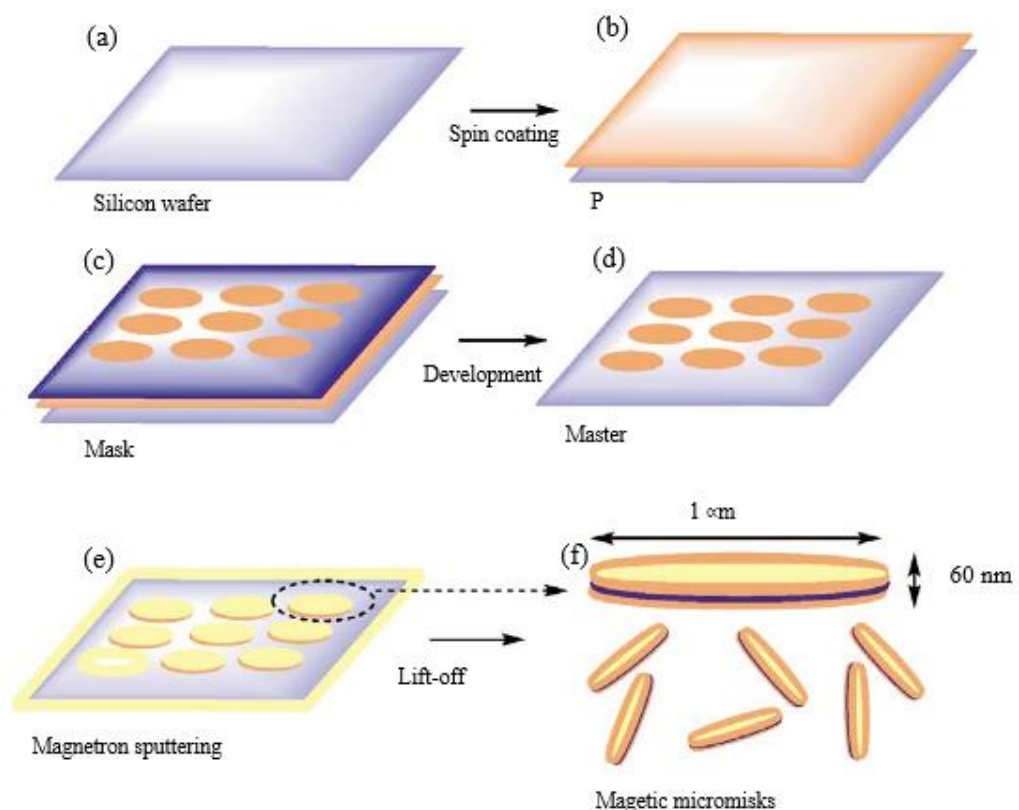


Figure 1.17: Fabrication of micro discs using optical lithography (Kim et al., 2010)

1.3.2 Inert Gas Condensation

Widely used in laboratory scale MNP synthesis, the source material is placed in the centre of a furnace and vaporised into an inert carrier gas such as helium or argon at ultra-high vacuum. The metal ions lose their kinetic energy by colliding with the carrier gas atoms, and condense to form MNPs. Although this technique is robust, it is energy intensive and raises MNP cost (El-Nour et al., 2010).

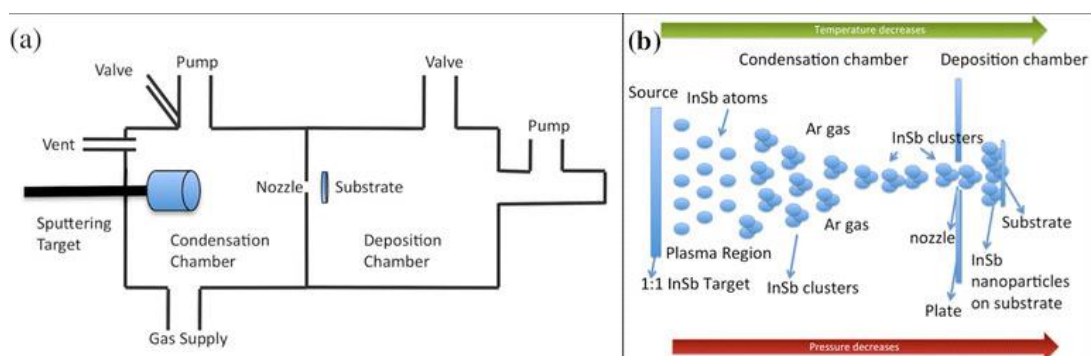


Figure 1.18: (a) Schematic of the inert gas condensation instrument (b) diagram explaining the formation of the nanoparticles during the inert gas condensation process (Pandya and Kordesch, 2015).

1.3.3 Electrochemical Oxidation

Electrochemical potential is used to oxidise a bulk metal to ions in the presence of an organic solvent, which acts as a stabilising agent. However, control of the MNP size and shape is an issue (Starowicz et al., 2006). Related to electrochemical oxidation, the key difference is that an electrical arch is used to oxidise a metal anode in a dielectric liquid, rather than an electrochemical reaction (Lo et al., 2007).

1.3.4 Laser Ablation

A bulk metal plate is decomposed by a laser while immersed in a liquid solution, forming a plasma plume, MNPs form upon condensation of this plume (Mafuné et al., 2001). Although laser ablation does not require the use of capping ligands (El-Nour et al., 2010) and MNPs can be obtained in a variety of solvents, control of the size of the MNPs requires optimisation of the background gas pressure and type, which requires an understanding of the complex gas dynamics and inflight characteristics (Amoruso et al., 2013).

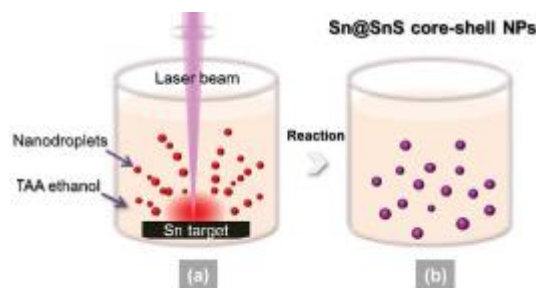


Figure 1.19: Schematic formation of tin sulphide nanoparticles (SnS) by laser ablation; (a) a long pulse width laser ablates bulk tin target in an ethanol solution of thioacetamide (TAA), (b) ablated high temperature tin nanodroplets react with ambient TAA to form core-shell SnSNPs (Sun et al., 2012).

1.3.5 Chemical Reduction

In this method, metal ions are reduced to an insoluble zero valent state through the use of reducing chemical species. There are a variety of reactions that can produce AuNPs, such as the Turkevich method, which produces AuNPs by the reaction of Au^{3+} ions with sodium citrate, which acts as a reducing and capping ligand. The Brust-Schiffrin method, Au^{3+} ions are reduced by sodium borohydride in tetraoctylammonium in the presence of dodecanethiol (Saha et al., 2012) .

Derivatives of this method have been reported, such as Sun and Xias study in 2002, where the production of AuNPs occurred though the reduction of Au^{3+} ions by ethylene glycol in the presence of poly(vinylpyrrolidone) (PVP) , which acts as a capping ligand (Sun and Xia, 2002). The advantage of this technique is the high uniformity of the MNPs synthesized, however the use of non-polar solvents has raised concerns about the potential environmental impact of these strategies. H_2O_2 has been studied as a reducing agent for MNP synthesis, however the reduction rate is too slow and an additional surfactant such as SDS or Triton X-100 is required to prevent MNP aggregation (Li et al, 2012). Other commonly used reducers are ascorbate and H_2 . Interestingly the use of a strong reductant resulted in small monodispersed MNPs, while weaker reductants resulted in a wide size distribution (El-Nour et al., 2010).

1.3.6 Sol-gel Synthesis

This robust technique has been used to produce a wide variety of structures such as calcium titanate powder, silica glasses and TiO₂ NPs. Formation of MNPs occurs through the gelatinization of the precursor solution, usually initiated by the addition of an acid to the solution. Sol-gel facilitated the nucleation and growth of MNPs, resulting in greater control of the size and shape of the MNPs produced than other physicochemical methods. There are two general sol-gel processes, depending on the solvent used, aqueous vs non aqueous. Aqueous sol-gel does not require an organic solvent however the procedure is complex and the structures produced are usually amorphous. Non-aqueous sol-gel processes may address the shortcomings of the aqueous sol gel, but this requires the use of organic solvents.

1.4 Biosynthesis of Metal Nanoparticles

Conventional methods for metal nanoparticle synthesis are potentially environmentally hazardous, laborious and cost intensive. Micro-organisms have been documented to produce nanomaterials for their physical properties such as mechanical strength (Beaufort et al., 2008) and magnetism (Yan et al., 2012) .

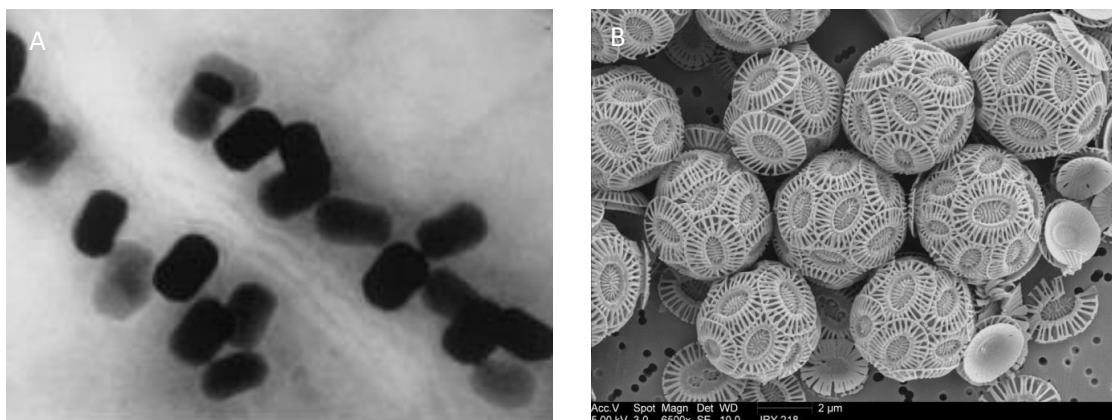


Figure 1.20: (a) TEM image of biosynthesized magnetite nanoparticles arranged in magnetosomes in a magnetotactic bacterium (Bazylinski and Frankel, 2004) and (b) SEM of coccolithophoric algae showing calcite plate exoskeleton (Young, 2003).

Metal nanoparticle biosynthesis by micro-organisms in a toxicity defence mechanism against metal ions in solution. Metal ions in solution can cause up regulation of reactive oxygen species (ROS) and antioxidant depletion, which leads to DNA damage and lipid peroxidation. Metal ions may react key sites in important enzymes, which may inactivate the enzyme causing disruption of cellular metabolism and nutrient uptake. Further certain metals such as Ag^+ have been found to impair membrane function (Lemire et al., 2013). Fig. 1.21 summarises the known anti-microbial activities of metal ions.

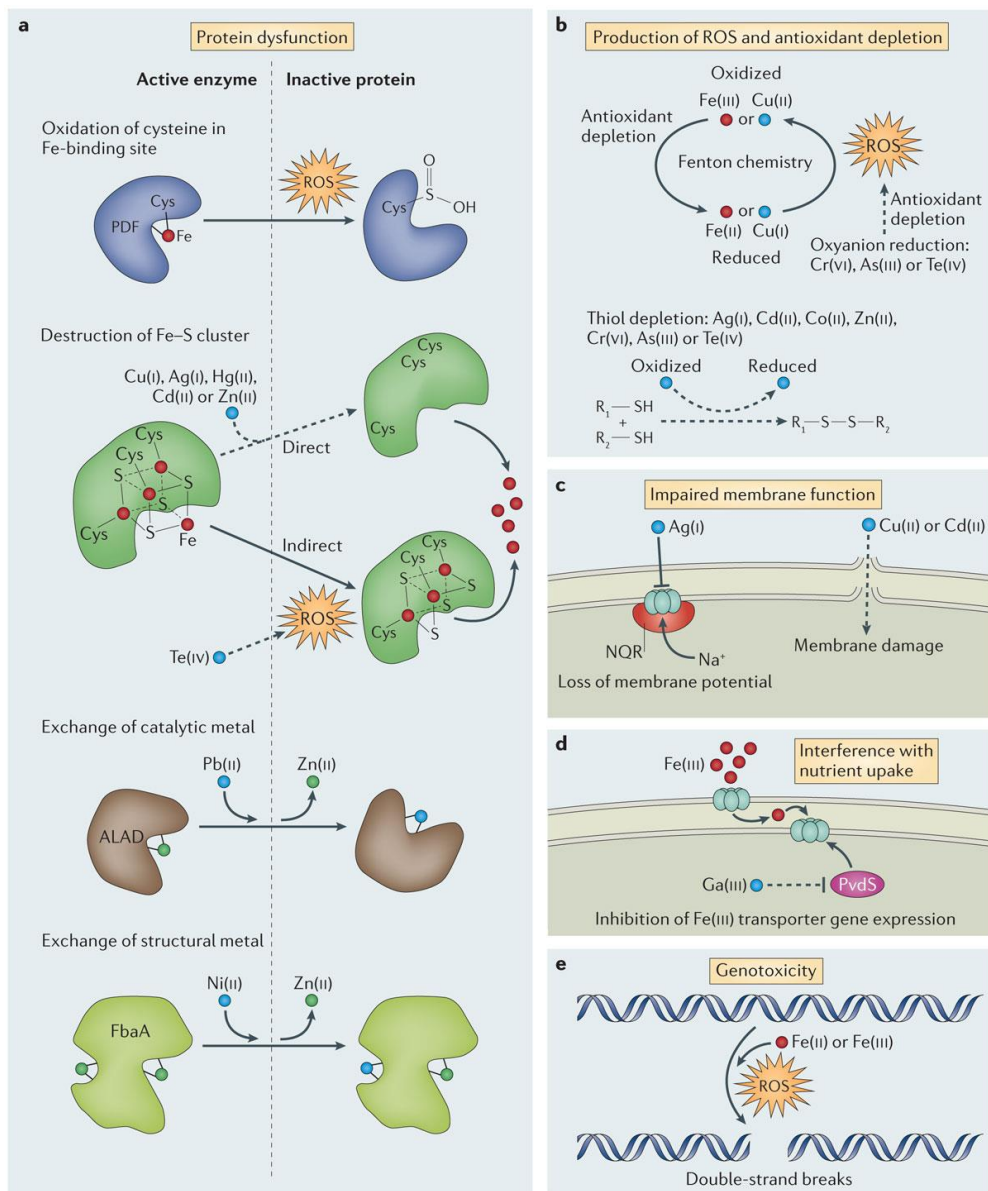


Figure 1.21: Antibacterial mechanisms of metal toxicity. (a) Metal ion inactivates enzyme through chemical modification, (b) up regulation of ROS (c) impairment of membrane function, (d) interference of nutrient uptake and (e) genotoxicity through DNA oxidation causing double strand breaks (Lemire et al., 2013).

In order to survive in heavy metal contaminated environments, microbes have evolved a variety of strategies to lower the toxicity, which are illustrated in Fig. 1.22. Microbes may utilise strategies that lower the intracellular concentration of heavy metals such as efflux pumps, or metal ion efflux pumps and lowered activity of transmembrane metal transport pumps. Microbes may also secrete siderophores which co-ordinate metal ions, which trap the metal ion and reduce metal ion uptake or increase metal ion efflux. Some strategies either repair the enzyme or bypass the affected metabolic pathway by producing proteins which do not contain active sites that are affected by the heavy metal. Microbes may also chemically modify the metal to a less toxic form, by modify its oxidation state or covalent modification (Lemire et al., 2013), which is exploited in the bioremediation of metal contaminated areas.

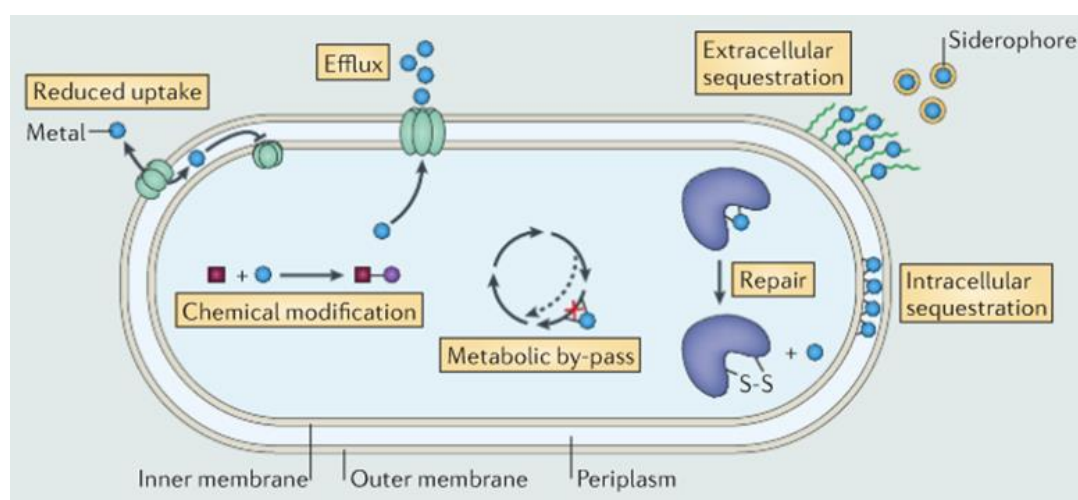


Figure 1.22: Defensive mechanism of microbial cells against heavy metals (Lemire et al., 2013).

Microorganisms have been reported to produce MNPs as a defence mechanism against the toxicity of metal ions in solution. Microbial cells have been reported to produce noble metal nanoparticles such as gold (Corte et al., 2011), silver (H. Wang et al., 2009), palladium (Wu et al., 2011) and platinum (Syed and Ahmad, 2012). Biosynthesis has also been reported for other metals such as uranium (Bargar et al., 2008), plutonium (Icopini et al., 2009) and bi metallic nanoparticles such as gold-palladium nanoparticles (Windt et al., 2005) and gold-silver nanoparticles (Castro-Longoria et al., 2010). Fig. 1.23 shows a selection of TEM images of biosynthetic MNPs.

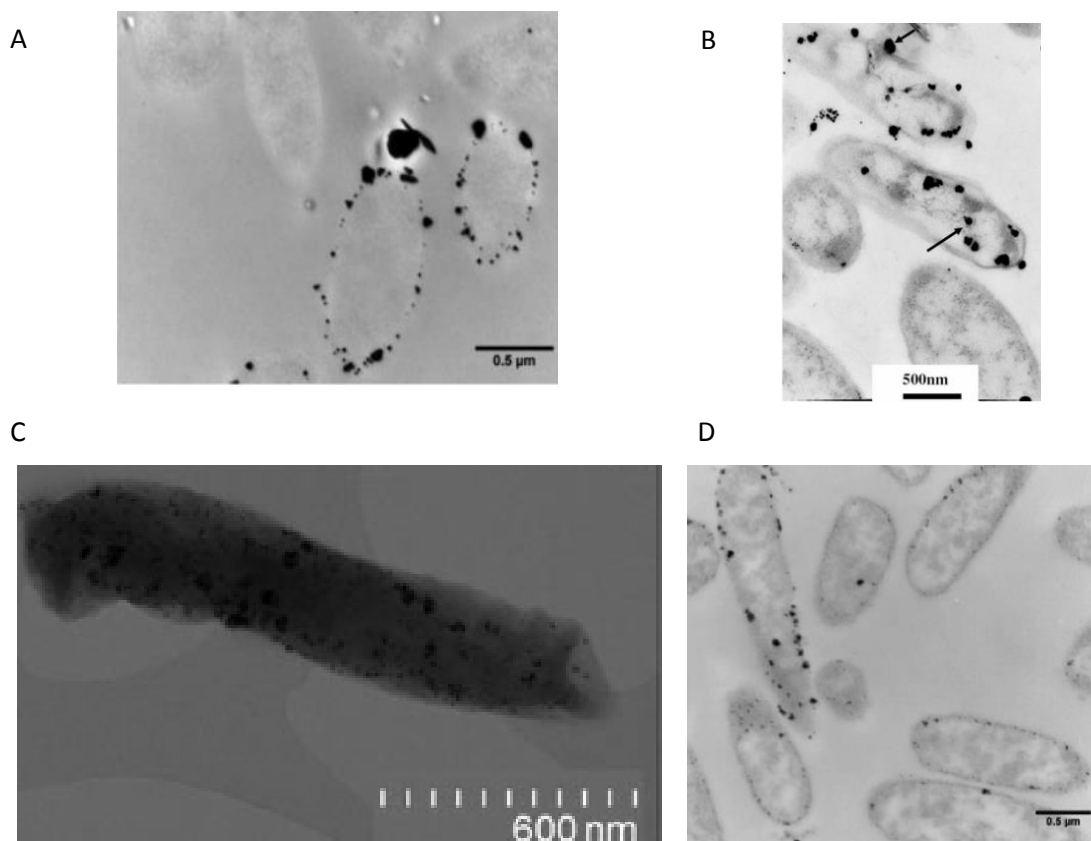


Figure 1.23: (a) AuNPs synthesized by *S. oneidensis* (Corte et al., 2011), (b) AgNP synthesized by *S. oneidensis* (H. Wang et al., 2009), (c) PdNPs synthesized by *Desulfovibrio desulfuricans* (Wu et al., 2011) and (d) Pd-AuNPs synthesized by *S. oneidensis* (Simon Corte, T. Hennebel, et al., 2011).

Further some papers report an improvement in some microbial processes such as an increase in extra cellular electron transfer in palladium treated *Desulfovibrio desulfuricans*. *D. desulfuricans* culture produced PdNPs located in the periplasm upon incubation with tetrachloropalladate for 24 hours, which participated in the electron transport pathway (Wu et al., 2011). Nakamura et al reported that colloidal α -Fe₂O₃ functionalised ITO electrodes improved current density by *S. loihica* PV-4 by over forty fold. The authors suggest this improvement in respiratory current is due to bacterial cell association with the α -Fe₂O₃ colloid assembly. However Wu et al reported that when *S. oneidensis* MR-1 cells exposed to Au³⁺ before inoculation into an electrochemical cell showed a reduction in redox current. Interestingly the $\Delta omcA/\Delta mtrC$ mutant showed an increase in the oxidation current, which suggests that the biogenic AuNPs may mimic the role of the omcA/mtrC cytochrome complex (Wu et al., 2013). In the last 15-16 years, biological synthesis methods have emerged

as a promising alternative, as these methods possess lower environmental impact and due to the specific interaction of the biomolecules and the inorganic surface, can occur at room temperature which lowers cost. However, the reaction is slow, taking hours to days compared to minutes, and the size distribution of the MNPs is far too broad for practical applications. The following sections describe the mechanism of MNP biosynthesis. As the majority of reports focus on AuNP biosynthesis, this section will tend to focus mainly on AuNPs, however reports for other MNPs will be included as appropriate.

1.4.1 Bioaccumulation/Biosorption

The first step in bacterial MNP biosynthesis is the bioaccumulation/biosorption of the metal ion precursor. Bacterial accumulation of metal ions is affected by metabolic state and solution pH. At pH 8, Au³⁺ accumulation by a viable *Cupriavidus metallidurans* culture was lower than at pH 5-7. Further, metabolically active cells accumulated more Au³⁺ than inactive or dead cells under all pH conditions examined. Further inactive/dead cells did not produce AuNPs, suggesting MNP biosynthesis is a metabolic mediated process.

Bioaccumulation of metal ions is a metabolically driven process and is more efficient than the passive biosorption. Heat treated *S. oneidensis* MR-1 cells removed Au³⁺ ions from the medium slower than metabolically active *S. oneidensis* cells.

Mukherjee et al, ruled out the role of sugars in metal reduction and suggested that positively charged amino acid residues (e.g. lysine) in cell wall and unidentified reductase enzymes were responsible for the trapping of Au³⁺ ions on the fungal cell surface and reduction to Au⁰ for the fungi *Verticillium* sp (Mukherjee et al., 2001).

1.4.2 Metal ion Induced Changes in Gene and Protein Expression

SDS-PAGE analysis of active *Rhizopus oryzae* incubated with Au³⁺ demonstrated up regulation of proteins at 42kDa and 45kDa, which suggests that Au³⁺ stimulates a stress response at sub toxic concentrations (15-130µM) while at higher Au³⁺ concentrations (250µM) toxicity of the Au³⁺ ions inhibits growth and protein

expression, and may induce protein degradation as a response to the oxidative stress (Das et al., 2012).

Microarray experiments of *Cupriavidus metallidurans* cultures exposed to sub-toxic concentrations of Au³⁺ (10-100µM) showed that out of 6205 transcripts analysed, 52-303 upregulated while 32-229 were down regulated. The gene cluster Rmet_3618-3623 was the highest upregulated, which contained the oxidative resistance genes (*ohr*, *oxyR*, *ahpC*, *kata* and *sodB*). Further, the genes for Cu⁺/Cu²⁺ detoxification on chromosome 1 and plasmid pMOL30 (cup/cop regions) along with the mercury resistance cluster (*mer*) was shown to be up regulated (Reith et al., 2009).

1.4.3 Bioreduction

Bioreduction is a biologically driven reaction where biomolecules such as sugars, enzymes or vitamins donate electrons to an exogenous electron acceptor. The main precursor of AuNPs is HAuCl₄, which dissociates to Au³⁺ ions and AuCl which dissociates to Au⁺ (Kitching et al., 2014). The Au³⁺ precursor is preferred due to the higher solubility of Au³⁺ ions, however Au⁺ ion solubility may be improved by complexation with the appropriate ligand such as alkenes, alkylamines, alkylphosphines, alkanethiols, and halide ions. For AgNPs, AgNO₃ is preferred as a metal precursor due to its solubility in water.

Bioreduction of metal ions can occur in one or two steps, depending on the metal oxidation state, as shown in Eqn 1.5 for Ag, and Eqn. 1.6-1.7 for Au below.



Cupriavidus metallidurans reduces Au^{3+} ions to Au^{1+} in the intracellular environment. This process was relatively rapid, as 100% of the bioaccumulated Au^{3+} was reduced to Au^+ in less than 6 hours. Detection of an Au^+ -C complex led the authors to suggest methylation as a possible defence mechanism. Methylation may also reduce Au^{3+} ions to Au^+ in the fungi *R. oryzae* (Das et al., 2012). XPS of a partially purified *R. oryzae* protein extract incubated with Au^{3+} ions showed that the concentration of Au^{1+} initially increased. However, over time the Au^{1+} concentration decreased while the concentration of Au^0 increased. XPS of the protein extract also revealed a negative surface charge and shifts in the C_{1s} and N_{1s} after interaction with the Au^{3+} ions demonstrates that Au^{3+} ions bind to cytosolic proteins through covalent interaction instead of electrostatic interaction; this suggests that Au ions are reduced by proteins.

As shown in Fig. 1.24, reduction of the metal ions can occur in either the intracellular or extracellular space, depending on the species examined. Intracellular reduction is more common for bacterial species, while extracellular reduction is more common for fungal species (Kitching et al., 2014). Intracellular reduction occurs at high concentration of the metal ion precursor. A planktonic cell *S. oneidensis* culture when exposed to sub toxic concentrations of Ag^+ ($10\mu\text{M}$) for 24 hours, the AgNPs formed precipitated on to the cell surface, however when the concentration of Ag^+ was increased to $100\mu\text{M}$, AgNPs were found mostly in the cytosol (Wang et al., 2009). Reducing agents for bacterial synthesis of MNPs have not been thoroughly examined, however for the electroactive bacteria *Shewanella* sp. and *Geobacter* sp. outer membrane cytochrome complexes are known to reduce metal ions via heme groups which act as an electrical conduit between the periplasm and the extracellular environment.

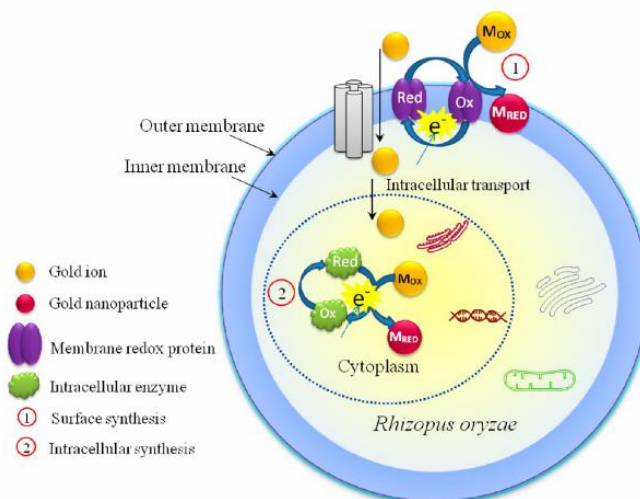


Fig. 1.24: Mechanisms of Au reduction by *R. oryzae* (Das et al., 2012)

Intracellular metal reduction is not as well understood, as it is unclear how metal ions diffuse through the cell membrane. Two mechanisms are proposed, either through active bioaccumulation or passive biosorption, due to the increase of membrane porosity caused by metal ion toxicity.

The appearance of a peak at $1,735\text{cm}^{-1}$ of the FTIR analysis of viable *Phanerochaete chrysosporium* biomass after interaction with Au^{3+} ions suggests involvement of aromatic amino acids such as tyrosine or tryptophan in the reduction of metal ions (Sanghi et al., 2011). Au^{3+} reduction by the cowpea chlorotic mottle viruses of unmodified SubE (yeast) (CCMV) occurred through the hydroxyl groups of tyrosine residues that extend from the capsid. Further the ratio between tyrosine to histidine residues in the capsid influences AuNPs, requiring at least a ratio of 2:1 (Slocik et al., 2004), as histidine has a high affinity towards transition metal ions as the electron donor groups on the imidazole ring readily forms co-ordination bonds (Bornhorst and Falke, 2000).

Alkalinity of the solution affects the metal reduction rate, due to the formation of $\text{Au}(\text{OH})_3$ complex. Tyrosine was found to be responsible for Au reduction by the CCMV virus. Interestingly at pH 10 (pKa of tyrosine) was found to produce substantially higher amounts of AuNPs for the virus, however due to the formation

of the insoluble $\text{Au}(\text{OH})_3$ complex, the reduction rate was significantly lowered (Slocik et al., 2004).

Non protein mechanism for metal reduction has been suggested in the literature such as riboflavin. Riboflavin is a redox shuttle used in *Shewanella* sp. for mediated extracellular electron transfer. Depending on the solution pH, it can be either positively or negatively charged or found in a neutral state. Nadagouda and Varma were able to produce AgNPs and PdNPs using purified commercial riboflavin as both a reducing and capping agent (Nadagouda and Varma, 2008). Au^{3+} ions in the presence of glutathione have been shown to induce phytochelatins by *Candida albicans*, which have been shown to reduce metal ions. Melanin when secreted in a phenol form can reduce Au^{3+} to Au^0 , and is oxidised in the process to its quinone form (Chauhan et al., 2011) .

1.4.4 Nanocrystal Formation and Capping

At present there are no reports directly examining how the metal nanocrystal forms during biogenic MNP synthesis. Cell/protein structure has been hypothesized to act as a template for MNP growth, but this has not been experimentally demonstrated. The topology of CCMV viral capsid surface did not contribute significantly to AuNP nucleation, due to the rapid reduction of Au^{3+} ions (Slocik et al., 2004). Although very few studies examine the nucleation process, XRD analysis (Table 1.2) of the MNPs show that biogenic MNPs are usually semi crystalline in nature possibly to the specific interaction of the protein and inorganic surface and low temperature of the synthesis.

Table 1.2: Au planes detected by XRD of various viable fungal cell and protein extract synthesized AuNPs reported in the literature

Organism	Plane	Reference
Extract		
intracellular protein extract <i>Pycnoprus sanguineus</i>	Au (111), Au (200), Au(220), Au(311) and Au (222)	Shi et al., 2015
boiled <i>Volvariella volvacea</i> extract	Au (111), Au(200) and Au (220)	Philip, 2009
blended Pear extract	Au (111) and a small Au (200)	Ghodake et al., 2010
Secretome of <i>Penicillium</i> sp. 1-208	Au (111), Au (200), Au(220), Au(311)	Du et al., 2010
Viable Whole Cells		
<i>Phanerochaete Chrysosporium</i>	Au (111), Au (200), Au(220), Au(311)	Sanghi et al., 2011
Metal tolerant fungi isolates	Au (111), Au (200), Au(220), Au(311)	Gupta et al., 2011
<i>Epicoccum nigrum</i>	Au (111), Au (200), Au(220), Au(311)	Sheikhloo et al., 2011
<i>Hormoconis resinae</i>	Au (101), Au (200) and Au (220)	Mishra et al., 2010

Small Au^0 crystals are unstable and can be disturbed by changes in pH and temperature. The MNPs must be capped by biomolecules derived from the cell (Fig. 1.25a). Capping proteins may be loosely bound by electrostatic interaction or Vann der Walls forces due to the small size. Capping proteins may also bind via covalent bonds with phosphate groups (Fig. 1.25b) or carboxylic acid groups. FTIR is the most commonly used method to detect the capping ligands. However as microbes produce a variety of enzymes and other proteins, the individual molecules can't be identified. FTIR can identify the presence of organic molecules and the shifting of functional groups to lower frequencies indicates interactions with other groups. The main FTIR results from the literature are summarised in Table 1.3.

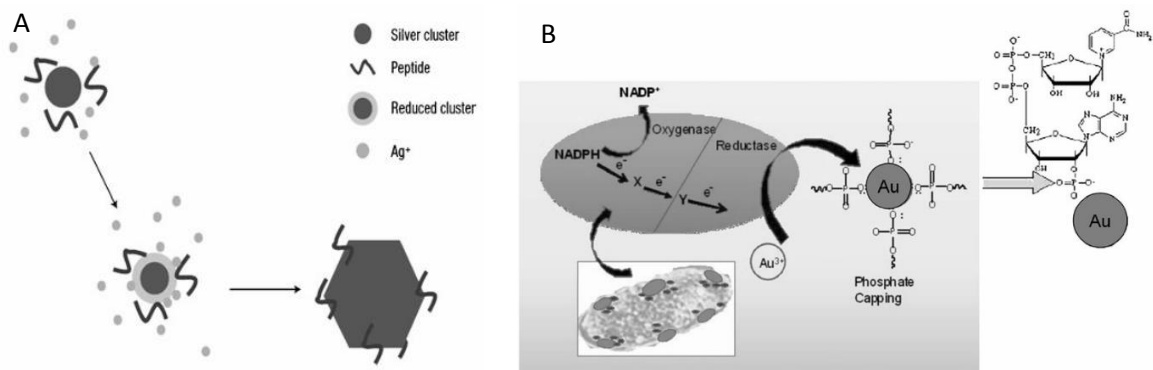


Figure 1.25: Proposed mechanism of (a) AgNP formation and (b) AuNP formation in *Stenotrophomonas maltophilia* (Durán et al., 2011)

Table 1.3: FTIR characterization of AuNP capping and stabilizing agents in various microbial species

Species	Main FTIR peaks that shift following AuNP formation (cm ⁻¹)	Groups	Putative biomolecule	Reference
<i>Rhizopus oryzae</i>	1652.9, 1550 and 1379	Amide I, II and III	Surface-bound protein	Das et al., 2009
<i>Aspergillus oryzae</i> var. <i>viridis</i>	1660 and 1530	Amide I and II	Proteins (through free carboxylate groups)	Binupriya et al., 2010
<i>Colletotrichum sp.</i>	1658, 1543 and 1240	Amide I, II and III	Proteins	Shankar et al., 2003
<i>Penicillium brevicompactum</i>	3100–3350 (broad peak)	NH or OH	Proteins	Mishra et al., 2011
<i>Aspergillus niger</i>	1383 and 1112	Aromatic and aliphatic C-N	Proteins	Bhambure et al., 2009
<i>Phanerochaete chrysosporium</i>	1367 and 1029	Aromatic and aliphatic C-N	Proteins	Sanghi et al., 2011
<i>Alternaria alternata</i>	1625, 1425, 874 and 1240	Amide I, C-H deformation, C-H aromatic, and Amide III	Proteins	Sarkar et al., 2011

Thiol groups have been found to be to bind directly to AuNPs by FTIR. FTIR analysis of *Phanerochaete chrysosporium* protein extracts revealed the disappearance of –SH stretching band when the protein extract was incubated with Au³⁺ ions (Sanghi et al, 2011). Phosphate groups of proteins have also been suggested to bind to the surface of AuNPs produced by *R. oryzae*. Das et al detected the shift amide groups of these groups in their study of *R. oryzae*, suggesting free amine groups may be involved in AuNP capping (Das et al., 2012).

Most reports do not examine band shifting in FTIR, so the detection of function groups here does not indicate their involvement in MNP binding, but infers the identity of the bound molecule. Amide I, II and III groups are the most commonly detected group in the FTIR analysis of biogenic MNPs, suggesting proteins are the main capping agent in MNP biosynthesis. Shankar et al also detected Amide I, II and III bands in their study of AuNPs synthesis by *Colletotrichum* sp. Binupriya et al detected amide I and II bands in the AuNPs produced by *Aspergillus oryzae* var *vidis*. Suresh et al using viable *S. oneidensis* cells to produce AuNPs detected Amide I and II peaks, and a small Amide III peak (Suresh et al., 2011) .

Phenol groups have been detected in Mishras study of AuNP biosynthesis by *Penicillium brevicompactum*. Carboxylic acids due to their negative charge may also be involved in AuNP capping as suggested by studies of AuNP biosynthesis by *R. oryzae*, *P. brevicompactum* and *A. alternata*.

In addition to methionine and cysteine, there have been other amino acids suggested to be involved in AuNP biosynthesis. Aromatic amino acids such as tyrosine and tryptophan have been suggested to be involved in AuNP capping in *Aspergillus niger*, *P. chrysosporium* and *A. alternata*.

Few proteins to date have been identified to be involved in MNP capping, however Zhang et al, 2011 identified proteins involved in energy metabolism (ATPase, 3-glucan binding protein and glyceraldehyde-3-phosphate dehydrogenase) to be involved in the capping for AuNPs produced by *Fusarium oxysporum*, which suggests reducing proteins may also be involved in MNP capping (Zhang et al., 2011)

1.5 Problems with Metal Nanoparticle Biosynthesis

The biosynthesis methods, although cost effective, greener and not as laborious, suffer from several drawbacks that compromise their use in commercial applications. MNPs properties are size dependent, chemical reduction production of MNPs produces a uniform MNP population; the biosynthetic methods produce MNPs with a too broad size distribution for practical applications, due to the long incubation time required and the non-specificity of the process (Kitching et al., 2014). Due to the toxicity of the heavy metal precursor, scale up of the biological synthesis of MNPs is a challenge. Although the synthesis time is longer from days to hours or fraction of hours, viable cell synthesis is preferred over cell extracts, as downstream processing of the effluent increases the synthesis cost, the biological host cannot be recovered and reused and viable cells may respond with greater reducing potential due to an active response to Au^{3+} ions.

In this context, *Shewanella* sp. biofilms were utilised for the production of AgNPs and mammalian cell lines to produce AuNPs. Immobilised biomass has been poorly examined for MNP biosynthesis, although it is possible, for example Kalathil et al was able to produce AgNPs between 1-7nm in size within 2 hours using a mixed species biofilm on carbon paper (Kalathil et al., 2011). Immobilised biomass does have potential advantages over the planktonic mode of cultivation, which is listed in Table 1.4.

Table 1.4: Advantages and disadvantages of using planktonic cells and immobilised biomass for high value product synthesis

	Advantages	Disadvantages
Planktonic	Lower mass transfer resistance Easier scale up Easier to quantify cell growth and productivity	Free cells require separation from product
Immobilized	Easier reuse of biomass (Qureshi et al., 2005) Promotes easier separation of product from catalyst (Qureshi et al., 2005) High productivity (Qureshi et al., 2005)	Cell growth restricted by matrix (Qureshi et al., 2005) Membrane reactors may foul (Qureshi et al., 2005) Increased mass transfer resistance

1.6 Aims of the thesis

Biological synthesis of MNPs although promising, suffers from limitations that prevent them from commercial and industrial application, which are the slow synthesis rate and wide size distribution. Further, the use of microbial hosts raises concerns about the potential immunogenicity of the biogenic MNPs. The aims of the thesis were to explore novel strategies to increase the MNP synthesis rate, decrease the particle size distribution of the biogenic MNPs and to explore the potential of mammalian cell biosynthesis of MNPs to address the potential immunogenicity of the biogenic MNPs synthesised by microbial hosts.

Chapter 3 examines the possibility of increasing the synthesis rate of AgNPs by *Shewanella oneidensis* MR1. biofilms by the application of a mild reducing electrochemical potential. This chapter also investigates the effect of the electrochemical potential on the size and shape of the AgNPs produced by the biofilm. Chapter 4 will focus on the optimisation of the protein extraction buffer and

examines the effect of the extraction buffer on the particle size and size distribution of AuNPs synthesised by cell surface protein extracts from *R. oryzae*.

Immunogenicity of MNPs synthesised by microbial hosts is a concern for in-vivo use due to the presence of microbial proteins in the protein corona. As the protein corona derived from mammalian cells is less likely to be immunogenic, mammalian cell biosynthesis is explored in Chapter 5. Bovine aortic endothelial cells were investigated for their ability to synthesise AuNPs. Cell culture conditions such as synthesis buffer selection, serum concentration and the initial concentration of the gold salt precursor (HAuCl_4) were optimised. Further AuNPs synthesised under the optimised conditions were characterised in terms of their size, shape, crystallinity and surface chemistry.

Chapter 2: Materials and Methods

A comprehensive description of the methods used in this study.

2.1 Cell Culture and Biomass Preparation

Microbial and mammalian cell culture procedures were performed using already optimised procedures or suppliers recommendations. Media recipes can be found in Section 2.6.

2.1.1 Microbial Cell Culture

Shewanella oneidensis MR1 was sourced from the Belgian Co-ordinated Collection of Micro-organisms (BCCM) as a freeze dried culture and was revived by suspending the pellet in Luria broth (LB) and plating on Luria agar (LA) (50µl of suspended culture per plate). *Escherichia coli* was sourced from a previous PhD student (Monica Epifanio) and revived by scraping surface of culture tube with sterile inoculation loop and spreading on LA plate. Both species were maintained on LA, a widely used bacterial culture medium, at 30 °C in an incubator (Lab Companion, UK) (Fig 2.1). A single colony was used to inoculate a new LA plate twice per week for both bacterial species.

Rhizopus oryzae was sourced from Dr. Sujoy K Das from the Central Leather Research Institute, Chennai Province, India, was shipped as an active cell culture on dry ice. Upon receipt, it was immediately spread on Potato Dextrose Agar in Agar Slant tubes. *R. oryzae* was maintain on PDA slants and sub cultured weekly.

All microbiological techniques were carried out under aseptic conditions in a 70% ethanol cleaned Microflow Laminar Flow Hood, BSL-1 (Astec, UK).



Figure 2.1: Photograph of Laminar flow hood used for microbial cell work.

2.1.2 Establishment of the *Shewanella* Biofilm

The inoculum size impacts the growth of a culture, therefore the culture was standardised before inoculation to increase repeatability. A single colony was used to inoculate 10 mL of LB in a 50ml culture flask to generate sufficient biomass. The culture was then incubated at 30 °C for 22 hours at 150 rpm under aerobic conditions. After incubation the optical density of the culture was measured, and the culture was diluted to an $OD_{600nm}=1$ using LB to standardise the culture. 2 mL of the culture was used to inoculate 20 mL of Modified M1 media in 100 mL flask, and incubated for 24 hours at 30 °C and 150 rpm under aerobic conditions.

In order to retain redox mediators important for electroactive biofilm formation, 20 mL overnight culture was added to the 20 mL of fresh Modified M1. 10 mL of the culture was inoculated into each bioelectrochemical reactor (Epifanio et al., 2015). The medium was flushed for 15-20 minutes with humidified N_2 gas, which was humidified by passing through sterile water in a closed 100ml serum bottle. Once anaerobic conditions were obtained in the culture, they were maintained by flushing the headspace continuously with humidified N_2 . The cells were then incubated at 30°C by pumping 30°C water through the heat jacket of the ECs, and the working electrodes were poised at a potential of +0.2 V vs. Ag/AgCl to promote bacterial attachment. To reduce mass transfer limitations, the chamber was stirred at 150rpm by a magnetic stirrer.

2.1.3 Fungal Cell Cultivation and Protein Extraction

R. oryzae biomass was maintained on potato dextrose agar (PDA). Fungal biomass was cultivated aerobically in 700 mL Potato Dextrose Broth (PDB) (inoculated in 14 X 50 mL flasks) for 72 hours at 30°C and 150 rpm.

After the 72 hours incubation, the fungal biomass was washed thrice with ice cold phosphate buffer (50 mM, pH 7.2) and then blot dried with Whatman blotting paper to remove residual PDB. Dried mycelium was then cut into small pieces and disrupted by grinding with sea salt with a mortar and pestle in the above mentioned phosphate buffer until a slurry was formed. The slurry was centrifuged at 12,000 rpm for 20 minutes at 4 °C.

The pellet was washed thrice with ice-cold 50mM phosphate buffer and then dried with blotting paper. 3g of the pellet was added to 15 mL extraction buffer (Buffer: 1: 2mM dithiothreitol in 25 mM Tris-HCl, pH 8.5, buffer 2: 0.1% SDS in 0.1 M phosphate buffer, pH 8.0, or buffer 3: 1% Triton X-100 in 0.1 M phosphate buffer, pH 8.0), which was then incubated for 6 hours at 4°C for extraction buffer 1 and 30-35°C for buffer 2 and 3.

2.1.5 Mammalian Cell Culture

All cell culture experiments were carried out under aseptic conditions in a Bio air 2000 Mac laminar flow cabinet (Euroclone, Spain) (see Fig. 2.2). The laminar flow hood was cleaned with Virkon and 70% ethanol immediately before and after use. The laminar flow cabinet was also U.V. sterilised on a frequent basis.



Figure 2.2: Laminar flow hood used for mammalian cell culture experiments.

Bovine aortic endothelial cell line (BAEC) and Bovine aortic smooth muscle cell line (BASMC) were sourced from the NIH repository. BAECs of passage 11 to 20 and BASMCs of passage 4 to 31 were used in these experiments. BAECs were incubated in Roswell Park Memorial Institute medium 1640 (RPMI 1640) media supplemented with 10% foetal bovine serum (FBS) and 1% penicillin/streptomycin (P/S) antibiotic cocktail, which will be referred to as full RPMI 1640 media and stored at 37 °C, in a humidified atmosphere of 5/95 % CO₂/air (v/v) in a Hera water jacket heated incubator (Thermo Scientific, US).

BAEC and BASMC cultures in 6 well plates (Fisher Scientific) were stored in stacks of a maximum of 3 and T75 flasks (Fisher Scientific, US) were fitted with vented filtered caps to ensure appropriate gaseous exchange. See Fig. 2.3 for photographs of culture vessels used in this study. Cell culture plates and flask surfaces were vacuum gas plasma treated by supplier, which enhances cell attachment. 6 well plates were used for AuNP biosynthesis experiments, due to the low volume needed for experiments. T75s were used to grow sufficient amount of cells for AuNP biosynthesis experiments.

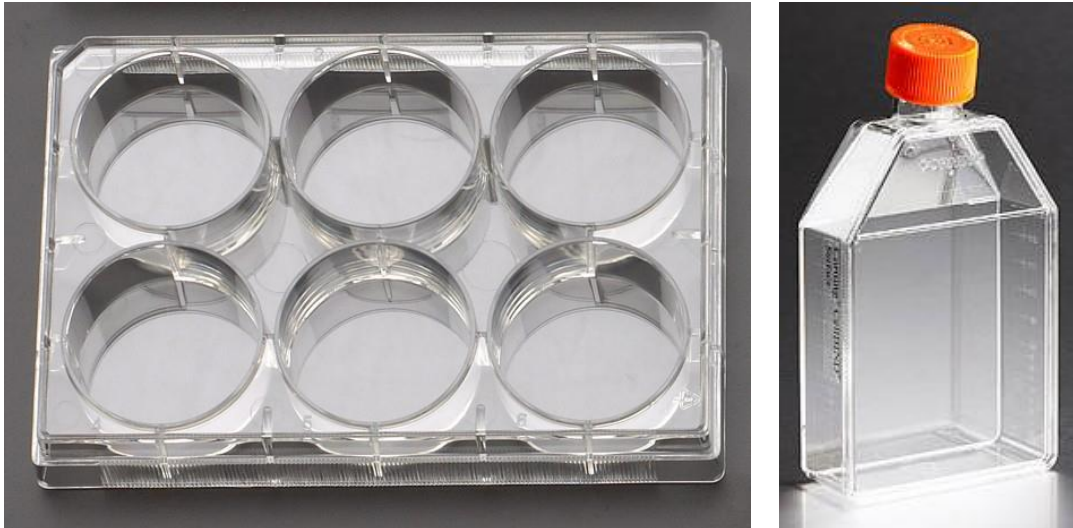


Figure 2.3: Photograph of culture vessels (a) 6 well flask (socialbiomedial.com), (b) T75 flasks (eandkscientific.com).

2.1.6 Mammalian Cell Subculture

BAECs and BASMCs were passaged when they reached 90% confluency. Media was aspirated using a glass pipette connected to a vacuum. BAECs and BASMCs were then washed twice with 1X phosphate buffer saline (PBS) to remove residual FBS, which inhibits trypsin activity. Trypsin was used to hydrolyse the surface proteins of BAECs and BASMCs, which anchor the cell to the surface of the plate. A 1X solution of trypsin was prepared by diluting the 10X stock solution of trypsin in 1X PBS, without Ca and Mg ions, which aid in cell attachment. 2.5mls of the 1X trypsin was added the BAECs and BASMCs in the T75s flasks, and incubated at 37 °C and 5% CO₂ for 5 minutes to detach the cells. 5mL of full RPMI-1640 media was added to each T75 flask to inhibit further trypsin activity, which may lower cell viability. The cell suspensions were centrifuged at 1,200 rpm for 5 minutes to pellet the cells. The cells were then counted as described in Section 2.1.7. Once the cell density was calculated, the original cell suspension was used to inoculate T75 flasks and 6 well plates were then seeded at 60% confluency

2.1.7 Cell counting

Cells were then counted by haemocytometry, using a Neubauer improved bright line haemocytometer. Cell pellet was suspended in 1ml of full RPMI media, and an aliquot of this suspension was diluted by a factor of 10 in full RPMI media. 100µl of

the diluted cell suspension was loaded onto the haemocytometer, and cells counted under a light microscope, using a cell counter. Fig 2.2 illustrates the cell counting grid in the haemocytometer, the four corner squares (one of which is marked in Fig. 2.1). Cells were counted in these 4 squares, and an average cell count was taken. If the cell count in a single square was over 100, the cell suspension was diluted further.

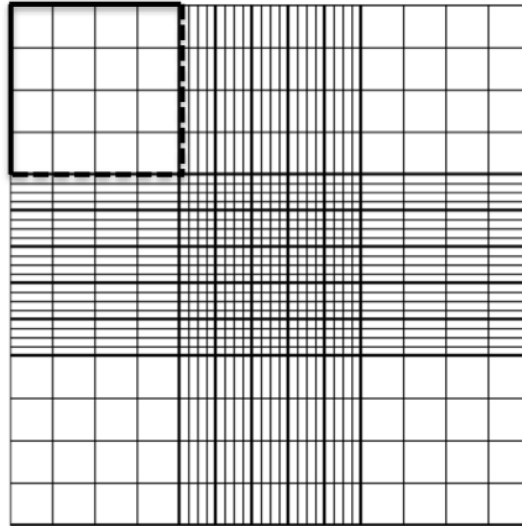


Figure 2.4: Illustration of cell counting grid of a haemocytometer (hemocytometer.com).

Once average cell count was obtained, it was used in Eqn 2.1 to calculate cell density in suspension.

$$\text{Cell density} = \text{Ave. Cell count} \times 10,000 \times \text{dilution factor} \quad 2.1$$

2.1.7 Long Term Cell Storage

Bacterial cells were grown for 8 hours in LB media, to mid exponential phase, which is optimal for cell storage. Glycerol is a commonly used additive for bacterial cell storage, as it prevents the formation of ice crystals during freezing. 0.5 mL of the 8 hours culture was added to 0.5 mL of 80% glycerol stock, to a final glycerol concentration of 40% (v/v) Cultures were then stored at -80°C. Cell viability was determined one week later by reviving a vial of the culture, by scraping the top of the vial with a sterile loop and spreading on a LA plate.

Mammalian cells were detached from the surface by trypsinisation as described in Section 2.1.6. Cells were counted as in Section 2.1.7 and $1.5-2 \times 10^6$ cells were added to a single 2 ml vial in full RPMI 1640 media along with 10% v/v dimethylsulphoxide (DMSO). As the freezing process is a stressful process to mammalian cells, a slow and constant freezing rate ensures cell viability upon revival. To ensure this, BAECs and BASMCs were stored in a Mr Frosty™ (Thermo Scientific, USA) freezing container containing isopropanol at -80°C , which freezes cells at a constant rate of $1^{\circ}\text{C}/\text{min}^{-1}$ for 24 hours. Vials were then transferred to a liquid nitrogen container for long term storage.

Stock viability was checked one week later by reviving a vial of the culture, which was quickly thawed in a 37°C water bath and 0.5 mL was used to inoculate 12 mL full RPMI in a T75 cell culture flask. Media was replaced no later than 24 hours revival, and cell viability was determined by cell attachment under light microscope. If culture viability was poor, the remaining vials of the particular stock would be suspended in RPMI and centrifuged to remove DMSO and any soluble apoptotic factors. The cell pellet was suspended in 1 ml full RPMI media and used to seed 1 T75 flask.

2.2 Electrochemistry

The potential range in the electrochemical techniques was selected to encompass both direct electron transfer (DET) and mediated electron transfer (MET) of the *S. oneidensis* culture. The potential poised during chronoamperometry (CA) was selected to maximise *S. oneidensis* attachment. Biofilm electrochemical behaviour was determined by cyclic voltammetry (CV) and presence of bound redox agents by differential pulse voltammetry (DPV). All potentials stated are versus an Ag/AgCl reference electrode.

2.2.1 Electrochemical Cell Set up

Potentiostat-controlled electrochemical cells (ECs) were chosen for our study. Single chamber, water-jacketed ECs with a working volume of 10 mL were operated in a three electrode configuration under the control of a five channel potentiostat (VSP Bio-Logic, USA).

The counter electrode was a 0.25 mm coiled titanium wire approximately 20 cm in length. The working electrode was either carbon felt (CF) or carbon cloth (CC) and had the dimensions 2 X 1cm. CF electrodes were washed with 1M HCl to removed metal ion contaminants and rinsed with DI water, while CC electrodes were rinsed with DI water. The working electrodes were connected to Ti wire current collector via miniature screw and nuts. The Ti wire current collector consisted of Ti wire soldered to copper wire in a 6.5mm glass capillary. The resistance of each working electrode assembly did not exceed 2.5 Ω for CF and 2 Ω for CC in each experiment.

The counter and working electrode were placed approximately 5 mm apart in the electrochemical cell. Ag/AgCl reference electrode ($E=+0.225$ vs. standard hydrogen electrode, SHE) (Als, Japan) was connected to a 3 mm Vycor frit (Bio analytical Systems, UK) via a salt bridge consisting of 0.1 M Na_2SO_4 in 1% agar. The Vycor membrane was boiled in 0.1M HCl to remove the oxide/Ag layer which may develop during biofilm growth/AgNP synthesis. Electrochemical cells were filled with DI water and wrapped with tinfoil to keep electrodes moist during autoclaving (121 $^{\circ}\text{C}$, 1 bar and 15 minutes). Agar salt bridge was added after autoclaving. To maintain anaerobicity, the top of the ECs were sealed with 2 sections of parafilm (American National Cam, USA). Fig. 2.5 shows the basic set of the electrochemical cell used in the study.



Figure 2.5: Electrochemical cell set up for *Shewanella* sp. biofilm growth

Before inoculation, the electrochemical cells set up was analysed by CA at -0.8 V, cyclic voltammetry (CV) and differential pulse voltammetry (DPV) with sterile fresh modified M1 medium to check the connections in the EC. If electrochemical noise were observed, the growth medium or the agar bridge was replaced. If the features persisted, the EC was discarded.

2.2.2 Cyclic Voltammetry

The theory of CV is explained in Chapter 3 and was performed to determine the electrochemical profile of the attached cells. The electrochemical potential applied to the system was scanned from $E_0 = -0.8$ V to $E_f = 0.2$ V at a scan rate of 1.0 mV.s and current monitored. The reverse scan ranged from $E_0 = 0.2$ V to $E_f = -0.8$ V. CV analysis occurred without stirring and under anaerobic conditions, to show diffusion limited reactions and minimise electrochemical noise.

2.2.3 Differential Pulse Voltammetry

The theory of DPV is explained in Chapter 3 and was performed to analyse bound redox mediators such as flavins. The potential range examined was between -0.8 V to $+0.2$ V. Pulse height was kept constant at 50 mV and pulse width at 200 ms, Step height was 2 mV and step time was 400 ms. A reverse scan was also performed from $+0.2$ V to -0.8 V. DPV analysis occurred without stirring and under anaerobic conditions, to show diffusion limited reactions and minimise electrochemical noise.

2.2.4 Chronoamperometry

The potential applied to the working electrode was poised at $+0.2$ V to favour electrode bioreduction and cell attachment. As the electroactive *S. oneidensis* cells attach to the surface of the working electrode and reduce it, an anodic (oxidation) current is produced. CA records this current vs. time, which gives a real time measurement of cell respiration rate. Current was recorded every 60 seconds during biofilm growth and AgNP synthesis. The reactor was stirred at 150 rpm with magnetic stirrer to lower mass transfer limitations.

2.3 Nanoparticle Biosynthesis

2.3.1 Bioelectrochemical Synthesis of Silver Nanoparticles

For biofilm mediated electrochemical synthesis, once the current reached a stable value, the spent growth medium was removed. 9 mL of a 100 mM HEPES buffer was added to cells and flushed with humidified N_2 for 10 minutes. The headspace of the reactor was constantly flushed with humidified N_2 to ensure constant anaerobic conditions. DPV was then performed once anaerobic conditions were created. 1 ml of an anaerobic 1 mM solution of $AgNO_3$ was then injected into the EC, and media flushed with N_2 to ensure anaerobic conditions for 5 minutes. The headspace of the EC was constantly flushed with N_2 and the working electrode was poised at a potential of either 0 , -0.2 or -0.4 V for 100 minutes. Open circuit voltage (OCV) was used as a control.

To determine if attached cell biomass is necessary, planktonic cells were examined for AgNP bioelectrochemical synthesis. 100mls of LB was inoculated with a loop of *S. oneidensis* from a 2 day old culture on a LA plate and incubated at 30 °C and 150 rpm for 22 hours. After incubation, the culture was centrifuged at 5,000 rpm for 10 minutes at 20 °C to pellet the cells. The cells were washed thrice to remove residual soluble flavins with 100 mM HEPEs buffer, and the cells were suspended at an $OD_{600nm} = 2$ in 100 mM HEPEs buffer. 9 mL of the resuspended culture was injected into sterile electrochemical reactors containing CF working electrodes along with 1 mL of a 10 mM solution of $AgNO_3$, and flushed with humidified N_2 gas to obtain anaerobic conditions. The working electrode was poised at a potential of either 0, -0.2 or -0.4V for 100 minutes.

For the abiotic control experiments, the procedure were carried out as stated before, only sterile electrodes with no biomass were used in the experiment.

2.3.2 Fungal Cell Surface Protein Synthesis of AuNPs

Following incubation, the surface protein (supernatant) was collected by centrifugation at 15,000 rpm for 20 min at 4 °C. Protein was analysed by bicinchoninic acid assay (BCA), and 3 mg of filter sterilised extract was added to a 10 mL solution of 0.5 mM $HAuCl_4$ in a 50 mM phosphate buffer (pH 7.2), followed by incubation at 30 °C for 30-72 h under shaking (150 rpm).

The synthesized AuNPs were collected by centrifugation at 20,000 rpm for 30 min at 4 °C to remove excess unreacted and loosely bound proteins from AuNP surface, and then the pellet was washed three times with DI water. The AuNP pellet was then resuspended in deionised water and analysed.

2.3.3 Mammalian Cell AuNP Biosynthesis

Confluent T-75 flasks were used to seed 6 well plates at approximately 60% confluency. BAECs and BASMCs were incubated in RPMI 1640 media supplemented with 10% v/v FBS and 1% v/v penicillin/streptomycin (P/S) antibiotic cocktail at 37 °C and 5% CO_2 until confluent. The media of the BAECs and

BASMCs was replaced with full RPMI media 1 day prior before Au exposure to increase repeatability.

Once confluent, the spent media was aspirated and washed twice with 1X PBS to remove any residual media, which may contain reducing agents. The BAECs and BASMCs were exposed to 0, 0.5, 0.75, 1, 1.5 or 2mM Au in or 1X PBS supplemented with 1% v/v FBS. To determine if the media can reduce Au ions, 0, 0.5, 0.75, 1, 1.5 and 2mM Au in either RPMI without glucose or phenol red, supplemented with 1% FBS or 1X PBS supplemented in 1X FBS, were incubated at 37°C and 5% CO₂ for 48 hours.

2.4 MNP Characterisation

In order to understand the mechanisms of MNP biosynthesis, and predict the physicochemical activity of the biogenic MNPs, a thorough understanding of the MNP characteristics is needed. MNPs were characterised by the SPR band, hydrodynamic size, particle size, crystal size, crystallinity and chemical composition. The theoretical basis of these techniques is described in Chapter 1, Section 1.2.

2.4.1 Isolation of MNPs

To ensure that the data from our analysis was for the MNP alone and not from the cell, a cell component or secretome, MNPs after synthesis were isolated in DI water. Unless stated, MNPs were collected and separated from the cells by centrifugation at 5,000 X rpm for 5 minutes at 4⁰C and MNPs were isolated by centrifugation at 13,500 rcf for 30 minutes at 4⁰C. The MNP pellet was rinsed thrice with DI water and then suspended in DI water.

2.4.2 U.V. visible spectrophotometry

Due to MNPs strong interaction with light, they can be detected due to their SPR band. Their SPR band position and shape may indicate MNP size and size distribution. To obtain the MNP spectra, 1.5 mL of the MNP sample suspended in DI water was analysed on a Cary 50 spectrophotometer (Varian, USA) at a step size of 0.1 nm and a scan rate of 10 nm.s⁻¹ at room temperature. For AgNPs, the samples were scanned between 700-350 nm and for AuNPs, the samples were scanned

between 800-400 nm. Wavelength range was selected to ensure that the SPR peak of well dispersed MNPs and MNP aggregates were detected.

To measure AuNPs associated with adhered BAECs and BASMCs, the cell associated AuNPs were analysed using a Tecan Infinite M200 plate reader (Tecan, Switzerland), scanning from 400-800 nm, in 1 nm steps and 25 flashes per step.

2.4.3 Dynamic Light Scattering

Protein capping and aggregation increase the hydrodynamic size of the MNPs. To measure the hydrodynamic size, 1 mL of the isolated MNPs was analysed in a 3 mL plastic cuvette using a Beckman Coulter Delsa Nano C Particle Analyser.

2.4.4 Transmission Electron Microscopy

MNPs due to their electron density will interact with an electron beam, and can be imaged in a TEM, which can be used to measure the particle diameter and observe the particle morphology. Isolated MNPs from the spent medium were drop dried onto carbon film coated copper TEM grids. The diameters of the MNPs were individually measured using Image J software (<http://imagej.nih.gov/ij/>).

2.4.5 Atomic Force Microscopy

MNP size may also be examined by atomic force microscopy (AFM). AgNPs were air dried onto 300 nm SiO₂ thermal oxide on Si wafer. The wafers were first scribed into 1 x 1 cm chips with a diamond scribe and sonicated for 15 minutes in a sequence of solvents (Ethyl lactate, Acetone, Methanol, Isopropanol) separately to remove dust followed by drying in an N₂ stream before use.

MNPs were analysed under ambient conditions on an Asylum Research Cypher-S AFM, using Budget Sensors MultiAI-75 silicon cantilevers (resonance 70-75 kHz) operating in repulsive tapping (AC) mode. Cantilevers were tuned to a frequency where the drive amplitude is 5% below the free air amplitude on resonance and imaged at 40-60% of the amplitude when driven at this frequency and imaged at scan speeds of 1-1.5 Hz. This analysis was done in the University of Nottingham by Alex

Summerfield. Height of the MNPs was individually measured using Gwyddion software (<http://gwyddion.net/>).

2.4.6 High resolution TEM and Selected area electron diffraction

Samples were air dried at RT on carbon film coated copper TEM grids, and examined under high resolution cryo-TEM (chilled by liquid nitrogen) by Yina Guo. Selected area electron diffraction (SAED) was also performed using the same HR-TEM. HR-TEM images were analysed using Image J software (<http://imagej.nih.gov/ij/>).

2.4.7 Base Piranha etching

In our previous work in Nottingham University, we encountered problems with spin coating samples on Silica wafers, possibly due to their hydrophobicity, which encourage material to be spun off the wafer rather than on. Etching the surface of the samples appeared to decrease the hydrophobicity of the wafer surface, encouraging material deposition. Silicon wafers were placed in a 3:1 mixture of ammonium hydroxide (NH₄OH) and hydrogen peroxide (H₂O₂) at 60 °C for 15-20 min. Then the silicon chips were washed with DI water and blown dry with N₂ gas.

2.4.8 Fourier transformed infra-red spectroscopy (FTIR)

The chemical nature of the MNP surface was examined by Fourier transformed infra red spectroscopy (FTIR). The solvent (DI water) was evaporated from the sample at 50 °C overnight. The dried MNP crystals was analysed between 4,500-500 cm⁻¹. The force gauge did not exceed 50%.

2.5 Cell Analysis and Biochemical Analysis

In order to understand the mechanism of MNP biosynthesis, both the MNPs and the cell should be analysed. Biochemical analyses were performed using standard protocols.

2.5.1 Biofilm Fixation and Dehydration

Electrodes post AgNP BES experiment were rinsed with 100mM HEPES buffer (pH 7) twice to remove loosely bound Ag. The electrodes with biofilm, were fixed with 5% glutaraldehyde in 100mM HEPES buffer (pH 7) for 30 minutes, and then immersed in 30%, 50%, 70%, 90% ethanol for 30 minutes and then 100% ethanol for an hour, twice. Sterile electrodes were air dried and analysed without fixation or dehydration.

2.5.2 Biofilm Carbon Coating

Electron microscopic analysis of insulating samples results in the build-up of electronic charge on the sample surface, which distorts the image. There are two methods to analyse insulating biological samples, either atmospheric pressure is varied during analysis which is termed variable pressure mode, which removes the build-up of charge however the image quality is negatively affected. Another option is to prevent the build-up of charge on the sample surface due, by coating the sample with a thin layer of a conductive material such as gold, silver or carbon.

A layer of a carbon was coated onto the CF electrodes with biofilm growth. EDX was also performed to determine Ag deposition. Biofilms on CF electrodes once fixed and dehydrated, were carbon coated with carbon lace at 0.1 mbarr of air.

2.5.3 Scanning electron microscopy and Energy Diffraction X-ray Spectroscopy

Scanning electron microscopy (SEM) of the working electrodes occurred in the School of Engineering in DCU. Samples were analysed by Zeiss EVO LS15 SEM at 100kX magnification. Energy Diffraction X-ray Spectroscopy (EDX) analysis of the electrodes utilised Panta FET Precision EDX detector, which was positioned at a 30° angle to the sample surface, and data analysed by INCA software. SEM images were analysed by Image J software (<http://imagej.nih.gov/ij/>).

2.5.4 Phase Contrast Microscopy

Samples were washed with 1 X PBS twice to remove residual AuNPs. They were then viewed under a 20 X objective lens.

2.5.5 Fluorescent Microscopy

4',6-diamidino-2-phenylindole (DAPI) is fluorescent stain, which binds strongly to A-T rich regions in the genome, and so is used to dye nuclei in mammalian cells. The number of DAPI stained nuclei can indicate the amount of cells attached to the surface of the plate, as most cells possess only one nucleus.

Samples were washed with 1 X PBS twice to remove residual AuNPs and media, and fixed for 20 minutes with 4% w/v formaldehyde in 1X PBS at room temperature. Residual formaldehyde was removed by washing cells thrice with 1X PBS. Nuclei were then stained with 1 µg/ml DAPI in 1X PBS for 15-20 minutes at room temperature and then washed thrice with 1X PBS to remove residual DAPI stain. Samples were immediately examined under blue filtered laser light.

2.5.6 Oxidative stress assay

ROS GLo™ H₂O₂ assay from Promega was used to determine oxidative stress in BAECs and BASMCs, and the non-lytic assay protocol was performed. Cells were plated at 60% confluency as in Section 2.1.6 in a 96 well tissue culture plate. Once confluent, the cells were exposed to 1.5 mM Au in 1X PBS or RPMI without phenol red and glucose for 18 hours. 20 µl of the H₂O₂ substrate buffer was added to each well and incubated as before for a further 6 hours. The conditioned media was taken and 100µl of the Ros_Glo™ detection solution was added in the wells of a black 96 well plate, and this was incubated in the dark for 20 minutes at room temperature. Relative luminescence units were recorded using a plate reading luminometer.

2.5.7 BCA Protein Assay

Protein concentration was analysed by the BCA protein assay. The assay works on the principle of Cu²⁺ reduction by the peptide bonds in proteins to Cu⁺ under alkaline conditions. The Cu⁺ ions react with bicinchoninic acid to form an intense purple complex in an alkaline environment, which has a strong absorbance at 562 nm. The assay is supplied in two separate reagents, an alkaline bicarbonate solution (reagent A) and a copper sulphate solution (reagent B).

To prepare a working solution, 50 parts reagent A was added to 1 part reagent B, and covered with tinfoil to protect it from light. The protein sample was diluted by factor of 1:10 to dilute any possible interfering agents that may be present in the sample. In a well of 96 well plate, 20 μ L of the diluted protein sample or BSA protein standard was incubated with 250 μ l of BCA working reagent and was incubated at 60 °C for 30 minutes wrapped in tinfoil, and was then allowed to cool to RT and absorbance measured at 562 nm using a Tecan Infinite M200 plate reader, with 25 flashes per well. A standard curve of known BSA concentrations (0.1-2mg mL⁻¹) was used to calculate the protein concentration

2.5.8 Protein concentrator

The above protein extraction methods resulted in insufficient protein concentration in the extract. Therefore the protein extracts required concentration, however the concentration method must not affect protein structure. Centrifugal concentration uses a selectively permeable membrane in a centrifuge tube to filter a protein solution, where the proteins higher than the molecular weight cut off point (MWCO) are retained in the retentate and are concentrated. Fungal protein extracts were concentrated using a Vivaspin 20 (MWCO 10,000Da) centrifugal concentrator. They were centrifuged at 4,000 rpm for 30 minutes at 20°C.

2.6 MNP activity

MNPs possess a variety of applications. Our research group is mostly interested in water treatment, therefore this study focused on the antibacterial activities of the MNPs produced.

2.6.1 Anti-bacterial assay

As inocula size affects metal toxicity, the *E.coli* inocula was standardised before the growth curve assay. A single colony of *E.coli* was used to inoculate 10mls of Luria broth and incubated at 30°C and 150rpm overnight. The overnight LB *E.coli* culture was brought to an OD_{600nm} and used as 10% v/v inoculum in M9 media. Fungal protein extract synthesized AuNPs were diluted in DI water to reached a SPR peak height of 0.1. This was added to the *E. coli* culture at a 10% v/v dilution and incubated aerobically for 24 hours at 30 °C and 150 rpm. 10% DI water was used as

a control. Samples of the culture were taken at 1, 4, 6, 8, 12 and 24 hours and OD_{600nm} was recorded.

2.7 Data Analysis

Electrochemical cell data was exported as an ASCII file by EC Lab Data (Bio-Logic). U.V. spectral data was exported as an ASCII file by Varian UV. Software.

ASCII files were analysed by Origin Pro (ver. 8.5) software. U.V. visible spectra and DPV data were subjected to base line subtraction to standardise the data.

MNP size data was analysed by Origin Pro (ver. 8.5) software. Mean sizes were averaged over n=3 independent biological replicates.

Exponential microbial growth rate constant was calculated on Excel 2010 software.

2.8 Media Recipes

All media recipes are standard microbiological media and used bacteriological grade components were possible.

2.8.1 Sterilisation and Glassware preparation

All glassware used for MNP biosynthesis was either washed with 3M Nitric acid for AgNPs or 3M Aqua regia (3:1 ratio of 3M HCl and 3M Nitric acid) for AuNPs.

Unless stated otherwise, all buffers, solutions and media were sterilised by autoclaving at 121 °C for 20 minutes at 1.5 psi, in a Classic Prestige Medical 1L autoclave (Presige Medical Ltd, UK).

Metal salts ($HAuCl_4$ and $AgNO_3$) were sterilised through a 0.2 μm filter instead of autoclaving to avoid metal ion reduction, and stored at 4 °C in the dark.

2.8.2 Luria Broth/Agar

Luria Broth or Luria Agar (LB or LA) was prepared by adding the components in Table 2.1 to DI water. Iron citrate, which was added to indicate the presence of *Shewanella* cells, which grew orange/pink (see Fig 2.4). pH of the solution was adjusted to 7.2 using 1M NaOH and 1M HCl. MgSO₄ and CaCl₂ were added only immediately before inoculation (MgSO₄ and CaCl₂ stocks were filter sterilised through a 0.2 µm filter).

Table 2.1: Media recipe for Luria Broth and Luria Agar

	Concentration (gL ⁻¹)
Bacteriological grade tryptone	10
Yeast extract	5
Sodium chloride	5
Iron citrate	0.1
Agar (For LA preparation)	15
Magnesium sulphate	0.024
Calcium chloride	0.001

LA plates were prepared by pouring 20mls of autoclaved LA into a 90 X 15.88 mm petri dish (Lennox) once cooled to temperature at which it can be handled comfortably. The plates were allowed to set with lid slightly ajar, to avoid excessive condensation in the plate, in the Microflow Laminar Flow hood. Plates were then incubated at 30° overnight to screen plates for contamination. Plates were sealed with parafilm and then stored at RT, as storage at 4 °C induced condensation in the plate, which increased the risk of contamination. Excess LA was stored in a water bath at 60 °C to prevent agar from setting and to avoid agar reboiling which caramelises the sugars in the medium.

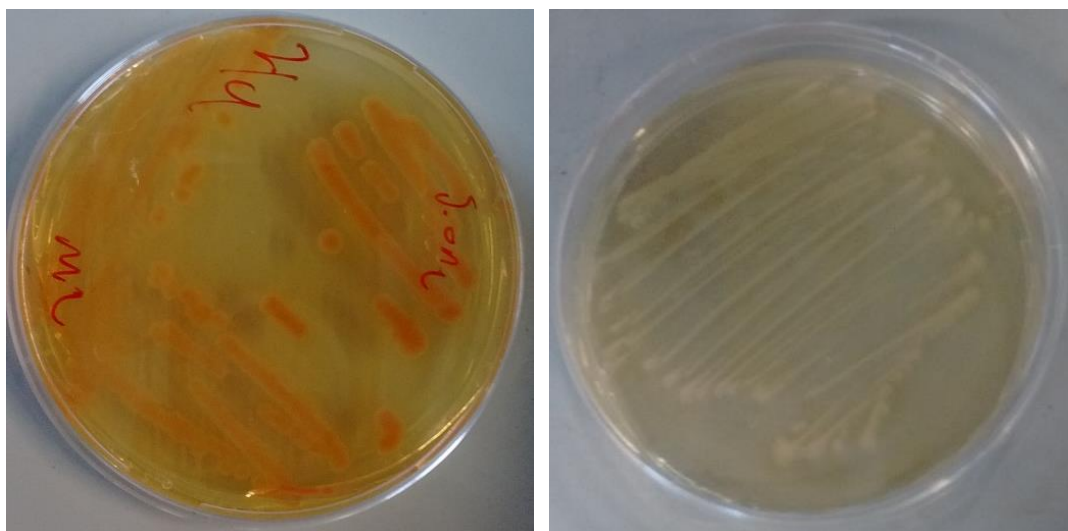


Figure 2.6: (A) *S. oneidensis* and (B) *E. coli* grown on LB supplemented with 0.1 g/L iron citrate

2.8.3 M9 Medium

M9 medium was prepared by adding the components in Table 2.2 to DI water. Diluted M9 salt solution was sterilised in by autoclaving. Glucose, magnesium sulphate and calcium chloride were added via a 0.25 μm sterile filter. The media was stored at 4 $^{\circ}\text{C}$

Table 2.2: Media recipe for M9 medium

	Concentration (mgL^{-1})
5X M9 salt solution	20% v/v
Glucose	4
Magnesium sulphate	24
Calcium chloride	1

2.8.4 Modified M1 medium

Modified M1 medium was prepared by adding the components in Table 2.3 to DI water. The solution pH was adjusted to 7.0 using 1M NaOH and 1M HCl. Immediately before inoculation, CaCl_2 stocks were filter sterilised through a 0.2 μm filter.

Table 2.3: Media recipe for Modified M1 medium

	Concentration (g.L ⁻¹)
HEPEs	7.2
Sodium hydroxide	0.3
Ammonium chloride	5
Potassium chloride	0.1
Sodium dihydrogen phosphate	0.52
100X amino acid solution	1% v/v
100X vitamin solution	1% v/v
100X mineral stock solution	1% v/v
Sodium lactate	20 mM
Calcium chloride	0.001

2.8.5 Potato Dextrose Broth/Agar

Potato dextrose broth (PDB) and agar (PDA) were prepared by adding the components listed in Table 2.4 to DI water. The pH was adjusted to 5.2 with 1M NaOH and 1M HCl. For agar preparation, 15g/L agar was added prior to autoclaving.

Table 2.4: Media recipe for Potato Dextrose broth/Agar

	Concentration (g.L ⁻¹)
Potato extract	15
Dextrose	20
Agar for (PDA preparation)	15

2.8.6 100X Amino acid stock

To create a 100X amino acid stock solution the components listed in Table 2.5 were added to DI water. Stock was then stored at 4°C

Table 2.5: Componentets of 100X Vitamin Stock

	Concentration (g.L ⁻¹)
L-Glutamic acid	2
L-arginine	2
DL-serine	2

2.8.7 100 X Vitamin Stock

To create a 100X vitamin stock solution the components listed in Table 2.6 were added to DI water and stirred for 10 minutes. pH was adjusted to 8.0 using 1M NaOH and 1M HCl. Stir until all components are completely dissolved. Adjust pH to 7 using 1M NaOH and 1M HCl, if necessary. Stock was stored at 4 °C.

Table 2.6: Componentets of 100X Vitamin Stock Solution

	Concentration (mg.L ⁻¹)
d-biotin	2
folic acid	2
pyridoxine HCl	10
riboflavin	5
thiamine HCl hydrate	5
nicotinic acid	5
d-pantothenic acid hemicalcium salt	5
B12	0.1
p-aminobenzoic acid	5
thioctic acid	50

2.8.8 100 X Mineral stock

To create a 100X mineral stock solution the components listed in Table 2.7 were added to DI water and pH adjusted to 7 using 1M NaOH and 1M HCl and stored at 4°C.

Table 2.7: Components of 100X Mineral Stock Solution

	Concentration (g.L ⁻¹)
Nitrilotriacetic acid	1.5
MgSO ₄ .7H ₂ O	3
MnSO ₄ .H ₂ O	0.5
NaCl	1
FeSO ₄ .7H ₂ O	0.1
CaCl ₂ .2H ₂ O	0.1
CoCl ₂ .6H ₂ O	0.1
ZnCl ₂	0.13
CuSO ₄ .5H ₂ O	0.01
AlK(SO ₄) ₂ .12H ₂ O	0.01
H ₃ BO ₃	0.01
Na ₂ MoO ₄ .2H ₂ O	0.025
Na ₂ WO ₄ .2H ₂ O	0.025

2.8.9 5X M9 salt stock

To create a 100X mineral stock solution the components listed in Table 2.8 were added to DI water.

Table 2.8: Components of 100X Mineral Stock Solution

	Concentration (g.L ⁻¹)
Disodium hydrogen phosphate	64
Potassium dihydrogen phosphate	15
Sodium chloride	2.5
Ammonia chloride	5

Chapter 3: Bioelectrochemical Synthesis of Silver Nanoparticles

Biosynthesis of metal nanoparticles (MNP) might provide a suitable synthetic route for in situ application, such as bioremediation, sterilization, etc. The biosynthetic process employing cell-free extract produces MNPs with an acceptable size and shape distribution in short time. However, biosynthetic process using viable cells are more appealing for in situ application, due to their lower cost and self-sustainability. In the latter process, size and shape of biosynthetic MNP are hard to control. In this study, we use electrochemical potential to drive the MNP biosynthetic process, thus improving size distribution of AgNPs in *Shewanella* sp. viable culture. We tested the process in both biofilms and planktonic cells. Results show that the biosynthesis time is lowered from over 48 hours to 100 minutes. Possible developments for a novel bioelectrochemical process are envisioned.

3.1 Introduction

3.1.1 Electroactive Bacteria

There are two broad classifications of electroactive bacteria, depending on how they interact with an electrically charge electrode surface. If the bacterium utilises the electrode surface as an electron donor, they are classified as an electrotrroph. However if they utilise the electrode surface as an electron acceptor, they are classified as an electrogen. This chapter will examine electrogens.

The ability of bacteria to generate an electrical current in microbial fuel cells (MFCs) has been uncovered in organisms such as *E. coli* (Masih et al., 2012), *P. aeruginosa* (Pham et al., 2008), as well as members of the *Clostridium* (Mathuriya and Sharma, 2009), *Desulfovibrio* (Cordas et al., 2008), *Shewanella* (Newton et al., 2009) and *Geobacter* (Cordas et al., 2008) genus. While *Desulfovibrio*, *Shewanella* and *Geobacter* sp. are considered electroactive bacteria, *E. coli* and *P. aeruginosa* are not as their current generation ability is not due to an extracellular electron transfer (EET) mechanism, but as a result of the secretion of compounds such as phenazines, whose main biological function is an intracellular signal to regulate biofilm formation and architecture (Pierson, 2010).

EET is a mechanism evolved by electroactive bacteria to survive in low oxygen environments. This mechanism gives the bacteria the ability to transfer its metabolically generated electrons to terminal electron acceptors such as Ag (Wang et al., 2009), Au (Suresh et al., 2011), Pd (Windt et al., 2005), U (Marshall et al., 2006), or organic compound such as DMSO (Gao et al., 2006). Small inorganic molecules such as nitrate, nitrite or insoluble minerals as Mn (IV) or Fe (III) may be used as terminal electron acceptors. In nature, these bacteria form a biofilm around inorganic mineral deposits. This project utilized the bacterium *Shewanella oneidensis* MR1, as its EET mechanism is well characterised and is easier to work with compared to members of the *Geobacter* genus.

3.1.2 Extracellular Electron Transfer

There are two main mechanism of extracellular electron transfer (EET) utilized by electroactive bacteria, either through direct contact with outer membrane cytochromes or through soluble secreted redox mediators such as flavins. Fig. 3.1 illustrates the main mechanisms of EET in *S. oneidensis*.

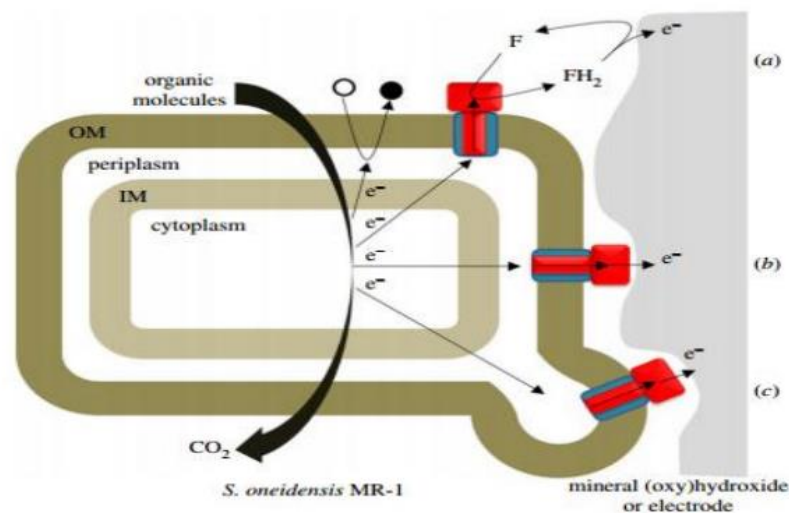


Figure 3.1: EET can occur either through (a) soluble flavins, (b) direct contact with OMC cytochromes or (c) cytochromes located on outer membrane extensions nanowires. (A) is termed mediated electron transfer (MET) while (B-C) is referred to as direct electron transfer (DET) (Breuer et al, 2015).

Direct electron transfer (DET) occurs through direct contact between the electron acceptor and the outer membrane cytochrome. In *S. oneidensis* the cytochrome is a complex known as the mtrC/omcA cytochrome complex. This complex is responsible for the transport of electrons through the outer membrane to the extracellular electron acceptor, as illustrated in Fig. 3.2. The mtrC/omcA is comprised of 4 protein subunits, mtrA, mtrB, mtrC and omc A (Shi et al., 2009).

MtrC and omcA associate to form a terminal cytochrome complex facing the extracellular environment. FLASH-labelled mtrC protein extract showed that upon addition of purified omcA, the steady state fluorescence polarisation increased progressively from 1.75 mP to a limiting value of 2.3 mP. As a control, mtrA was added, which did not affect the polarisation, however addition of salt decreased the polarisation, suggesting the omcA and mtrC binding is both specific and mediated in part by electrostatic interactions. Further when the bind affinities were calculated using the Hill equation (Eqn 3.1), the apparent dissociation constant (K_d) was found to vary between 0.5 and 1.0 depending on salt concentration and the Hill coefficient (n) was 1.6 (Shi et al., 2006) .

$$OmCA_{bound} = \left[\frac{[OmCA_{free}^n]}{K_d + [OmCA_{free}^n]} \right] X Max + Min \quad (3.1)$$

MtrA is periplasmic facing decaheme cytochrome, which receives electrons from CymA and transports them to the mtrC via electron hopping between the Fe residues located in the heme groups of the protein. MtrB is a β barrel porin, which spans the outer membrane and allows the periplasmic facing mtrA to come into contact and transfer electrons to the extracellular facing mtrC as shown in Fig. 3.2.

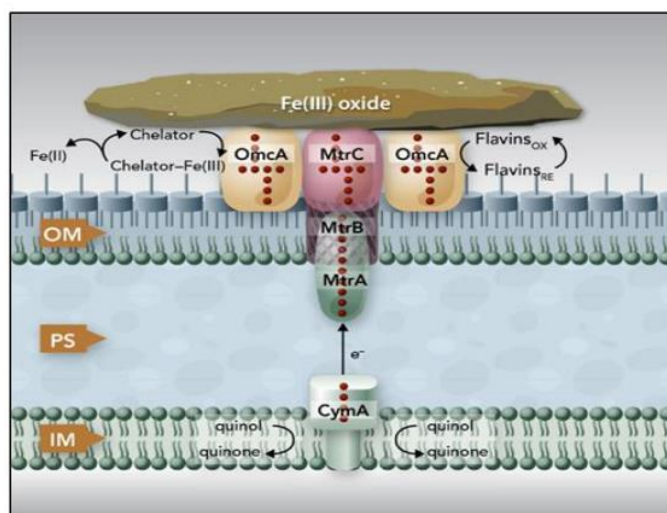


Figure 3.2: Diagram of the omcA/mtrcA cytochrome complex in *S. oneidensis* (Shi et al., 2009) .

Shewanella sp. secretes flavins which behave as extracellular redox shuttles, which transfer electrons from the mtrC/omcA complex to terminal electron acceptors. This is termed mediated electron transfer (MET). Replacement of medium with fresh media when the current stabilised showed an immediate decrease in current output of an *S. oneidensis* biofilm by $73 \pm 4.5\%$, which suggested that soluble mediator was involved in EET. Current was restored to $94 \pm 6.1\%$ of the original value, when the spent medium was centrifuged to remove planktonic cells and returned to the chamber. CV showed that the anodic current production decreased with the addition of fresh medium, while the addition of 250nm riboflavin (RF) to an established steady state biofilm increased anodic current production. Differential pulse voltammetry revealed peaks at -0.2 volts (indicative of flavins), which increased rapidly from $0\mu\text{A}$ to $\sim 200\mu\text{A}$ after 4 hours. Media exchange of biofilms less than 3 days old, lead to a decrease in the flavin peak by 70% approximately, indicating a portion of flavins are absorbed on to the electrode surface. However older biofilms (> 6 days) only showed a 30% decrease in this peak and only 50-60% drop in anodic current production (Marsili et al., 2008). This suggests that the dominant EET mechanism in *S. oneidensis* shifts towards DET from MET as the biofilm increases in age.

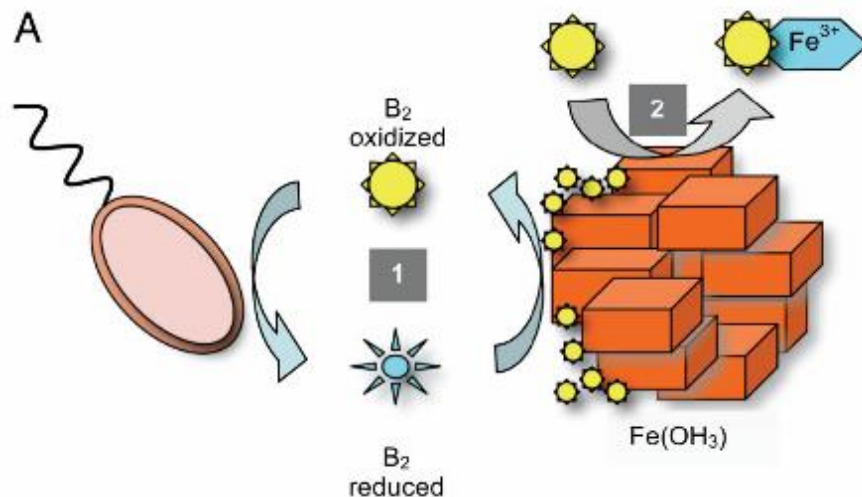


Figure 3.3: Mediated electron transfer by *S. oneidensis* (Marsili et al., 2008)

Although biofilms can carry out EET past the diffusion limits of MET, the mechanism has been a topic of much discussion. Nanowires have been proposed to address this problem, although the existence and identity of nanowires has been a topic of much debate in the literature. Studies have indicated the identity of the bacterial nanowires were bacterial appendages such as pili or flagella, due to their decreased current generation ability upon knock out of these structures. CV analysis of wild type *S. oneidensis* and knock out mutants of the type IV pilus ($\Delta pilM-Q$), flagella (Δflg), $\Delta mtrC/\Delta omcA$, mannose sensitive hemagglutinin pilus ($\Delta mshH-Q$) and a double knock out of $\Delta pilM-Q/\Delta mshH-Q$, which showed that the max current density for the wild type was $7.9 \pm 1.5 \mu A.cm^{-2}$. Only the $\Delta mtrC/\Delta omcA$, $\Delta mshH-Q$ and $\Delta pilM-Q/\Delta mshH-Q$ showed significantly decreased current density. While the Δflg knockout increased the current density to $9.5 \pm 2 \mu A.cm^{-2}$, this is not statistically significant. CV of the biofilms under non turnover conditions show that all mutants showed a decrease in anodic current production except the $\Delta mshH-Q$ mutant, while all mutants with the exception of $\Delta mshH-Q$ and $\Delta pilM-Q$ showed a decrease in cathodic current production. For turnover conditions, CV reveals that anodic current generation was lower for all mutants except the $\Delta pilM-Q$ and Δflg , which is in accordance to the max current density recorded by chronoamperometry. Interestingly the cathodic current did not decrease for any mutant, further the cathodic current increased for the $\Delta pilM-Q$ mutant. The relative contribution of DET and MET to

current generation did not significantly change between mutants and the wild type (Carmona-Martinez et al., 2011).

However further study reveals that, these appendages are not involved in electron transfer and that the observed decrease in current density was due to their role in bacterial cell attachment to the electrode surface. NanoOrange *in vivo* staining of *S. oneidensis* under oxygen limited conditions shows that *S. oneidensis* forms nanofilaments between adjacent cells which contain proteins. Co-staining with the FM 4-64FX (lipid dye), reveals that these filaments are outer membrane extensions. MtrC and omcA were show to present in these extensions by immunocytochemistry (Fig 3.4b) (Pirbadian et al., 2014). Although their existence has been demonstrated, the relative contribution of these nanowires to current production in MFCs is still relatively unknown.

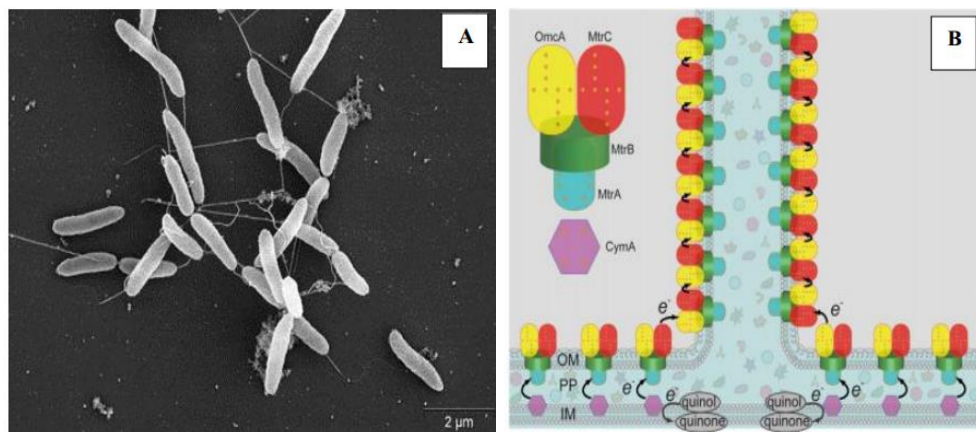


Figure 3.4: (a) SEM images of *S. oneidensis* nanowires and (b) proposed structural model for these nanowires (Pirbadian et al., 2014).

3.1.3 Biofilm Formation

In nature, microbes exist in a complex microbial community attached to a large surface known as a biofilm. Up until recently biofilms were considered a detriment for biotechnological processes. A summary illustrating the formation of a biofilm is shown below in Fig. 3.5. However in recent years, the use of biofilms for bioremediation (Singh et al., 2006) and potential for industrial biocatalysis applications (Rosche et al., 2009) has attracted much research interest. However in order to predict and control biofilm activity and structure, we must first understand

how the biofilm develops. This section summarises what is known about the development of *S. oneidensis* biofilms.

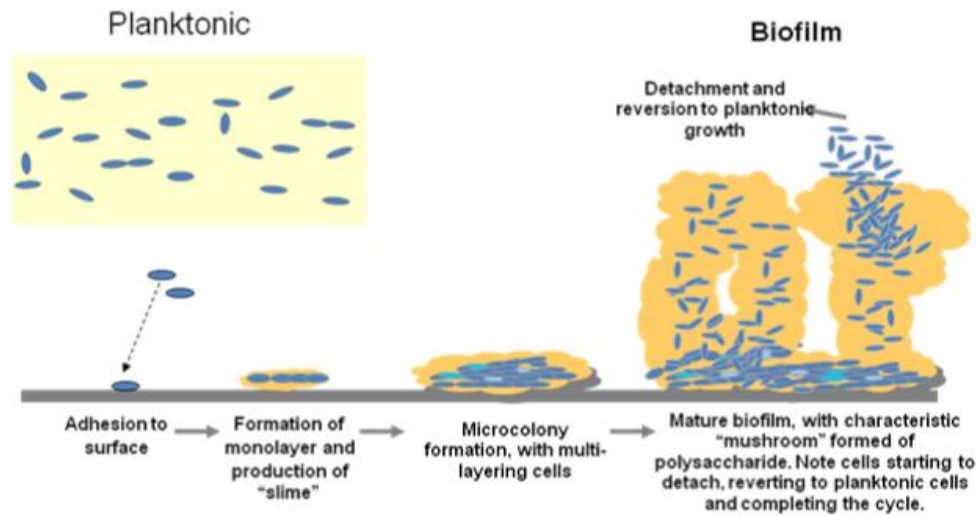


Figure 3.5: Illustration of the general mechanism of biofilm formation

The first step in biofilm formation is the release and detection of a threshold concentration of an intercellular signal, which is termed quorum sensing. This has been very well studied in medically relevant biofilm forming species such as *P. aeruginosa*. Acyl-homoserine lactone (AHL), a commonly used quorum signal in gram negative bacteria, was found to not be present in the supernatant of both an aerobic and anaerobic *S. oneidensis* culture using *A. tumefaciens* NTL4(pCF218)(pCF372) and *E. coli* MG1655(pJWP01s) reporter strains. In the same study, mutation of the *luxS* decreased the adhered biomass of *S. oneidensis* by 34%, as measured by crystal violet staining. Upon the reintroduction of *luxS* by plasmid borne *luxS* complementation, the adhesion of *S. oneidensis* biomass was recovered to the same level as the control experiments. Aerobic and anerobic growth curves of the mutant show that the growth rate was not affected, and the mutation specifically affected biofilm formation. Supplementation with synthetic AI-2 did not restore biofilm forming ability of the mutant, however supplementation with homocysteine (HCY) seemed to complement biofilm formation for the mutant, which seems to suggest that the *luxS* mutant negatively impacts S-ribosylhomocysteine (SRH) conversion to HCY and 4,5-dihydroxy-2,3-pentanedione (DPD). Growth curves of *S. oneidensis* in sulphur limited media show that

methionine metabolism in the activated methyl cycle (AMC) of the *luxS* mutant is disrupted (Learman et al., 2009).

Nitric oxide has been demonstrated to induce biofilm formation. H-NOX, a sensor protein for NO inhibits autophosphorylation HnoK leading to inactivation of HnoB, which increases intracellular c-di-GMP, which is an intracellular signal involved in biofilm formation. Addition of a NO release compound, DETA NONOate lead to a significant increase in biofilm formation for wild type *S. oneidensis*, 1.3 ± 0.3 (OD_{570}/OD_{600}) with 200 μ M DETA NONATE v.s. 0.6 ± 0.1 control 0 μ M DETA NONATE. $\Delta hnoX$, $\Delta hnoK$ and $\Delta hnoD$ deletion mutants showed significant decrease in biofilm formation when stimulated with 200 μ M DETA NONATE, with an OD_{570}/OD_{600} of 0.8 ± 0.2 , 0.8 ± 0.2 and 1 ± 0.2 respectively, which is comparable to their 0 μ M DETA NONATE control. Further when unstimulated with 0 μ M DETA NONATE, the knock outs except $\Delta hnoD$ showed no significant difference when compared to the wild type unstimulated. This indicates that $\Delta hnoX$ and $\Delta hnoK$ are specific for NO. Fig. 3.6 shows the hypothesized model of NO induction of *S. oneidensis* biofilm development (Plate and Marletta, 2012). This NO induction of *S. oneidensis* biofilm formation may be a defense mechanism against the free radical.

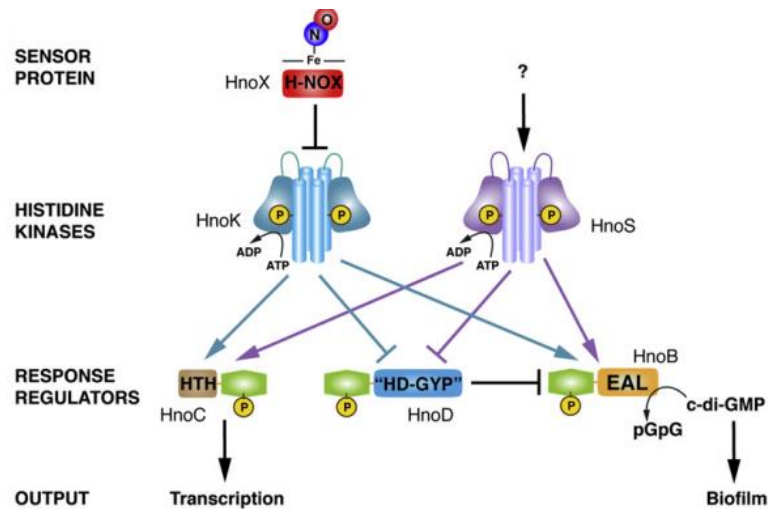


Figure 3.6: Model of NO induction of biofilm formation in *S. oneidensis* (Plate and Marletta, 2012)

Bond formation between the *mtrC* and *omcA* cytochromes and hematite was demonstrated by AFM. Interestingly the attractive force between the *omcA* and hematite was twice the attractive force than the *mtrC* and hematite, however the *mtrC* bond is more resilient (Lower et al., 2007). Further biofilm architecture of *S. oneidensis* was disrupted when the mannose sensitive hemagglutinin type IV pilus (*mshA*) and pilus retraction (*pilT*) genes were mutated (Thormann et al., 2004). These results suggest there are multiple attachment factors on the surface of *S. oneidensis* cells.

3.1.4 Bioelectrochemistry and Bioelectrochemical Reactors

Bioelectrochemistry examines redox reactions in biological systems such as proton transport, cell membrane potentials and EET. For our purposes, we will be focusing on the topic of microbial EET. There are many experimental factors that influence EET, which are the microbial inoculum, temperature, pH, presence of oxygen and reactor configuration. This section outlines the basic configuration of the electrochemical cell and examines the influence of reactor design on EET.

3.1.5 Electrochemical Cell Set Up

The basic electrochemical reactor configuration is illustrated in Fig. 3.7. A reference electrode is used to keep potential of the working electrode constant. During the course of the experiment, the ionic strength of the solution decreases, leading to a decrease in current. A salt bridge is added to ensure that the ionic strength of the solution is kept constant. The microbial consortia attach to the working electrode and generate electrons, bicarbonate and protons. The cations produced diffuse to the counter electrode and are reduced by the electrons generated by the microbial consortia. The reactions at the anode and cathode are summarised in Eqn 3.2 and in Eqn 3.3 respectively (Logan et al., 2006).

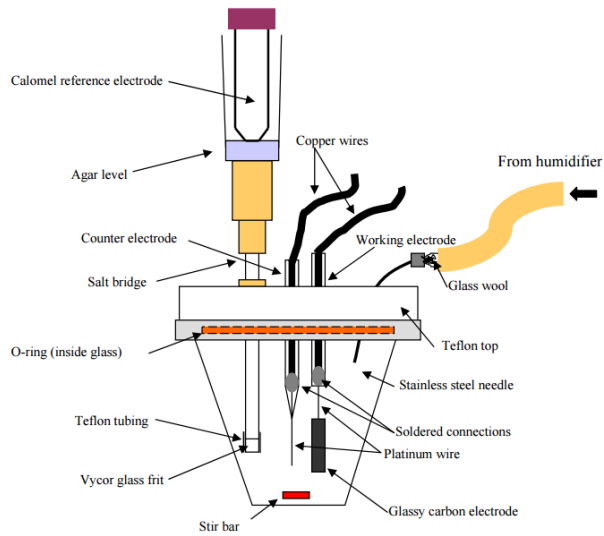
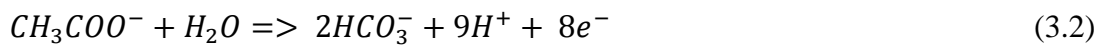


Figure 3.7: Electrochemical cell set up for *Shewanella* sp. biofilm growth (Marsili et al., 2008)



The operational principle of current generation is outlined in Fig. 3.8.

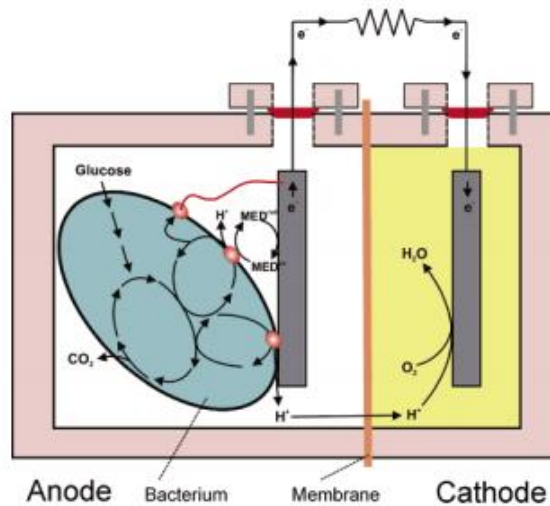


Figure 3.8: Operation principles of a MFC (Logan et al., 2006) .

The bioelectrochemical reactions can be influenced by a variety of factors such as temperature, applied electrochemical potential and electrochemical cell set up. This section shall examine the key design choices and their influence on BES.

3.1.5.1 Electrode Material

The electrode material is one of the most important parameters in a bioelectrochemical experiment. The ideal electrode should be highly porous for maximum biomass attachment, conductive for low over potentials and have low cost for cost effective scale up for industrial applications. Carbon materials are preferred as anodes due to their low cost and high biocompatibility. Graphite coated with carbon nanotubes (CNTs) offers the best performance to date, however the cost associated with the production of CNTs is too high for commercial applications. Graphine sponge has a lower cost, but is less conductive. Carbon felt, due to its large surface area produces high current density in MFCs.

3.1.5.2 Electrode Pretreatment

Electrode pretreatment has been examined to decrease over potentials and increase productivity in MFC and BES systems. The ideal treatment should be cheap, fast and safe while producing high current density. Plasma pretreatment is a cheap and safe method for the deposition of functional groups onto inorganic surfaces, such as electrodes and has been shown to increase cell attachment. Nitrogen and oxygen plasma pretreatment of a glassy carbon electrode increased anodic current generation. The lag phase of biofilm development also decreased from 4.8 days to 4.5 days for oxygen plasma pretreatment and 3.3 days for nitrogen plasma pretreatment (Flexer et al., 2013). Atmospheric air plasma treatment of graphite and carbon felt anodes increased maximum current production from *Shewanella loihica* PV4 biofilm during the early biofilm development stage. This was due to the increased hydrophobicity favouring cell attachment, however the coulombic efficiency (CE) decreased by 60% (Epifanio et al., 2015).

3.1.5.3 Electrochemical Cell

The standard dual chamber electrochemical cell is used primarily in BES experiments under anaerobic conditions to prevent the H^+ ions reacting with O_2 to produce H_2O (Croese et al., 2014), (Zhan et al., 2014), (Sasaki et al., 2012). The anode and cathode are usually separated by a proton (Sasaki et al., 2012) , anion (Zhan et al., 2014) or cation (Croese et al., 2014), (Sakai and Yagishita, 2007) exchange membrane to maintain redox gradients and prevent crossover reactions (Krieg et al., 2014), where mixing of the anode and cathode compartments leads to the formation of mixed potentials and internal currents which causes the depolarisation of the electrode (Harnisch et al., 2009) as observed for Pt based cathodes in methanol fuel cells (Ren et al., 2000).

In certain cases, membranes can be eliminated, to simplify the design and to reduce costs. Sasaki et al demonstrated that the membraneless H-type dual chamber electrochemical reactor produces biogas with similar H_2 content to the anode compartment of a H-type dual chamber cell with a proton exchange membrane ($54.4 \pm 9.5\%$ v/v vs $42.6 \pm 4.5\%$ v/v respectively) when the working electrode was poised at $-0.9V$ (vs. Ag/AgCl) (Sasaki et al., 2012) .

A single chamber is a simpler design for scale up, and shows similar performance as the H type dual chamber. A single chamber electrochemical reactor (Fig. 3.9) had a H_2 bioelectrochemical production rate of $2,196 \text{ mL}^{-1}\text{day}^{-1}$ for a single chamber vs. $2,445 \text{ mL}^{-1}\text{day}^{-1}$ for the H type dual chamber cell. The electrodes were only 2 cm distant in the single chamber MEC, thus resulting in higher current and H_2 production (Sasaki, Morita, D. Sasaki, et al., 2012). This relationship between electrode spacing and BES performance production was also demonstrated by Cheng and Logan, using single chamber MECs, fitted with graphite fibre anodes and carbon cloth anodes (Cheng and Logan, 2011). Small distance between electrodes should be taken into consideration for MEC design, due to the decrease in ohmic resistance and the resulting increase in current.

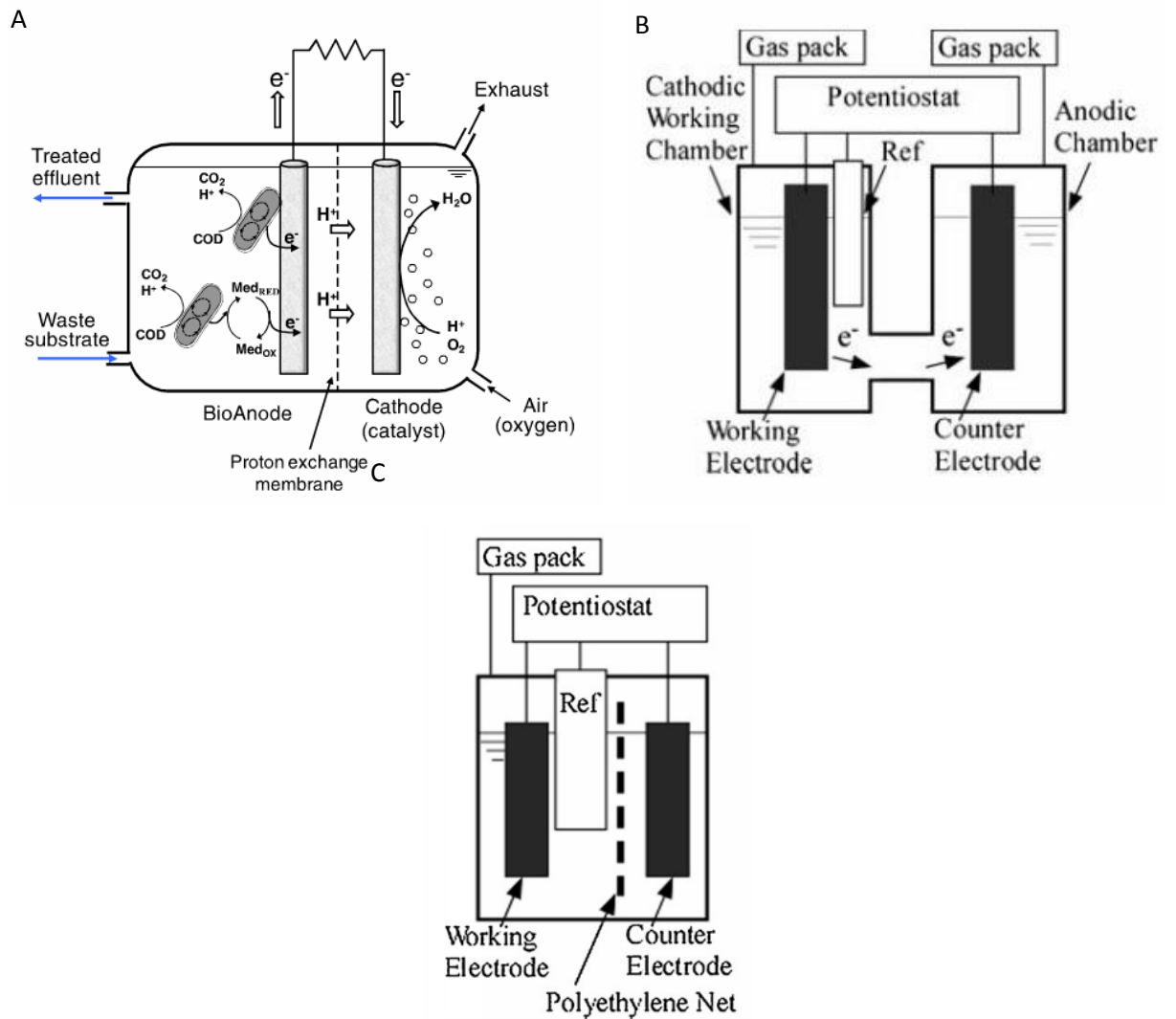


Figure 3.9: Schematics of electrochemical designs used in BES reports. (a) Dual chamber electrochemical cell fitted with proton exchange membrane (Villano et al., 2012), (b) H type dual chamber membraneless bioelectrochemical reactor (Sasaki et al., 2012) and (c) single chamber electrochemical reactor (Sasaki, et al., 2012).

3.1.6 Introduction Electrochemical Methods

Redox reactions of bioelectrochemical systems can be investigated using electrochemical methods. This section summaries the basic theory of the electrochemical methods utilised by this study.

3.1.6.1 Cyclic Voltammetry

Cyclic voltammetry is used in bioelectrochemistry to probe the electron transfer mechanism of the attached microbial community to/from the electrode surface (Carmona-Martinez et al., 2011; Epifanio et al., 2015). For our purposes, CV is performed upon inoculation of the electrochemical cell and under non-turn over conditions to determine if the attached biomass culture is sufficiently electrochemically active.

In this technique the potential of the working electrode is varied between two arbitrary potentials, E_1 - E_2 (forward scan) which covers the region of interest. Once E_2 is reached, the potential is swept back from $E_2 - E_1$ (reverse scan). Current is then plotted as a function of the applied potential, in which fully electrochemical reversible behaviour may be determined through the appearance of peaks in the forward and reverse scan that are within 60mV of each other.

This technique is performed under non stirring conditions; therefore diffusion may affect the intensity of the current measured for homogenous conditions, depending on the nature of the electrochemical reaction, reversible vs. non-reversible behaviour. To illustrate the difference, for a simple homogenous electrochemical reaction $A + e^- \Rightarrow B$, before the start of the peak, the potential is not sufficient to significantly reduce A to B, therefore current is low. At the start of the peak, A is beginning to be reduced to B, creating a diffusion layer, where the concentration of A is low. At the peak maximum, the diffusion layer has thickened, leading to a subsequent decrease in current as the diffusion becomes the rate limiting step in the reaction. As the diffusion layer increases, the diffusion of solute A decreases as

$$J = \frac{D_A}{\gamma} \Delta A \quad (3.4)$$

J = mass transfer flux ($\text{moles}\cdot\text{m}^{-2}\cdot\text{s}^{-1}$), D_A = diffusion coefficient ($\text{m}^2\cdot\text{s}^{-1}$) of A, ΔA = concentration difference of A between the interface of the diffusion layer and bulk solution and the interface of the surface of the electrode and diffusion layer ($\text{moles}\cdot\text{m}^{-3}$) and γ = diffusion layer thickness (m). For irreversible behaviour, the electrode kinetics are too low, which causes diffusion to become a rate limiting step. In this case, a significant potential over the thermodynamic limit is required to reduce A or oxidise B. However for reversible electrochemical behaviour, the electrode kinetics are sufficient to allow the system to follow the Nernst equation (Eqn 2.2).

$$E = E_f^0 \left(\frac{A}{B}\right) + \frac{RT}{F} \ln \frac{[B]_0}{[A]_0} \quad (3.5)$$

Cyclic voltammetric analysis under non turn over conditions is used to determine the inherent anodic and cathodic current of the attached biomass.

3.1.6.2 Differential Pulse Voltammetry

In this technique, the potential is initially held at a predetermined potential, to allow the system to equilibrate. The potential is then increased in a stepwise manner with time. Current is recorded before and after each step, and the difference is plotted against the potential. DPV is a more sensitive technique than CV, as the effect of the charging current is minimised.

DPV was utilised in this study to determine the presence of absorbed flavins on the electrode surface.

3.1.6.3 Chronoamperometry

Electroactive biofilms transfer metabolically generated electrons to the surface of the working electrode (See Section 3.1.2), for Extracellular electron transfer (EET). Chronoamperometry holds the potential applied to the working electrode at a predetermined constant that is optimal for biofilm formation (+ 0.2V vs Ag/AgCl). EET generates a measureable current, which is used to generate real time information on biofilm formation and metabolic activity.

AgNP BES was also performed using CA, where the potential of the working electrode was held at a constant potential and current monitored over the course of the experiment, which allowed for real time monitoring of Ag reduction.

3.1.7 Bioelectrochemical Synthesis

Bioelectrochemical systems (BES) have been utilised in the past to produce electrical energy as microbial fuel cells (MFC), however the current generation reported to date is not viable for electrical power production for commercial purposes alone. BES increases the reaction rates of biological synthesis. The increase in reaction rate occurs through the donation of electrons from the electrode to oxidoreductases on the microbial cell surface. BES systems have been used to produce a variety of high value products reported in Table 3.1.

Table 3.1: High value products produced by BES in literature

	Inoculum	Substrate	Electrode Material	Reference
Acetate	Activated sludge	Hydrogen	Carbon felt	Jiang et al., 2013
Hydrogen	<i>S. oneidensis</i>	Lactate	Carbon fiber fabric	Rosenbaum et al., 2010
Ethanol	<i>E. aerogenes</i>	Glycerol	Carbon cloth	Sakai and Yagishita, 2007
Hydrogen peroxide	MFC enriched culture	Hydrogen	Graphite	Rozendal et al., 2009
Methane	Activated sludge	Hydrogen	Carbon felt	Jiang et al., 2013

Although mixed species electroactive biofilms have been used to produce AgNPs prior to this report (Kalathil et al., 2011), the effect of the application of an electrochemical potential has not been examined to date. Mixed inoculum is usually preferred for BES synthesis, as mixed microbial consortia offer higher flexibility than single species in terms of substrate utilization for BES and do not require sterile or clean feed.

3.1.8 Aim of Chapter

Biological synthesis of MNPs suffers from poor synthesis kinetics, due to the low reduction rate of the host organism. The oxidation state of the enzymes of the mtr pathway in *S. oneidensis* biofilm can be influenced by the application of an electrochemical potential (Ross et al. 2011). As the first step in MNP biosynthesis is metal ion reduction, we hypothesize that the application of a mild reducing electrochemical potential may increase the reduction kinetics of the Ag ions and consequently AgNP synthesis, as *Shewanella* sp. biofilms may accept electrons from the electrode surface and then utilise these electrons to reduce Ag⁺ ions. Ag has a relatively low redox potential $\text{Ag}^+ + \text{e}^- = \text{Ag}^0$, $E^0 = 0.7996\text{V}$, compared to Au which has a redox potential of $\text{Au}^{3+} + 3\text{e}^- = \text{Au}^0$, $E^0 = 1.498\text{V}$. Therefore, to avoid electroplating the working electrode Ag was chosen as a model MNP for this research.

3.2 Materials and Methods

All methods were conducted in accordance with standard protocols and materials were of the highest grade possible (See Appendices 2).

3.2.1 Establishment of *Shewanella* Biofilm

A 3 electrode, 10ml working volume electrochemical cell was set up as described in Chapter 2, Section 2.2.1. A *S. oneidensis* biofilm was established as described in Chapter 2, Section 2.1.2.

3.2.2 Electrochemical Analysis of Biofilm

Electrochemical analysis of sterile electrodes and electrodes with biofilm growth as described in Chapter 2, Section 2.2.

3.2.3 Bioelectrochemical Synthesis of Silver Nanoparticles

Silver nanoparticles (AgNPs) were synthesized as described in Chapter 2, Section 2.3.1, and isolated and analysed by U.V. visible spectrophotometry, DLS, TEM, AFM, XPS and XRD as described in Chapter 2, Section 2.4.

3.2.4 Electrode Analysis

Sterile carbon felt (CF) electrode and CF electrode with biofilm after AgNP synthesis were analysed by SEM and EDX as described in Chapter 2, Section 2.5.1

3.3 Results

Electrochemical cell data such as CV are presented in this section as per the IUPAC convention. All references to potential are in reference vs. an Ag/AgCl reference electrode.

3.3.1 Biofilm Establishment

As discussed in Section 3.1.2, electrode material is an important decision in electrochemical cell design. Prior experience in our group has shown that carbon felt (CF) and carbon cloth (CC) show the greatest current generation for *Shewanella loihica* PV4. Prior to inoculation, the electrochemical cells were analysed by CA, CV and DPV (Fig 3.10) to ensure that the connections in the electrochemical cell were secure, the electrochemical cell was anaerobic and there were no chemical impurities present on the working electrode (e.g. HCl from the carbon felt preparation or metal impurities). There is no detectable signal arising from the CV and DPV analysis for the sterile ECs, which indicates that the ECs are well constructed and any signal generated in the course of the experiment is due to the electrochemical activity of the *S. oneidensis* inoculum.

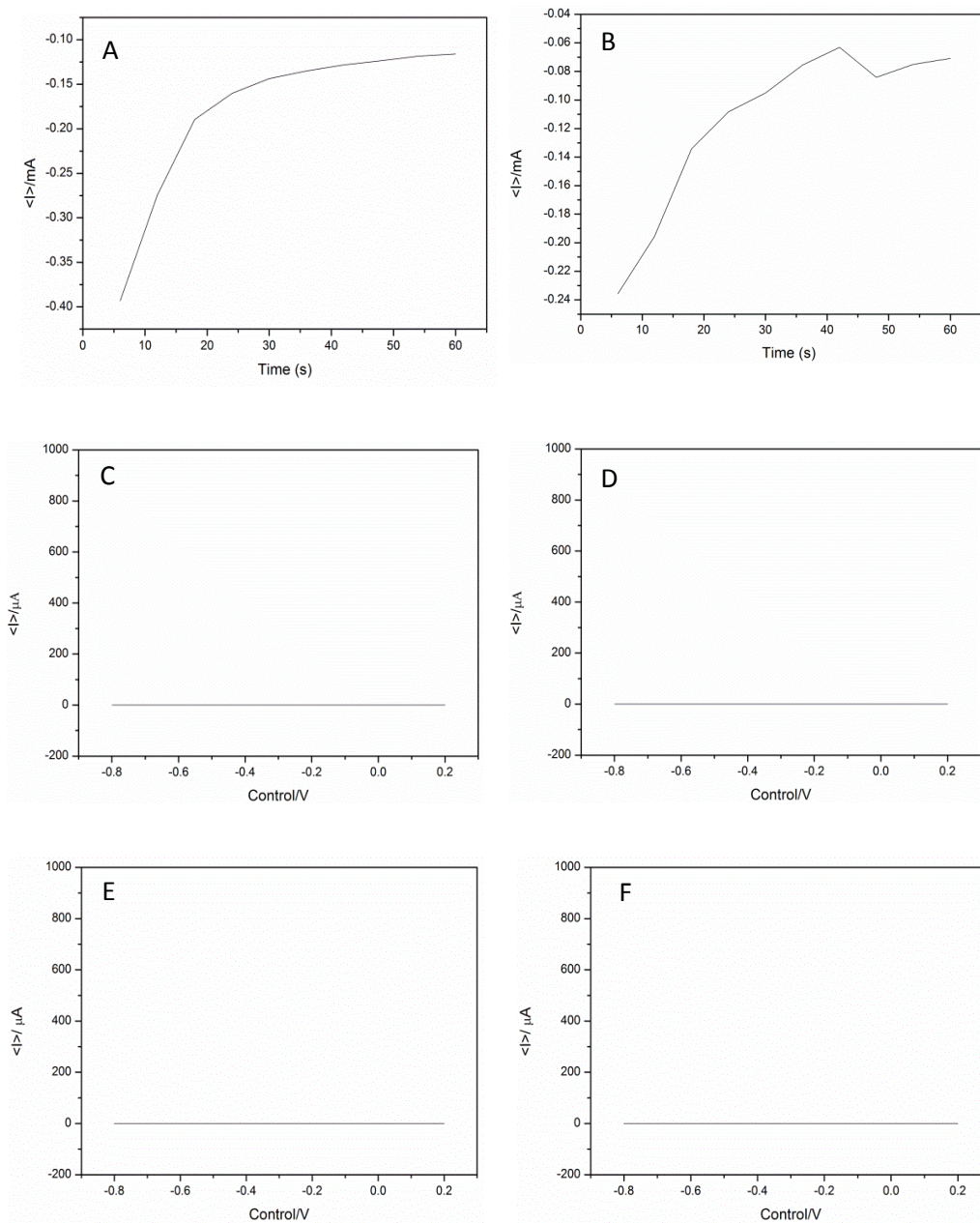


Figure 3.10: Electrochemical analysis of sterile electrochemical cell fitted with (A, C, E) carbon felt and (B, D, F) carbon cloth working electrodes containing M1 growth medium. (A, B) chronoamperometry at -0.8V (C, D) cyclic voltammetry and (E, F) differential pulse voltammetry.

After 22 hours of aerobic incubation in LB media, the OD_{600nm} of the *S. oneidensis* culture was 2.4 ± 0.1 , after which the cells were diluted in M1 media to an OD_{600nm} of 1. 2mls of the standardised culture was used to inoculate 20mls of M1 media and incubated for 24 hours at $30^{\circ}C$ and 150rpm. After 24 hour incubation, the OD_{600nm} of the culture was 1.5 ± 0.05 . CA of the *S. oneidensis* culture with CF working electrode showed that the cells adhered to the surface of the CF immediately upon introduction into the electrochemical cell, while bacterial attachment to the CC electrode appears to be more gradual (Fig. 3.11a). The current output reached a stable value after approximately 10 and 16 hours of incubation for cultures incubated with CF and CC working electrodes respectively. Comparing the anodic and cathodic peaks in the CV analysis of the *S. oneidensis* culture on CF and CC, the biofilm on CF shows a greater anodic current, while there is not a significant difference in the cathodic current.

DPV reveals the presence of microbially produce flavins, which increased over the course of biofilm development (Fig 3.11e and Fig. 3.11f). The flavin peak (~ 0.4 for the CF) is higher than the height of CC.

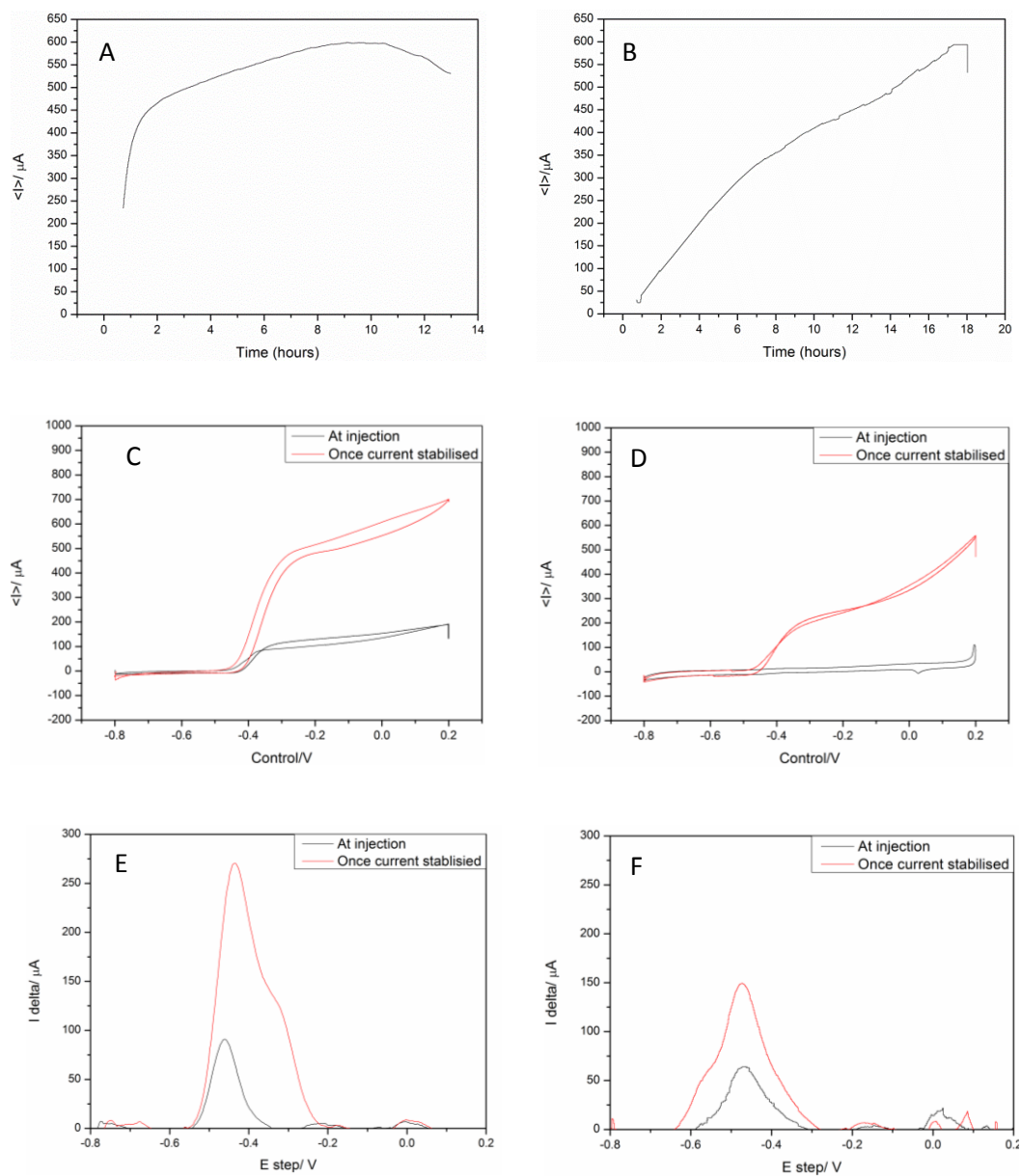


Figure 3.11: Electrochemical analysis of *S. oneidensis* MR1 biofilm established on a (A, C, E) carbon felt or (B, D, F) carbon cloth working electrode. (A, B) chronoamperometry at -0.8V (C, D) cyclic voltammetry and (E, F) differential pulse voltammetry.

Table 3.2: Maximum current density produced by *S. oneidensis* cells attached to each electrode

	Current density $\mu\text{A}\cdot\text{cm}^{-2}$
Carbon Felt	$313 \pm 77 \mu\text{A}\cdot\text{cm}^{-2}$
Carbon Cloth	$343 \pm 65 \mu\text{A}/\text{cm}^{-2}$

3.3.2 Silver Nanoparticle Bioelectrochemical Synthesis

The flavin peaks are reduced after replacement of the media with 100mM HEPES (Fig. 3.12).

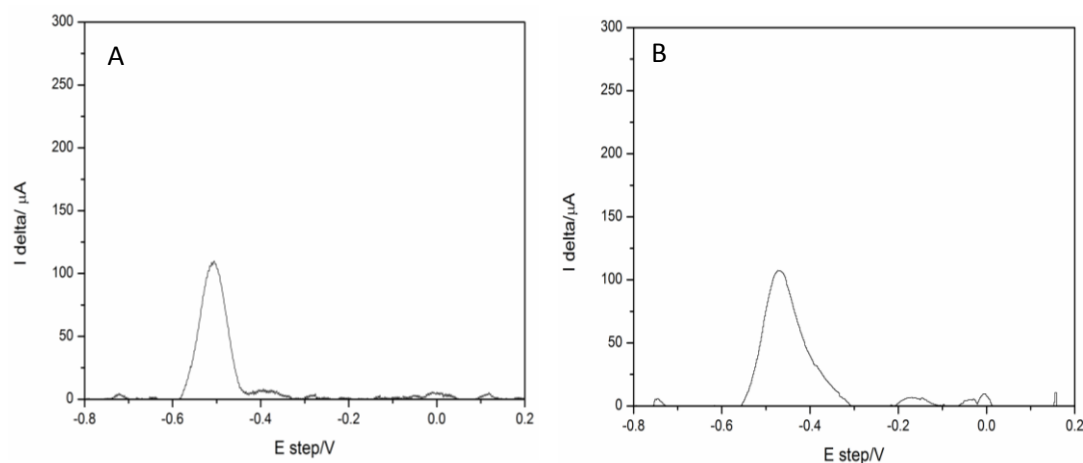


Figure 3.12: DPV of biofilm on (A) carbon felt or (B) carbon cloth after removal of spent media and injection of 100mM HEPES, and prior to 1mM Ag addition

After AgNP formation, the AgNPs were isolated from planktonic cells by centrifugation at 5,000 rpm for 10 minutes, and soluble flavins by centrifugation at 13,500rpm for 30 minutes as both the *mtrC* and *omcA* absorb light at 408nm (Shi et al., 2006) and flavins at (450nm), which is in the range of the SPR of AgNPs. The AgNP pellet was suspended in DI water and analysed by U.V. visible spectrophotometry (Fig. 3.13). The visible spectra of each potential showed a peak at ~414nm and ~525nm for CF and at ~ 525nm and ~ 600nm for CC. The peak at ~414nm corresponds to well dispersed AgNPs, while at ~525nm and ~600nm corresponds to AgNP aggregates, due to the overlapping of surface plasmon, which has been described previously for AuNPs (Fernández-Blanco et al., 2012) and

AgNPs (Tseng et al., 2010). In order to examine if the applied potential may reduce Ag ions in solution, abiotic experiments were performed. Fig 3.13d, shows that the applied potential does not produce AgNPs. As *S. oneidensis* attached to CF produced a greater abundance of well dispersed AgNP than CC, therefore CF was chosen as the electrode material for future experiments.

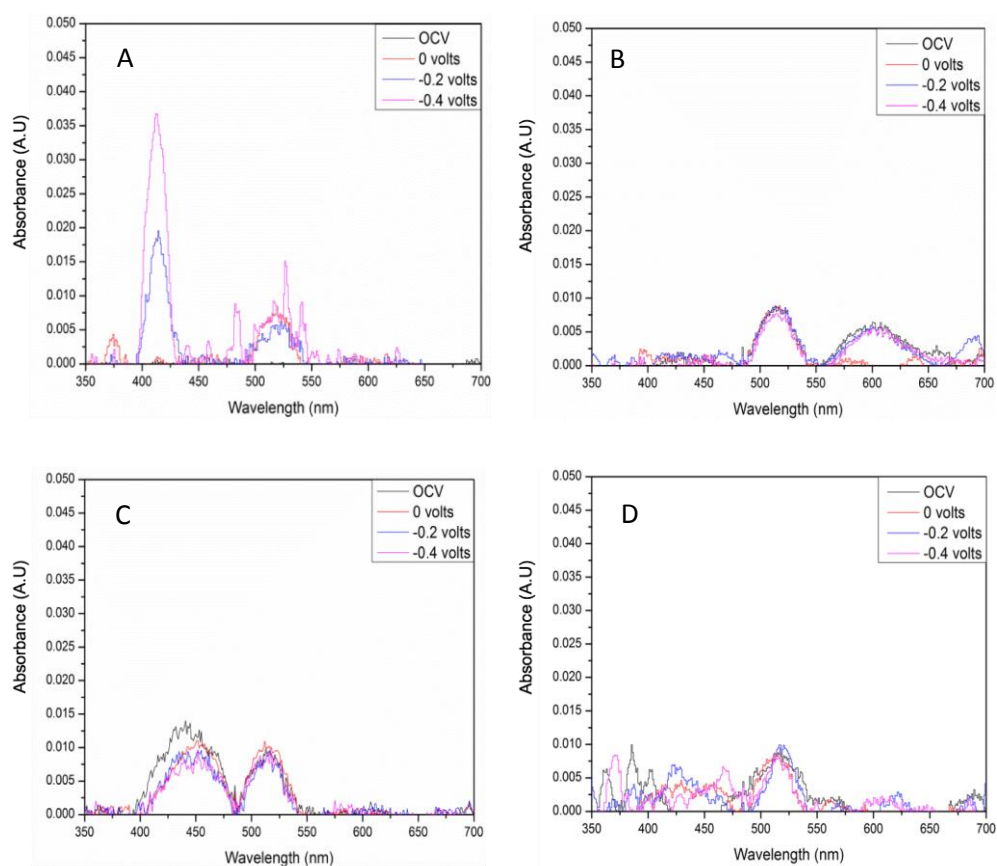


Figure 3.13: UV-visible spectra of the AgNP pellet produced by a *S. oneidensis* biofilm grown on a (a) CF or (B) CC working electrode, which was exposed to 1mM AgNO₃ and poised at 0, -0.2 or -0.4 volts for 100 minutes with 150 rpm stirring under anaerobic conditions. (c) CF and (d) CC abiotic control experiments,

The spectra for the AgNPs produced by the control appear to not be affected by applied potential. Therefore it was hypothesized that the HEPES buffer may be responsible for these peaks. To test this, 100mM HEPES buffer was incubated at 30°C under anaerobic conditions without the electrode under sterile conditions. Fig.

3.14 demonstrates that HEPEs buffer produces two small peaks ~525nm and ~600nm, which can be attributed to experimental noise.

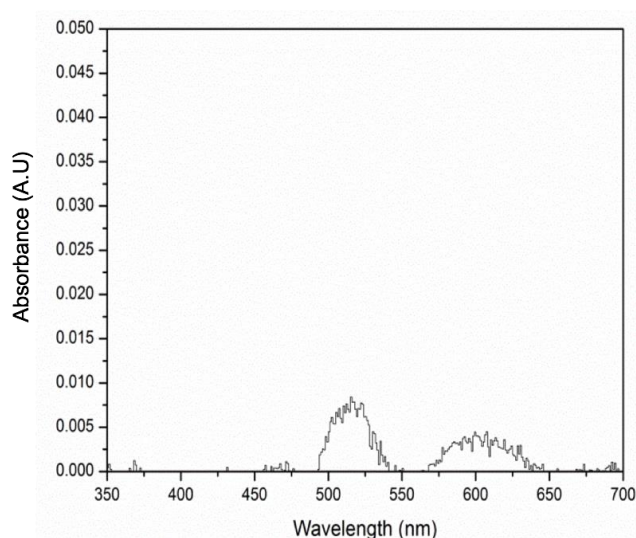


Figure 3.14: UV-visible spectra of 100mM HEPEs buffer incubated at 30°C with 1mM AgNO₃ for 100 minutes under aerobic conditions.

Further we were interested in AgNP bioelectrochemical synthesis formation by planktonic cells, therefore we injected 2 OD_{600nm} culture into sterile ECs and poised the CF at fixed various potentials for 100 minutes. Fig 3.15 shows that the AgNPs produced by planktonic cells are similar to the abiotic control peaks and is unaffected by applied potential

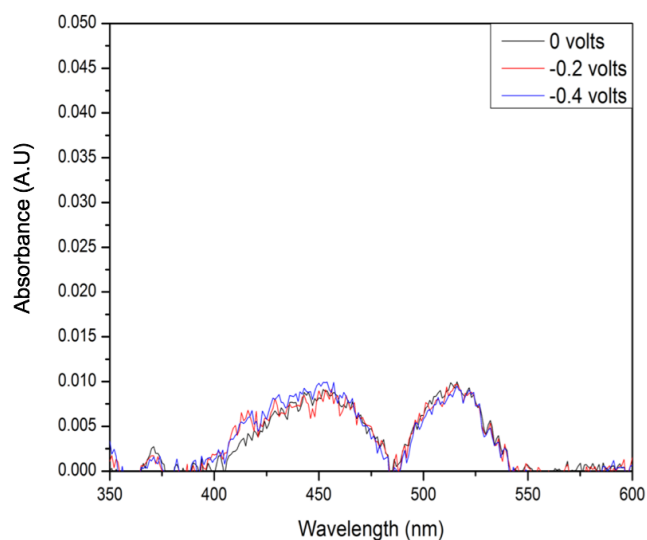


Figure 3.15: UV-visible spectra of the supernatant of a 2 OD600nm planktonic cell culture. Both were incubated with 100mM HEPES buffer, spiked with 1mM AgNO₃, and poised at a fixed potential for 100 minutes with 150 rpm stirring under anaerobic conditions.

Absolute charge transferred can be converted to moles of electrons transferred by Faraday's equation (Eqn. 3.6).

$$e^- = \frac{C}{F} \quad (3.6)$$

Where e^- is the moles of electrons transferred, C is the charge transferred and F is Faraday's constant. This can be then converted to the amount of silver ions reduced by the redox equation in Eqn. 3.7.



Fig. 3.16 shows that as the potential applied decreased, the rate of electron transfer increased. Further when the potential is poised at a high potential (0 - -0.2volts), the amount of electron transfer is low for the biotic experiments, however this value dramatically increases when the potential is poised at -0.4volts. Further the amount of electrons transfer is greater for the abiotic experiments than the biotic. It should also be noted that at -0.4 volts, the amount of electrons transferred is larger than the

amount of Ag ions present, indicating that there are other components in the buffer and in the biofilm that are reduced.

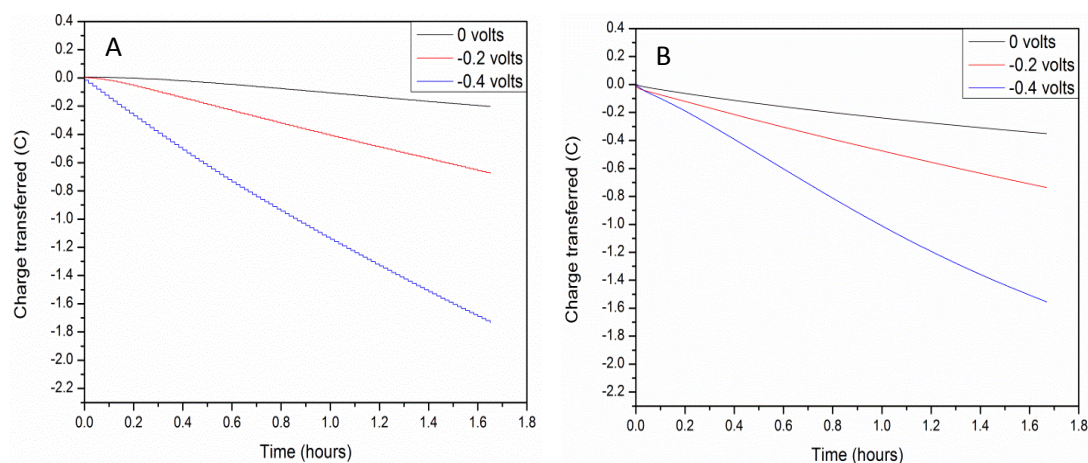


Figure 3.16: Rate of charge transfer from (A) carbon felt or (B) carbon cloth working electrode with 1mM Ag in 100 HEPEs with *S. oneidensis* biofilm.

3.3.3 Silver Nanoparticle Analysis

Table 3.4: Hydrodynamic size of AgNPs synthesized by a 24 hour *S. oneidensis* biofilms grown on carbon felt electrode (n=3).

Potential (V)	Size (nm)	PDI
0	363 ± 16	0.455
-0.2	295 ± 7	0.411
-0.4	290 ± 1	0.408

DLS measurements of the AgNPs isolated from the spent medium, indicates that the AgNPs are large and have a wide poly dispersion index (PDI), indicating a wide size distribution. However the size and PDI decreases as the potential decreases.

AgNPs isolated from the spent medium were then analyzed via atomic force microscopy (AFM) (Fig. 3.17) and transmission electron microscopy (TEM) (Fig. 3.18). AFM images show the AgNPs are small and have a narrow size distribution at 0 volts and -0.4 volts, while the AgNPs were large and had a wide size distribution.

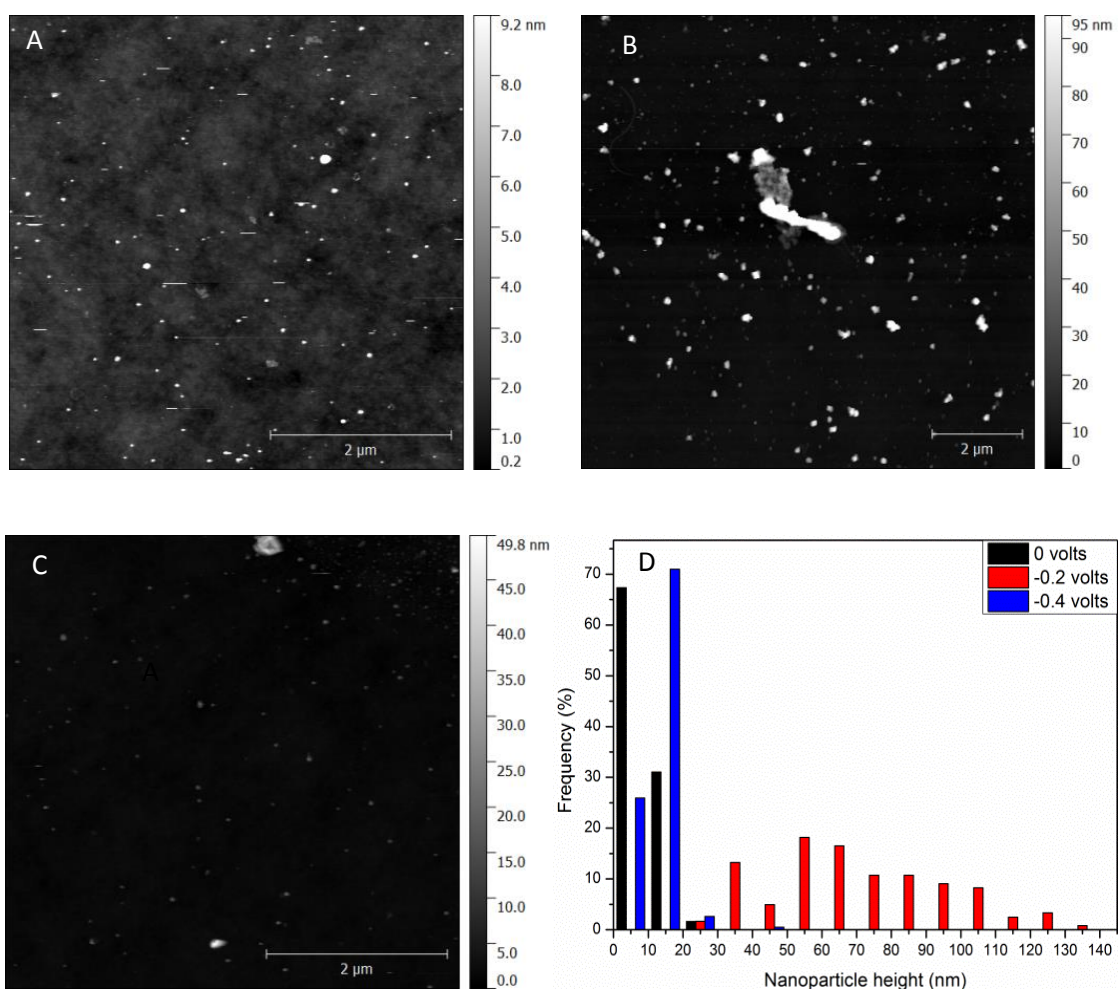


Figure 3.17: Atomic force microscopy images and size distributions of AgNPs in the spent medium from *S. oneidensis* grown on carbon felt electrodes for 24 hours, poised at (A) 0 volts, (B) -0.2 volts or (C) -0.4 volts in a bioelectrochemical reactor at 30 °C under anaerobic conditions and 150 rpm stirring. Nanoparticle distributions plotted on a histogram for *S. oneidensis* (D). Images taken by Alex Summerfield.

The TEM images show that the AgNPs are most spherical, and Image J analysis demonstrates that AgNP size and size distribution increases as potential applied to the biofilm decreases. The histogram of the TEM sizes also shows that the histogram is skewed towards larger AgNPs as size distribution increases.

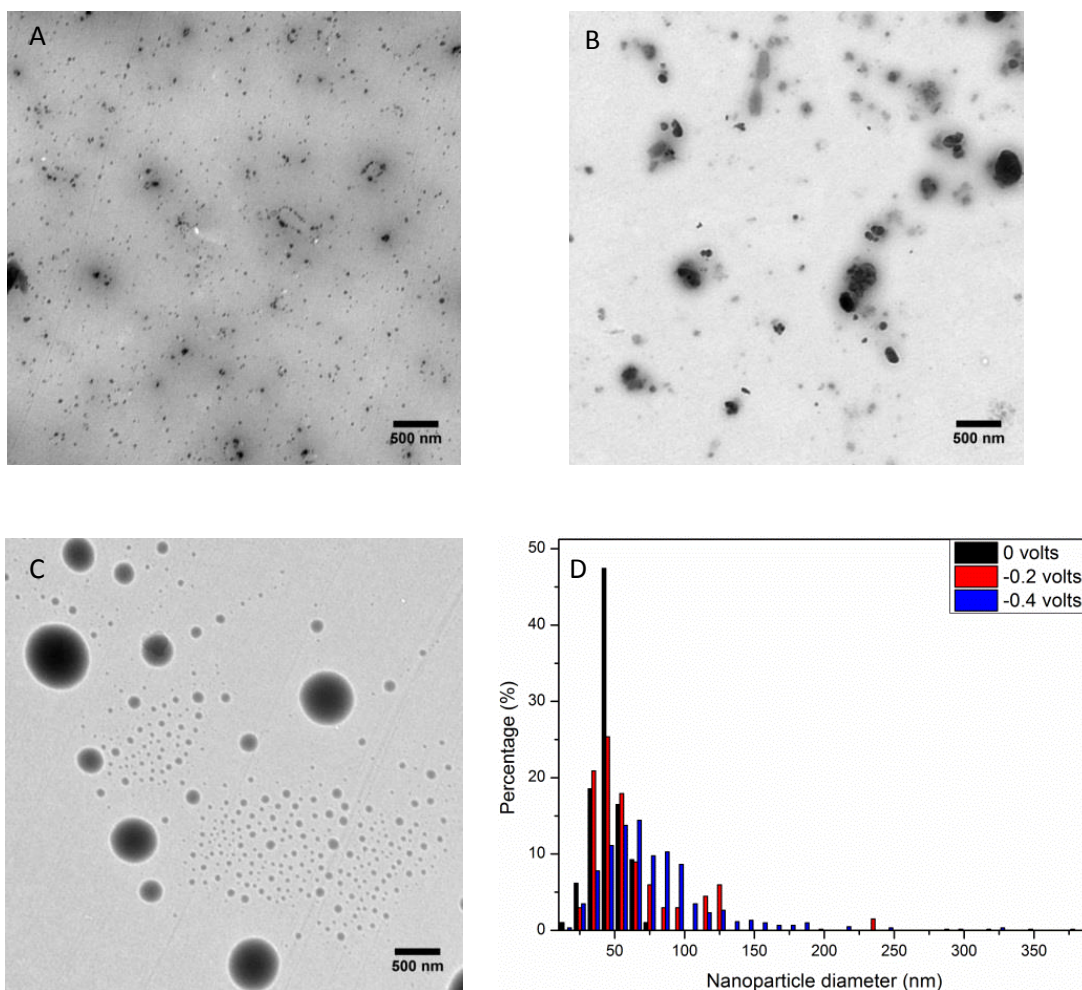


Figure 3.18: Transmission electron images and size distributions of AgNPs in the spent medium from *S. oneidensis* grown on carbon felt electrodes for 24 hours, poised at (a) 0V, (b) -0.2 volts or (c) -0.4 volts in a bioelectrochemical reactor at 30 °C under anaerobic conditions and 150 rpm stirring.

Crystalline structure of the AgNPs was investigated by XRD. XRD analysis (Fig. 3.19) reveals an Ag (111) plane, for all 3 samples. However at -0.2 volts, the XRD reveals Ag (200) and (311) planes. This indicates that the AgNPs synthesized at -0.2 volts possess a fcc structure, in accordance with other reports (Singh and Khanna, 2007). There were also a number of unrelated peaks detected and highlighted in Fig. 3.16. Silica (004) arises from the silica substrate used to mount the AgNP samples, the * labelled peak is due to the adhesive tape and # from the Cu K_{β} and tungsten L_{α} radiations from the X-ray tube.

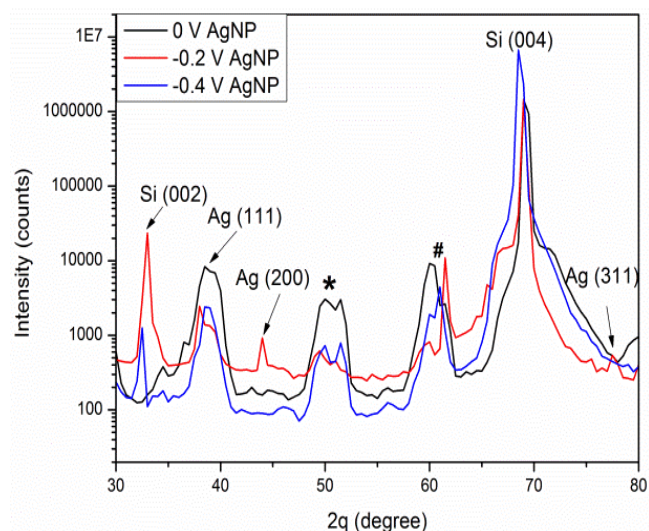


Figure 3.19: XRD analysis of AgNP synthesized by *S. oneidensis* biofilms grown on a carbon felt electrode for 24 hours poised at various fixed potentials for 100 minutes at 30⁰C and 150 rpm. * is due to the adhesive tape and # arises from XRD Cu K_β and tungsten L_α radiations from the X-ray tube. XRD analysis performed by Saikumar Inguva.

Table 3.5: Statistical analysis of the size of the AgNPs synthesized by *S. oneidensis* on carbon felt at each electrochemical potential applied, measured by TEM and AFM (n=3).

	0 volts	-0.2 volts	-0.4 volts
TEM Measured AgNPs (Diameter)			
Mean (nm)	45 ± 1	61 ± 4	78 ± 2
AFM Measured AgNPs (Height)			
Mean (nm)	9 ± 1	69 ± 6	11 ± 1
d spacing (Å)	2.3 ± 1	2.3 ± 1	2.3 ± 1
Crystal size	4 ± 1	4 ± 1	6 ± 1

AgNP mean height (AFM) and diameter (TEM) were measured, and reported in Table 3.5. These measurements do not agree between the different analysis methods. The large DLS suggests a large hydrodynamic size. The lattice spacing (d) and crystallite size was calculated from the Ag (111) plane

The XPS data of the Ag nanoparticles synthesized at different voltages is shown in Fig 3.20, which shows the wide scan of samples synthesized at 0V, -0.2V and -0.4V. In all the samples, the most prominent peaks were corresponding to Ag3d, Na1s, Zn2p, O1s, N1s, Ca2p, C1s and P2p in addition to the S12p from the substrate.

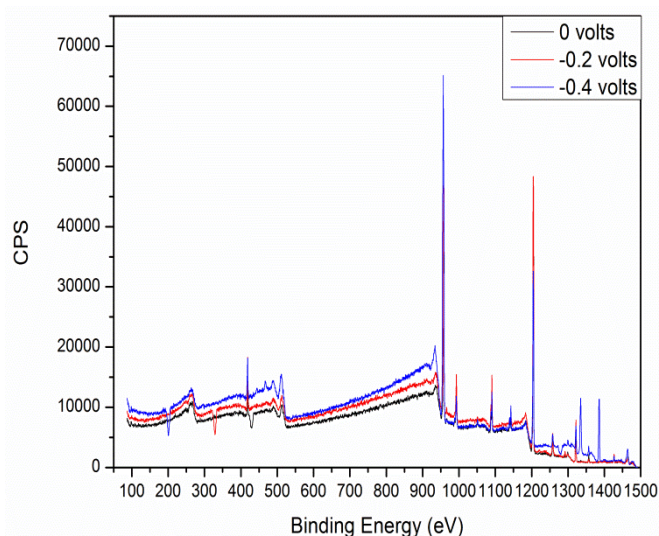


Figure 3.20: Wide scan XPS of AgNPs of *S. oneidensis* biofilms developed on CF electrodes exposed to 1mM Ag and poised a 0, -0.2 and -0.4 volts for 100 minutes.

At 0 volts, the binding energies corresponding to Ag3d_{3/2} and Ag3d_{5/2} were 365eV and 371eV, respectively. The peaks corresponding to -0.4V had the highest intensity, which indicates larger quantities of Ag synthesized at -0.4V. The presence of other elements is in accordance with the reaction condition utilized.

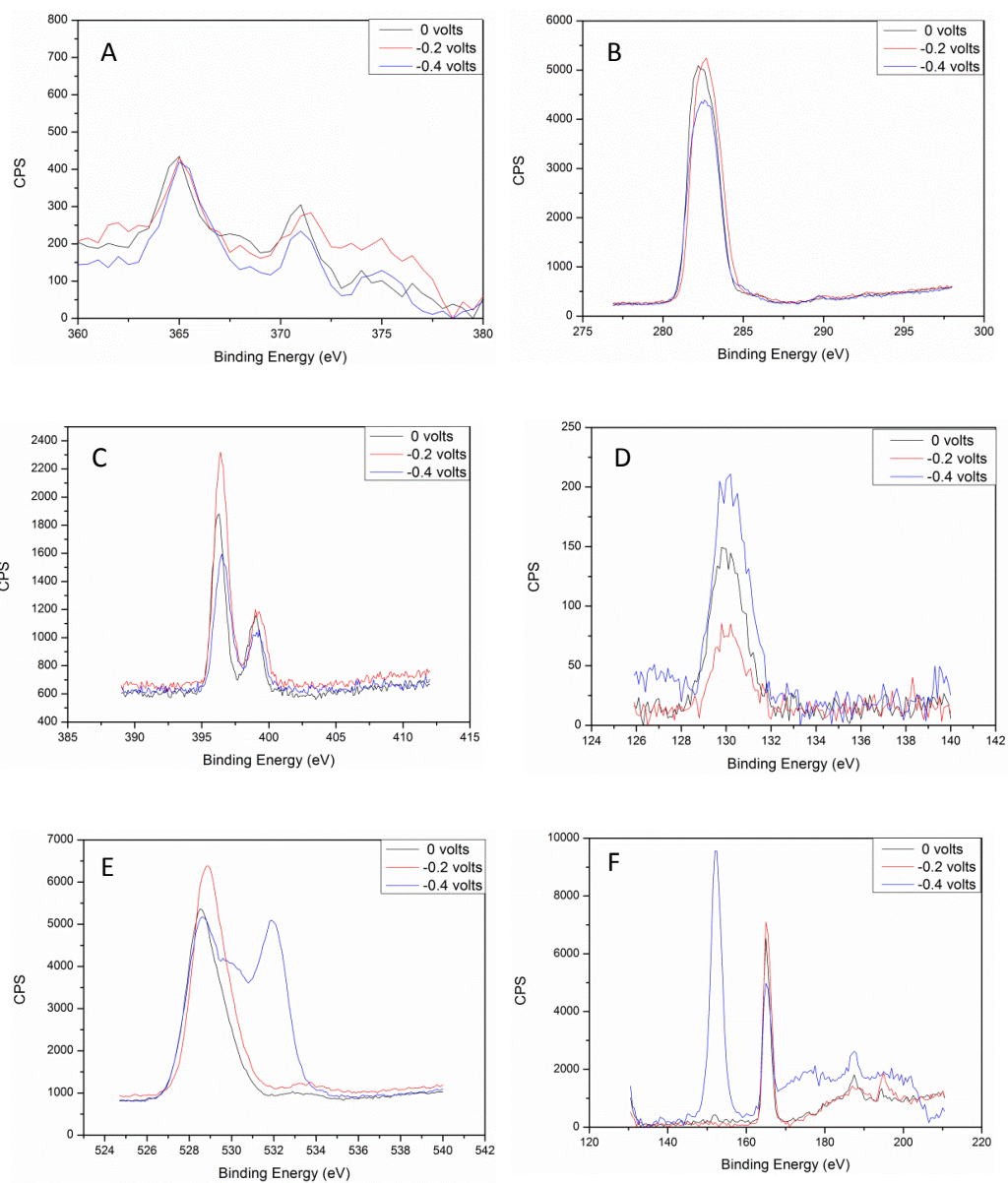


Figure 3.21: High resolution XPS analysis of AgNP synthesized by *S. oneidensis* biofilms grown on a carbon felt electrode for 24 hours poised at a fixed potential for 100 minutes at 30⁰C and 150 rpm. (a: Ag, b: C, c: N, d: P, e: O, f: S). XPS analysis by Emily Smith.

3.3.4 Biofilm Analysis

Metal deposition on the electrode surface was examined by SEM-EDX (Fig. 3.15). SEM images of the biofilm suggest that at OCV and 0 volts, the biofilm is disrupted by the high concentration of Ag^{+1} ion. At -0.2 volts, the rate of Ag reduction decreases the concentration of Ag^{+1} ion to a sub toxic concentration. However at -0.4 volts, the low potential disrupts the biofilm. SEM of the control electrodes show that Ag deposition onto the electrode surface increased as potential applied to the electrode decreased.

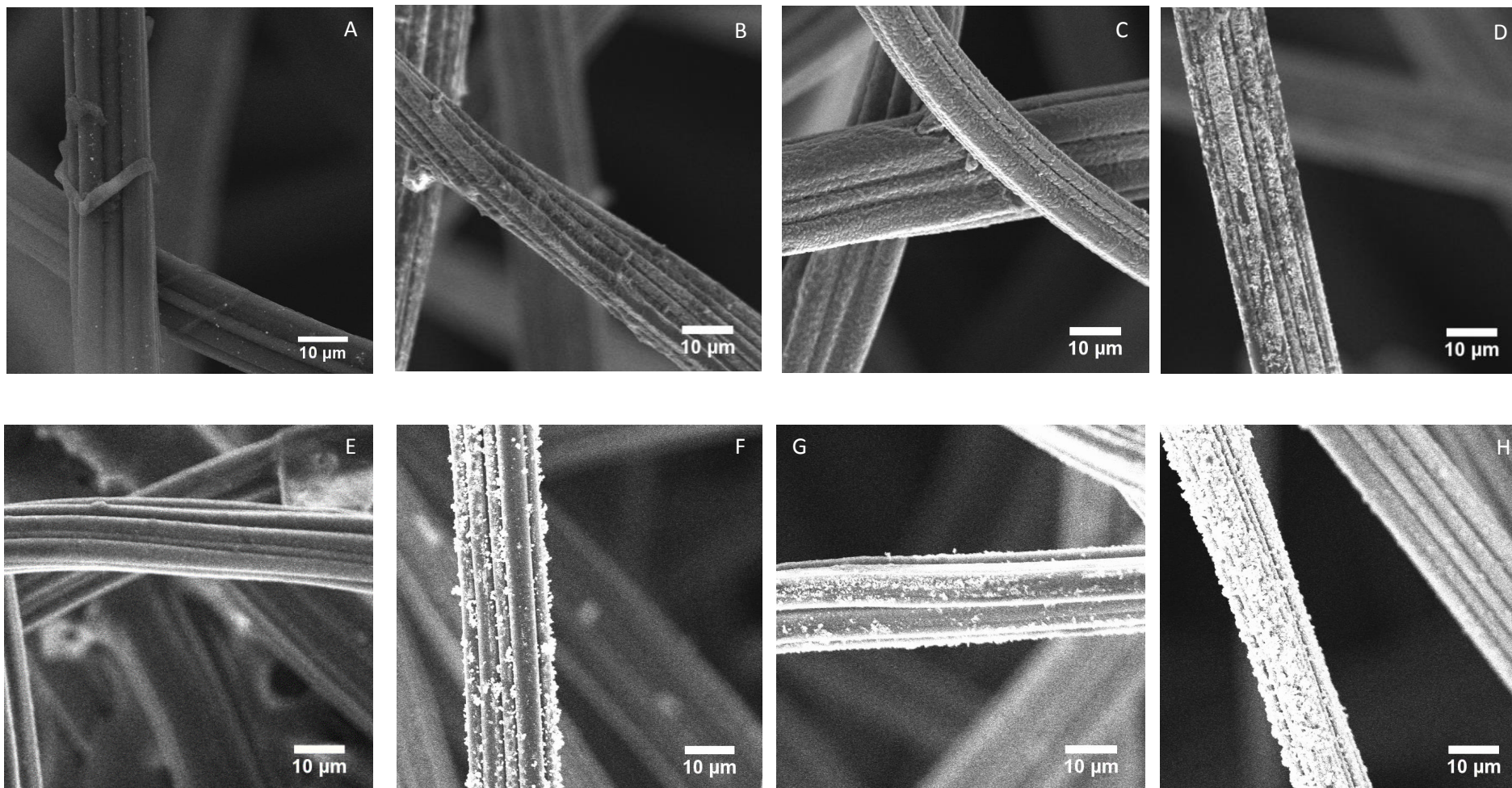


Figure 3.22: SEM images (1k X) of (A-D) a *S. oneidensis* biofilm grown on a carbon felt electrode for 24 hours and (E-H) a sterile carbon felt electrode exposed to 1mM Ag in 100mM HEPES buffer (pH 7) for 100 minutes at 30°C and 150 rpm, poised at (A, E) open circuit voltage, (B, F) 0 volts, (C, G) -0.2 volts or (D, H) -0.4 volts.

EDX was performed to determine Ag deposition on to the electrode (Fig. 3.23a). As carbon felt is not an ideal surface for EDX, these results are only to compare between the various experimental conditions (biotic vs abiotic at various potentials). Interestingly Ag deposition did not significantly increase for the biotic experiments, until the electrode was poised at -0.4 volts. EDX on the abiotic electrodes shows greater Ag deposition than the biotic at the same potential. Biotic experiments were carbon coated before SEM-EDX analysis, which may account for some of the difference between samples. Interestingly there is a correlation between the charge transferred and Ag deposition on the electrode surface (Fig. 3.23). OCV experiments showed $0 \pm 0.0\%$ Ag deposition for the biotic and abiotic control.

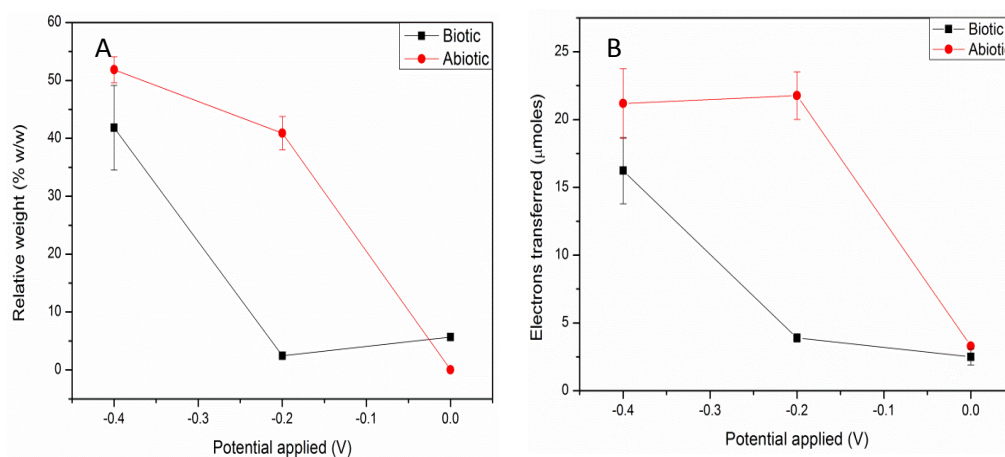


Fig.3.23: (a) Relative weight of Ag deposited (measured by EDX) on CF electrode with biofilm (biotic) and without biofilm (abiotic) and (b) total amount of electrons transferred after CF electrode poised at either 0, -0.2 and -0.4V for 100 minutes.

3.4 Discussion

Anodic current production between the CF and CC electrodes during *S. oneidensis* biofilm development showed no significant difference. However, the CA during biofilm development shows that *S. oneidensis* cells rapidly attach to the CF electrode, while cell attachment to the CC electrode proceeds at a slower and gradual rate. CV analysis of the *S. oneidensis* biofilm developed on CF and CC electrodes shows no significant difference in the cathodic current between the electrode materials. This indicates that the cathodic reaction rate of the biofilm would be similar between the CF and CC working electrodes, which turned out to be the case

as there was no significant difference in the current generated during AgNP synthesis between the CF and CC electrodes.

Similar cathodic current generation between the two electrode materials indicates that there would be no significant difference in the Ag reduction rate and consequently AgNP synthesis by the *S. oneidensis* cells attached to either the CF or CC working electrodes. Comparing the spectra of the AgNPs produced by the *S. oneidensis* biofilm developed on either CF or CC electrodes, CF produced a greater abundance of well dispersed AgNPs than the CC, which produced a low amount of large AgNPs. This suggests the electroactivity of the biofilm, does not affect AgNP synthesis. This is unusual for a BES process, where electroactivity of the microbial community is correlated with BES productivity (Lu et al., 2011). The difference in AgNP synthesis between the electrode materials may be due to the greater amount of biomass present on the CF surface, which has been reported to influence MNP synthesis (Das et al., 2012). Comparing the amount of electrons donated by CF working electrodes, with and without biofilm development, to electron acceptors during CA suggests that the attached cells inhibits charge transfer. In order to determine the role of biomass in the process, 2 OD_{600nm} planktonic *S. oneidensis* cell culture was utilized with sterile CF electrodes. The culture was unable to produce AgNPs, which suggests that attached *S. oneidensis* cells facilitate Ag reduction and structures/biomolecules in the biofilm act as nucleation sites for AgNP formation.

The spectra of the AgNPs show a SPR peak position of 414nm, which is characteristic of well dispersed AgNPs of approximately 40nm (Rogers et al., 2012), however the AgNPs possess a very large hydrodynamic size. Large DLS measurements in previous reports have been assigned to MNP capping by biomolecules such as proteins (Das et al., 2012). The disagreement between the AFM and TEM size may be due to residual biofilm, which would explain the very large hydrodynamic size. TEM shows the AgNP particle size, which agrees with the spectral data. Interestingly the particle size and size distribution increased as the potential applied to the electrode decreased, which was not predicted by DLS. The polydispersion index (PDI) as measured by DLS, suggests the size distribution would decrease with decreasing electrochemical potential. This disagreement may be

due to the lower amount of AgNP aggregation in suspension upon decreasing electrode potential.

The mean size and size distribution of the AgNPs increased upon decreasing the electrochemical potential applied. The histogram of the AgNP distribution shows that as potential decreases, larger AgNP production is favored. The mean AgNP size is much larger than has been reported prior. An overnight planktonic *S. oneidensis* cells synthesized AgNPs that had an average size of 4 ± 1 nm, and a range between 2-11nm (Suresh et al., 2010). However, when $100\mu\text{M}$ Ag was added during *S. oneidensis* planktonic cell growth, TEM images of the culture show Ag deposits of 20-50nm in diameter within the cytoplasm. However, for a lower ($10\mu\text{M}$) nontoxic concentration of Ag, the mean particle size of the biogenic AgNPs produced was 10nm, the majority of which was found on the cell surface. This suggests that intracellular reduction, due to high Ag toxicity, results in large AgNPs located in the cytosol, while the extracellular reduction results in small AgNPs (Wang et al., 2009). The lower abundance of biomass in this study may explain the difference between the AgNP sizes reported. Further as the cells were suspended in DI water during synthesis in Suresh's report, the AgNPs may arise via Ag reduction by intracellular components released by cell lysis. As this project utilized 100mM HEPEs buffer, reduction by intracellular components, released into the spent media due to cell lysis is less likely. The increase in AgNP size upon decreasing the electrochemical potential is not clear.

XRD of the AgNPs shows the crystal size of the AgNPs is smaller than the particle size and is not influenced by electrode potential. This suggests the AgNPs are quasi crystalline in nature. Further XRD of the AgNPs produced at -0.2 volts show Ag (111), Ag (200) planes and a small Ag (311) plane, which has been reported for planktonic *S. oneidensis* cell cultures prior (Suresh et al., 2010). However, the AgNPs produced at 0 and -0.4 volts are missing the Ag (200) and Ag (311) plane. The disappearance of these planes may be related to biofilm disruption. The dominant plane is Ag (111) for AgNPs produced at all potentials. XRD of AgNPs prepared by electrochemical reduced Ag^+ , reveals the presence of Ag (111), Ag (200) and Ag (220) planes but not Ag (311) (Roldán et al., 2013) ; (Singaravelan and Alwar, 2015). However XRD of AgNPs synthesized by a mixed species

electroactive biofilm under non electrogenic conditions reveal Ag (111), Ag (200), Ag (220) and Ag (311) peaks (Kalathil et al, 2011). The presence of these planes have been reported for AgNP biosynthesis by *Brevibacterium casei* viable cells (Kalishwaralal et al., 2010) , dried crushed *Cinnamomum camphora* tree leaf biomass (Huang et al., 2007) , nitrate reductase purified from *Fusarium oxysporum* (Kumar et al., 2007) and *Rhizopus stolonifer* cell free filtrate (Binupriya et al., 2010) The absence of the Ag (311) peak may be unique to electrochemical reduction method, and may indicate direct electrochemical reduction, while the appearance may indicate biofilm mediated reduction.

XPS shows the capping agents are not significantly affected by applied potential. The Ag3d3/2 and Ag3d5/2 peaks corresponding to -0.4V had the highest intensity, which indicates larger quantities of Ag synthesized at -0.4V. At a voltage of -0.4V, two peaks are observed for the O1s spectrum, which arises from the strong oxidation of the silver, yielding the Ag₂O phase of a cuprite structure. This may indicate poor AgNP capping at this potential.

EDX analysis of the biotic and abiotic experiments shows lower Ag deposition on electrodes with attached cells than sterile electrodes, due to the lower charge transfer. At -0.4 volts, the biofilm is disrupted, due to the low potential applied to the electrode, which was accompanied by a significant increase in electron transfer and Ag deposition, possibly due to an increase in the electrochemically active surface area. Examining Fig. 3.11a suggests that biofilm disruption may occur gradually over the course of the experiment, as a sudden disruption of the biofilm may result in a sudden decrease in the slope of the graph.

3.5 Conclusions

We accomplished our aim to increase the synthesis rate of AgNPs by *S. oneidensis* biofilms by the application of a mild electrochemical potential.

Electrode material was an important factor in AgNP BES, as CF electrodes due to their greater surface area resulted in higher AgNP BES than the CC electrode, possibly due to greater amount of attached biomass. *S. oneidensis* biofilms inhibit

Ag reduction, resulting in an increase in over potential, size and size distribution of the AgNP. Application of a mild electrochemical potential, although lowers the amount of aggregates in the spent media, increases AgNP size and size distribution of the core size. However, the AgNPs produced are semi crystalline, due to the ambient synthesis temperature, and AgNP crystallinity is not affected significantly by electrode potential.

3.6 Future work

This research lays the ground work for future research on more versatile MNP synthesis.

AgNP size and size distribution are quite large. Application of a reductive –oxidative potential cycle has been shown to decrease the size and size distribution of AuNPs produced by electrochemical reduction, as each cycle decreased the AuNPs size and created new AuNP nuclei (Fernandez –Blanco et al, 2013). Utilisation of reductive –oxidative potential cycles may decrease AgNP size; however, the capping ligands may prevent AgNP oxidation.

AgNP activity should be examined to determine if the MNPs produced could be utilised in commercial or industrial settings. Potential activities of the AgNPs that should be studied are their anti-microbial activity, catalytic activity and toxicity.

Chapter 4: Fungal Protein Extraction of Gold Nanoparticles

Fungi are underexplored in MNP biosynthesis. Cell surface proteins of *Rhizopus oryzae* produced small AuNPs (~15nm), a purified cell surface protein extract was therefore hypothesized would produce small AuNPs with a narrow size distribution. However different protein extraction methods affect protein stability. The aim of this Chapter is to examine the effect of DTT, SDS and Triton X-100 on protein extraction on the synthesis, size, shape and antimicrobial activity of the AuNPs produced.

4.1 Introduction

4.1.1 Bacteria vs Fungi

AuNP biosynthesis is well characterised in bacteria, however less than 30 fungi species have been investigated to date for AuNP biosynthesis. In general, the biology of fungi is not as well studied compared to bacteria, as their structure complicates the microscopic and mechanistic studies required for MNP characterisation. Under laboratory conditions, fungi grow to a similar biomass density than bacteria. A *Rhizopus oryzae* culture using glucose as a carbon/energy source achieved a biomass yield of $0.55\text{g}\cdot\text{g}^{-1}$, compared to $0.31\text{g}\cdot\text{g}^{-1}$ for an *Escherichia coli* culture under the same conditions (Xu et al., 1999). However fungi have many advantages over bacteria for MNP biosynthesis, such as greater secretion of proteins with diverse functions (Girard et al., 2013). Table 4.1 lists the various pros and cons of the conventional, bacterial and fungal synthesis methods. Fungi have been reported to have a greater metal biosorption ability than bacteria, for example *Aspergillus* sp. absorbed 92% Cr^{-2} and 90% Ni^{+2} while *Micrococcus* sp. absorbed 90% Cr^{-2} and 55% Ni^{+2} at their optimal pH (Congeevaram et al., 2007).

Table 4.1: Pros and cons of physicochemical, bacterial and fungal methods of MNP synthesis (Kitching et al., 2014)

Method	Pros	Cons
Top-down synthesis	Highly controlled particle size distribution and shape	Extreme conditions, High tech facilities, High cost.
Bottom-Up synthesis	Cost-effective. Highly controlled particle size distribution and shape.	Potentially hazardous capping ligands and residual toxins add to environmental toxicity.
Bacteria	Cost-effective and environmentally safe. Biological capping agents for MNP stabilisation	Large nanoparticles with broad particle size distribution. It is not possible to obtain pure nanoparticles without any organic components.
Fungi	Cost-effective and environmentally safe. High concentration of extracellular redox enzymes and capping agents for MNPs stabilization. Smaller size than bacterial-synthesized MNPs. Easy scale up.	Broad particle size distribution, low repeatability. It is not possible to obtain pure nanoparticles without any organic components.

Due to their high secretion of extracellular proteins and small MNP size produced and ease of scale up, biosynthesis by fungi merits further study.

4.1.2 *Rhizopus oryzae*

The fungus chosen for this study was *Rhizopus oryzae*, a filamentous fungus from the family *Zygomycetes*. *R. oryzae* is ubiquitous in nature and often found on decaying organic material and has a large substrate utilisation capacity and can grow on glycerol, ethanol, lactic acid, glucose, mannose, fructose, xylose, cellobiose, fatty acids and oils. *R. oryzae* has been reported to produce ethanol, lactic acid and

fumaric acid, and is often used in Asia for food fermentation and to produce alcoholic beverages such as ragi or tempeh. Although generally regarded as safe, it is known as an opportunistic human pathogen for patients with already weakened immune systems (Meussen et al., 2012).

As shown in Fig. 4.1, at low Au^{3+} concentrations, Au^{3+} ions are reduced by cell surface proteins, however at higher Au^{3+} concentrations ($>250\mu\text{M}$), the Au^{3+} ions diffuse through the cell membrane and are reduced in the cytosol. Further at $250\mu\text{M}$ Au^{3+} , protein expression was suppressed, due to the toxic effect of the high Au^{3+} concentration. Further the authors observed an intermediary Au^+ formation, possibly by methylation (Das et al., 2012).

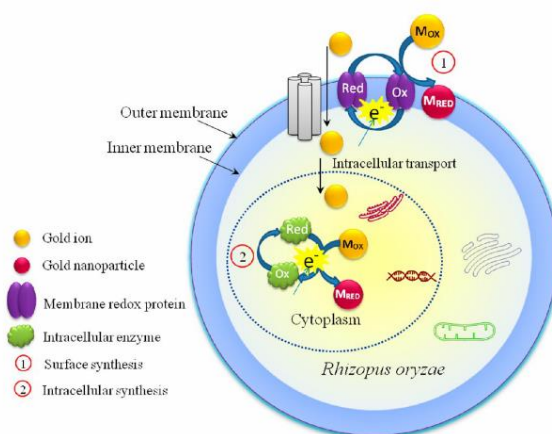


Fig. 4.1: Mechanisms of Au reduction by *R. oryzae* (Das et al., 2012)

Further partially purified protein secretome showed that the ratio between the protein and Au^{3+} ions present in the solution affects AuNP size, as solutions with a higher proportion of Au^{3+} resulted in a larger mean AuNP size, while a higher proportion of protein resulted in a small mean AuNP size (S. Das et al., 2012).

4.1.3 Protein Extraction

The 3 dimensional structure of a protein influences its function, and is affected by pH, temperature, ionic strength, presence of denaturing agents and solvent. The detergent used for protein extraction may affect protein confirmation, for example SDS linearizes proteins into peptide chains with a net negative charge, while DTT and β mercaptoethanol reduces disulphide bonds which reduces protein stability.

The efficiency of protein extraction is dependent on detergent, temperature, ratio of biomass to extraction buffer. Raising the extraction temperature from 4°C-37°C increased the extraction efficiency of cell surface proteins from *Saccharomyces cerevisiae* cells from 27 µg.g⁻¹ to 118 µg.g⁻¹ after 30 minutes with β mercaptoethanol extraction buffer. Further they show that 0.1% w/v SDS has greater protein extraction efficiency than β mercaptoethanol, as SDS at 30°C extracted 5,500 µg.g⁻¹, while β mercaptoethanol at 30°C extracted 118 µg.g⁻¹.

4.1.4 Aims

As reduction of Au³⁺ occurs at the cell surface, using cell surface protein extracts may produce high concentration of AuNPs. However the extraction method may denature the extracted proteins and lead to poor AuNP synthesis ability of the resulting protein extract. In this chapter we compare different extraction buffers in their ability to extract cell surface proteins from *R. oryzae* and the resulting protein extracts for their ability to produce AuNPs.

4.2 Materials and Methods

All methods were conducted in accordance with standard protocols and materials were of the highest grade possible (See Appendices 2).

4.2.1 Fungal Cell Biomass Cultivation and Protein Extraction

R. oryzae was maintained as described in Chapter 2, Section 2.1.1. Fungal biomass was cultivation and cell surface protein extraction was carried out as described in Chapter 2, Section 2.1.3.

4.2.2 Gold Nanoparticle Biosynthesis

AuNP biosynthesis was performed as described in Chapter 2, Section 2.3.2

4.2.3 Gold Nanoparticle Analysis

AuNPs were isolated and analysed by U.V. visible spectrophotometry, DLS, TEM, HR-TEM, XRD, SAED and FTIR as described in Chapter 2, Section 2.4

4.2.4 Antimicrobial Activity

The antimicrobial activity of the AuNPs was determined by analysing their effect on the growth of an *E. coli* culture, as described in Chapter 2, Section 2.7

4.3 Results

4.3.1 Protein Extraction

The weight of blot dried biomass was 90 ± 4 g. The BCA standard curve yielded a linear equation, of which is shown below in Eqn 3.1.

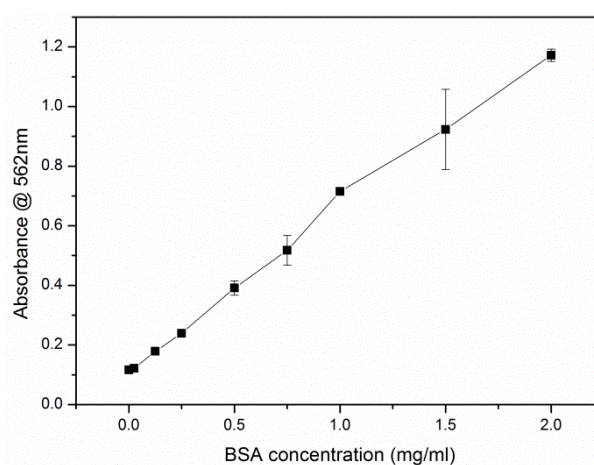


Figure 4.2: Example BCA Standard curve

$$Abs = 0.539(Protein Conc.) + 0.1178 \quad (3.1)$$

Table 4.1: Protein extraction efficiency for various detergents examined

Detergent	Protein Concentration (mg/ml)
2mM DTT	0.32 ± 0.15
0.1% SDS	0.88 ± 0.25
1% Triton X-100	0.67 ± 0.16

The BCA assay shows that the SDS and Triton X-100 detergents have higher protein extraction efficiencies than DTT. Triton X-100, a non-ionic surfactant, also had comparable extraction efficiency to SDS.

4.3.2 Gold Nanoparticle Synthesis

Protein extracts were concentrated using a centrifugal concentrator. 3mg of each protein extract was used in each experiment. After incubation with the Au³⁺ ions we see that the Triton X-100 protein extract produced the greatest amount of AuNPs (Fig. 4.3). SDS produced a small amount of AuNPs with a broad size distribution. The SPR bands are 545nm, 556nm and 540nm for AuNPs produced by DTT, SDS and Triton X-100 protein extracts respectively.

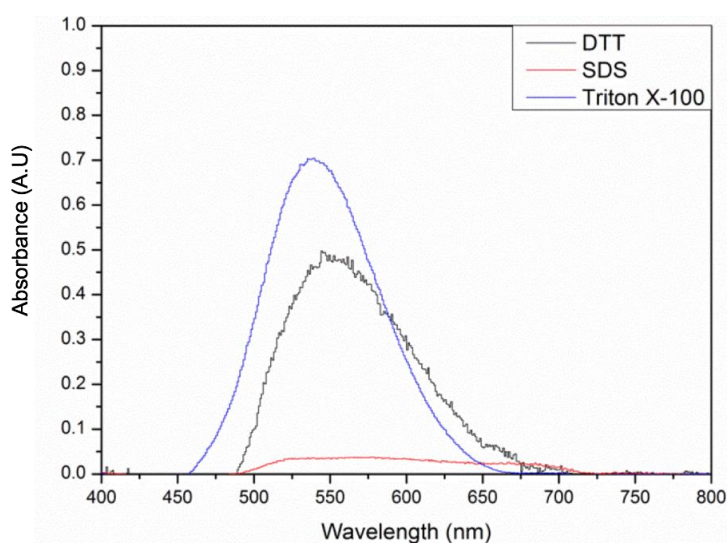


Figure 4.3: UV- Visible spectrophotometry of AuNPs synthesized by *R. oryzae* cell surface extracts, prepared by various detergents.

4.3.4 Gold Nanoparticle Analysis

XRD analysis (Fig. 4.4) of AuNPs produced by all extracts showed Au (111), and Au (222) plane, Triton however showed an additional Au (311) plane. The Au (111) plane was the most dominant plane for AuNPs examined.

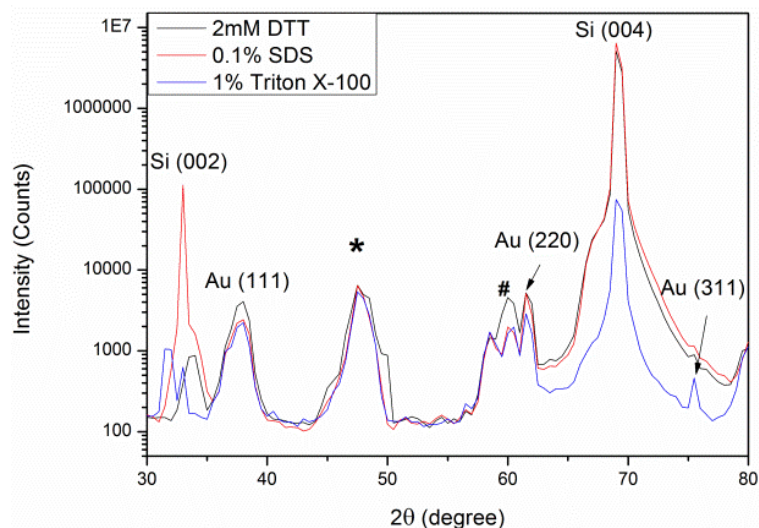


Figure 4.4: XRD of AuNPs synthesized by *R. oryzae* cell surface extracts, prepared by various detergents.

TEM images (Fig 4.5) of the AuNPs show that the AuNPs prepared by DTT and Triton X-100 protein extracts are mostly spherical and approximately the same diameter. While the AuNPs prepared by the SDS protein extract possess a nanoflower morphology. AuNPs diameters were measured using Image J and reported in Table 4.2. HR-TEM image analysis by Image J showed that the d spacing in the AuNPs are also reported in Table 4.2. The SAED of the AuNPs confirm the XRD results, which showed that the AuNPs produced by DTT and SDS extracts possess Au (111) and Au (220) planes while AuNPs produced by Triton X-100 extract possess Au (111), Au (220) and Au (311).

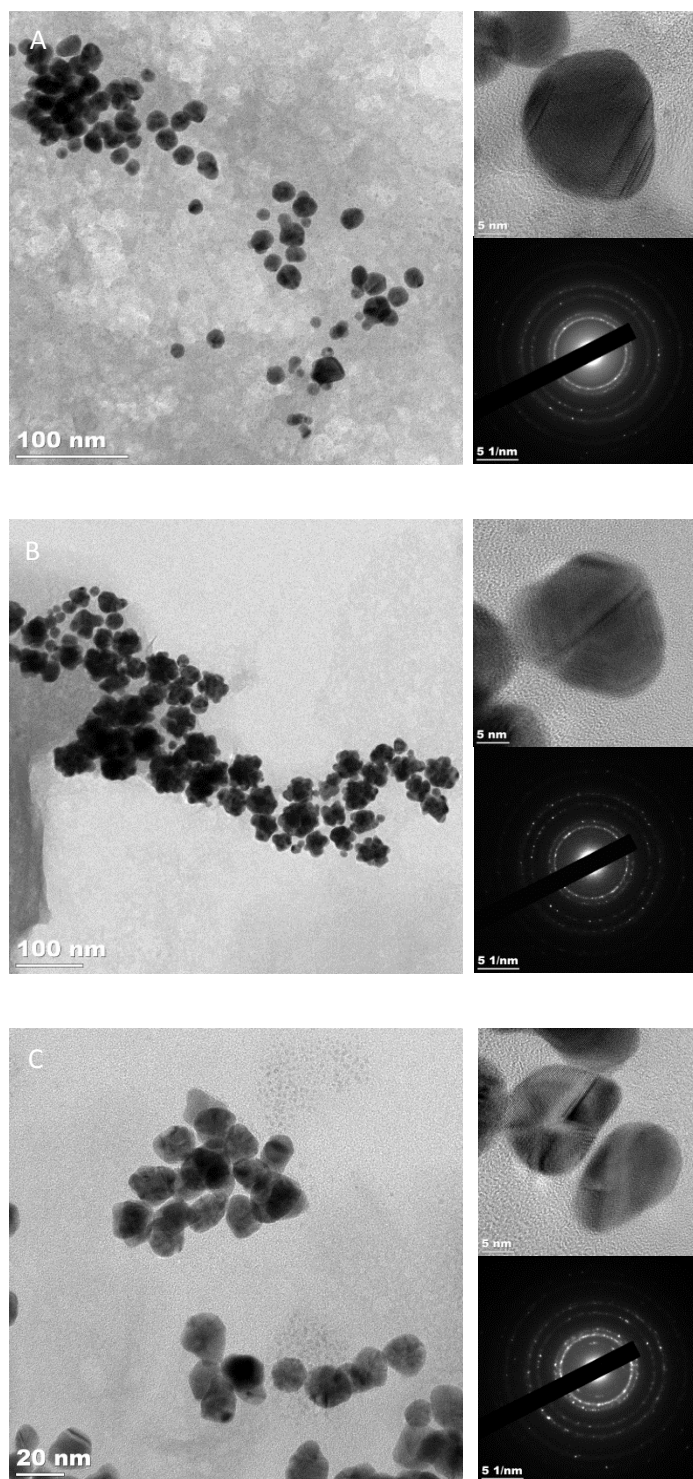


Figure 4.5: TEM, SAED and HR-TEM of AuNPs synthesized by fungal cell surface protein extracted prepared by (A) 2mM DTT, (B) 0.1% w/v SDS and (C) 1% v/v Triton X-100 detergents.

AuNPs produced by SDS protein extract were large and had a wide size distribution, as predicted by their SPR band. AuNPs produced by Triton X-100 and DTT extracts similar in size and size distribution, however the AuNPs prepared by the DTT extract has a significantly wider size distribution (Fig. 4.6).

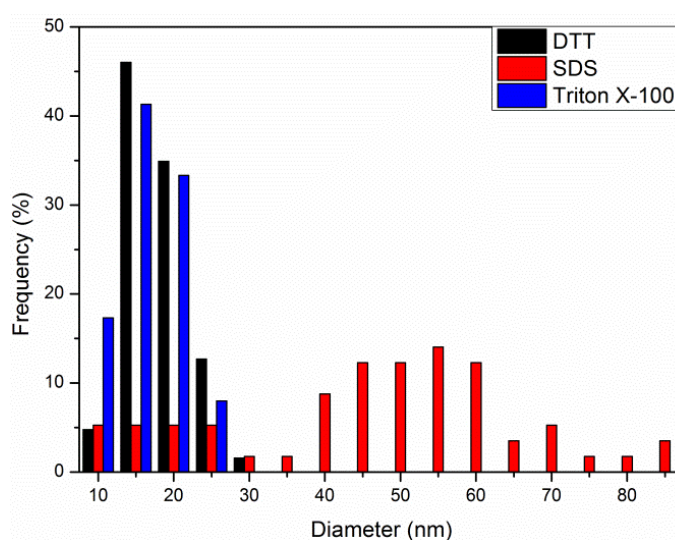


Figure 4.6: Histogram of AuNP sizes produced by 2mM DTT, 0.1% w/v SDS and 1% v/v Triton X-100 extracts.

SDS protein extracts had the largest hydrodynamic and particle size. However all protein extracts had the same d spacing and crystal size.

Table 4.2: Hydrodynamic size (DLS), particle size (TEM and crystal size (XRD) for the AuNPs synthesized by protein extracts prepared by various detergents (n=3).

	Hydrodynamic size (nm)	Particle size (nm)	d spacing (Å)	Crystal size (nm)
2mM DTT	42 ± 4	16 ± 2	2.4	5 ± 1
0.1% SDS	244 ± 35	43 ± 1	2.4	5 ± 1
1% Triton X-100	62 ± 4	19 ± 1	2.4	5 ± 1

4.35 Antimicrobial Activity of the Gold Nanoparticles

To determine the AuNP anti-microbial activity, a growing *E. coli* culture was incubated with the AuNPs. The AuNP dosage was standardised by their SPR peak height, while the 1ml of autoclaved sterilised DI water was added to the culture. The growth curves in Fig. 4.7 shows that the OD_{600nm} of the culture incubated with the AuNPs prepared by Triton X-100 extract was constant around 0.3. While the cultures incubated with AuNPs prepared by DTT and SDS extracts were similar to the control culture until after 12 hours incubation. After 12 hours the OD_{600nm} of the DTT and SDS AuNP treated cultures decreased.

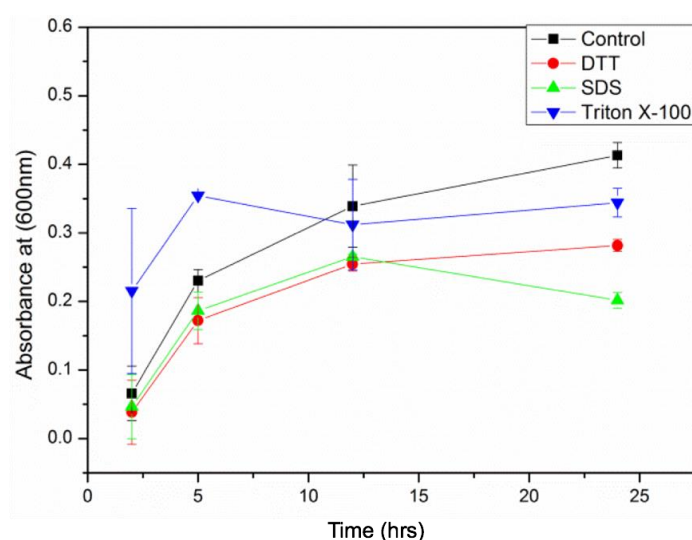


Figure 4.7: Growth curve of *E.coli* in M9 medium with 0.1 OD of AuNPs prepared by various protein extracts.

Table 4.3: Absorbance of *E.coli* incubated with AuNPs produced by the different protein extracts for 24 hours.

AuNP Sample	Absorbance @ 600nm
Control (vehicle)	0.41 ± 0.02
DTT	0.28 ± 0.01
SDS	0.20 ± 0.01
Triton X-100	0.34 ± 0.02

4.4 Discussion

2mM DTT has a poor protein extraction efficiency ($0.32 \pm 0.15 \text{ mg.ml}^{-1}$) compared to 0.1% w/v SDS ($0.88 \pm 0.25 \text{ mg.ml}^{-1}$) and 1% v/v Triton X-100 ($0.67 \pm 0.16 \text{ mg.ml}^{-1}$), possibly due to the lower temperature that the DTT extraction occurs (4°C).

The SPR of the AuNPs show that the average size of the AuNPs would be $>60 \text{ nm}$ for DTT and Triton extract prepared AuNPs and $>80 \text{ nm}$ for the SDS extract prepared AuNPs. However the particle sizes as measured by TEM are much smaller, 50-66% of the size predicted by the SPR peak height. This difference in the SPR predicted size and TEM measured diameter suggests that the AuNPs aggregate in solution. The hydrodynamic size is also larger than the particle size, which is due to the presence of a protein corona which caps the AuNP growth and stabilises the AuNP. Interestingly the SDS extract synthesized AuNPs protein corona is much larger than expected, which indicates the presence of AuNP aggregates.

TEM of the AuNPs produced by the DTT and Triton X-100 protein extracts were small and spherical, however the SDS protein extract produces a small amount of large AuNPs nanoflowers with a wide size distribution, which suggests denatured proteins produce large AuNPs. As an equal amount of protein from each extract was used in the AuNP synthesis, the difference in AuNP abundance and structure arises from the difference in protein structure. Comparing the particle size of the AuNPs generated in this study to AuNPs synthesized by *R. oryzae* secretome at approximately the same protein to Au^{3+} ratio, the secretome produces AuNPs of around $5 \pm 1 \text{ nm}$ which is significantly smaller the AuNPs generated by the cell surface extract, which may be due to residual electron donor (e.g. NADH). Further the protein corona decreases in size as the AuNP size increase, possibly due to the low protein concentration (Das et al., 2012). SDS extract produced large Au nanoflowers which indicates that proteins extracted by 0.1% w/v SDS are poor capping agents as reported for trypsin synthesized AuNPs and is illustrated in Fig. 4.8.

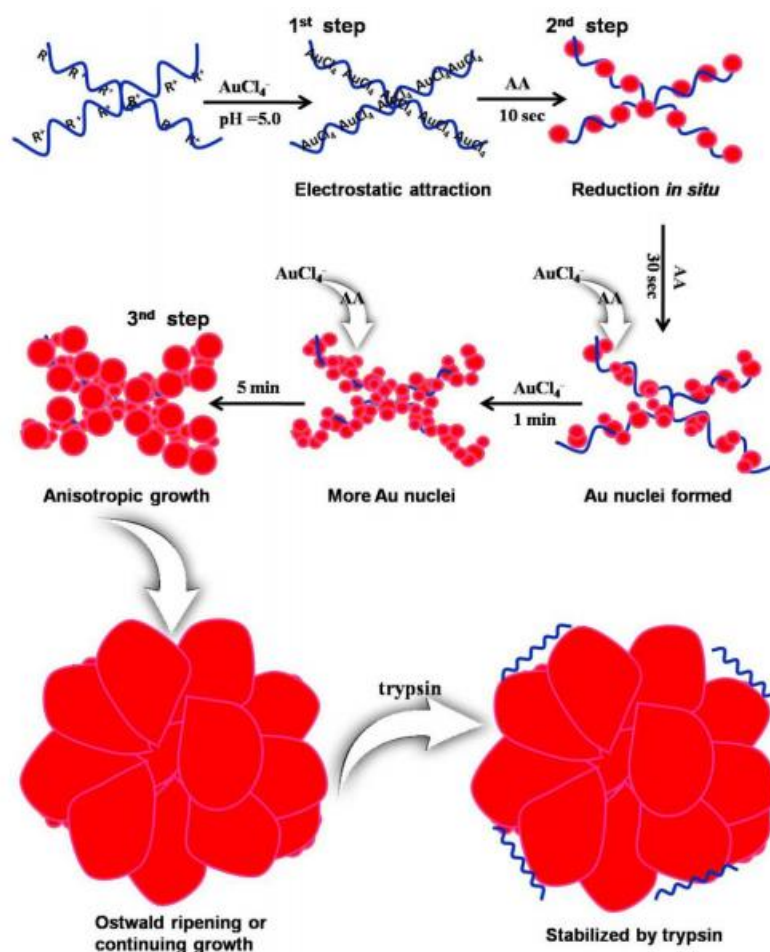


Figure 4.8: Proposed mechanism for gold nanoflower formation by trypsin (Li and Weng, 2010).

XRD shows that the Triton X-100 AuNPs possess the Au (111), Au (220) and Au (311) planes, while the AuNPs synthesized by DTT and SDS extract are missing the Au (311) plane. This indicates that the method of protein extraction influences AuNP crystallisation. The Scherrer ring patterns in SAED of the AuNPs confirm the XRD results. The Scherrer ring pattern associated with the Au (311) plane is poorly visible, possibly due to the low peak in the XRD. The broad XRD peaks are indication of the semi crystalline nature of the AuNPs, due to the ambient temperature of their synthesis. Table 4.3 shows the Au planes detected by XRD analysis of AuNPs produced by various viable fungal cell and protein extracts. The broad XRD bands suggest that the AuNPs are semi crystalline in nature, due to the low temperature of their synthesis.

Table 4.3: XRD analysis of various viable fungal cell and protein extract synthesized AuNPs reported in the literature

Organism	Plane	Reference
Extract		
intracellular protein extract <i>Pycnoprus sanguinasc</i>	Au (111), Au (200), Au(220), Au(311) and Au (222)	Shi et al., 2015
boiled <i>Volvariella volvacea</i> extract	Au (111), Au(200) and Au (220)	Philip, 2009
blended Pear extract	Au (111) and a small Au (200)	Ghodake et al., 2010
Sectrome of <i>Penicillium</i> sp. 1-208	Au (111), Au (200), Au(220), Au(311)	Du et al., 2010
Viable Whole Cells		
<i>Phanerochaete Chrysosporium</i>	Au (111), Au (200), Au(220), Au(311)	Sanghi et al., 2011
Metal tolerant fungi isolates	Au (111), Au (200), Au(220), Au(311)	Gupta et al., 2011
<i>Epicoccum nigrum</i>	Au (111), Au (200), Au(220), Au(311)	Sheikhloo et al., 2011
<i>Hormoconis resiniae</i>	Au (101), Au (200) and Au (220)	Mishra et al., 2010

AuNP dosage was standardised by the SPR peak height, therefore any difference in antimicrobial activity by the AuNPs is due to the physicochemical properties of the AuNPs and not the AuNP concentration. The AuNPs produced by DTT and SDS extracts appear to possess anti-microbial activity, as they appear to reduce the *E.coli* growth rate. However the anti-microbial is for DTT and SDS protein extract prepared AuNPs (32% and 49% decrease in absorbance after 24 hours compared to the control respectively). The cultures incubated with AuNPs produced by Triton X-100 extract showed a high optical density after 2 hours, which may be due to cell lysis, as the OD_{600nm} remains constant during the experiment. This suggests that the Au (311) plane may be responsible for cell lysis, however it may be due to the effect of the protein corona. AuNP induced cell lysis of *E.coli* has been reported before by Zhou et al, who observed cell lysis of an *E. coli* culture after 3 hours of incubation with polyallylaminehydrochloride (PAH) capped AuNPs with a mean size of 22nm. They also show that the negatively charged cell surface of *E.coli* attracts positively charged AuNPs, which cross the cell wall barrier and is involved in the breakdown of the cell wall (Zhou et al., 2012).

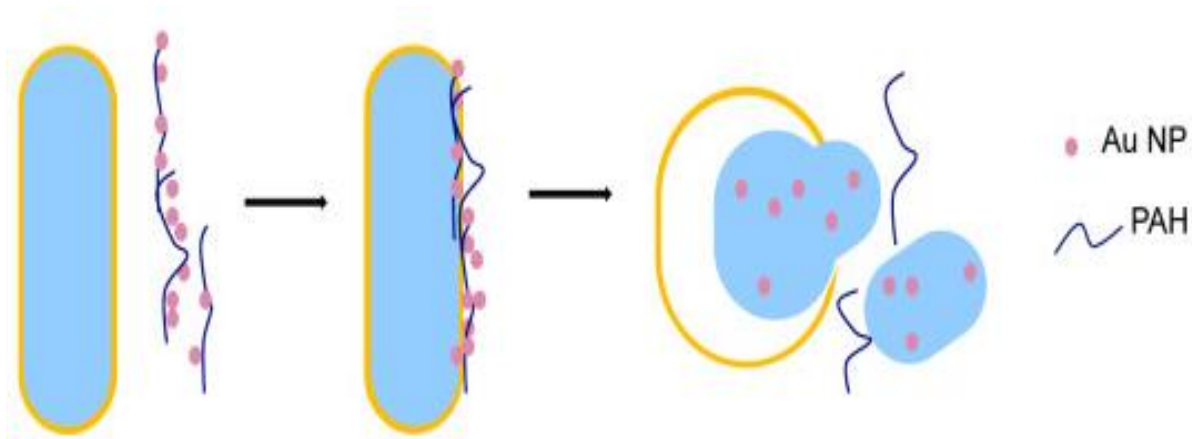


Figure 4.8: Au NPs uptake into bacterial cells followed by lysis (Zhou et al., 2012).

4.5 Conclusions

The optimal extraction buffer for protein extraction is SDS, while the optimal buffer for AuNP synthesis is Triton X-100. Protein structure may affect Au crystallisation, which affects Au size, shape and crystallinity. The antibacterial activity of the AuNPs is also dependent on the AuNP crystallinity and possibly the protein corona.

4.6 Future Study

As stated above, the difference in the AuNPs produced by the cell surface extract and the partially purified secreted protein extract may be due to residual NADH. Future experiments should examine adding in exogenous NADH during AuNP synthesis.

AuNP also possess catalytic activity, the Triton X-100 AuNPs should also be examined for their potential to degrade recalcitrant pollutant such a 4 –nitrophenol.

Chapter 5: Vascular Cell Biosynthesis of Gold Nanoparticle

Biosynthesis of gold nanoparticles (AuNPs) using mammalian vascular endothelial and smooth muscle cells was examined *in vitro*. Cell culture conditions such as buffer selection (PBS) and FBS concentration (1%) were first optimised as well as Au concentration. Following optimisation, the AuNPs produced were semi crystalline in nature and 23 ± 2 nm for endothelial cells and 23 ± 4 nm for smooth muscle cells. The potential synthetic mechanism responsible for AuNP biosynthesis was examined and suggests that the production of reactive oxygen species during oxidative stress reduced the Au³⁺ ions, although there may also be some Au³⁺ reducing activity in the secretome.

5.1 Introduction

5.1.1 Arterial Structure

The vascular system is comprised of a network of various types of blood vessels, which are essential to distribute oxygen and nutrients to tissues and collect and deliver waste products for processing in vertebrates. The structure of a blood vessel is illustrated in Fig. 5.1, which is comprised for 3 main layers, the outermost layer-tunica adventitia, the intermediary layer- tunica media and the innermost layer- tunica intima (Lilly 2014). The tunica intima is a monolayer of endothelial cells, and is important for vascular tone regulation, mediating the inflammatory response and regulating transport of molecules into the media later. The media layer is comprised of vascular smooth muscle cells (VSMC) and elastic fibres. The primary role of the VSMC is to regulate blood pressure, as the endothelial layer in response to stimuli, influences vascular tone and produces vasotransmitters such as nitric oxide (NO), The release of these vasotransmitters cause VSMC relaxation, though the opening of Ca²⁺ channels. The adventitia is comprised of extracellular matrix (ECM), fibroblasts and nerve cells. Recent studies have also suggested that stem cells may also reside in this layer (Tigges et al. 2012; Majesky et al. 2011).

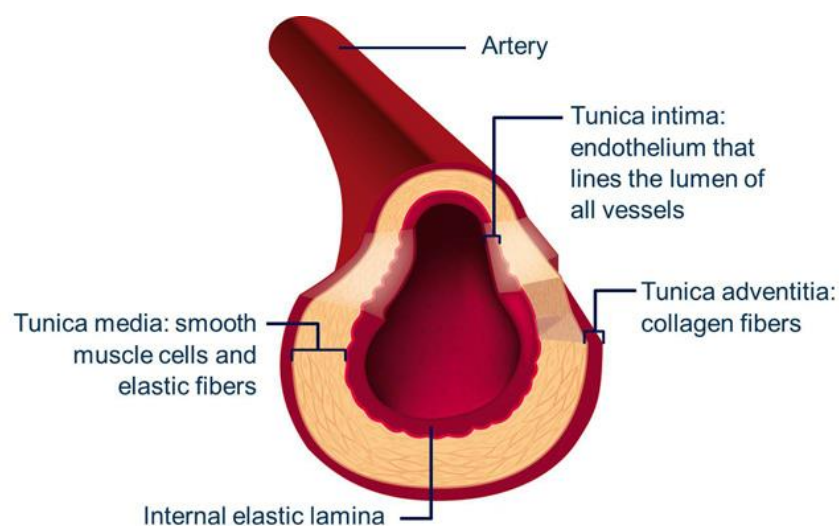


Figure 5.1: Arterial structure (Pah-info.com)

5.1.2 Biosynthesis of AuNPs in Mammalian Cells, *in-vitro* and *in-vivo*

At present mammalian cell biosynthesis of metallic nanoparticles is understudied, most focus on tumor cell biosynthesis and at the time of submission, there nothing in the literature reporting endothelial cell biosynthesis of AuNPs. Deposition of 10 μ l of a 10mM and 100mM HAuCl₄ salt solution on the epithelial cells of a finger produced AuNPs. AuNPs were 14 \pm 11nm for 10mM HAuCl₄ treatment and 49 \pm 21nm for 100mM HAuCl₄ treatment. Although the AuNPs located predominantly in the cytosol of the epithelial cells, they did not account for the fact that human skin is covered in sweat, which contains lysozyme and other salts, which have been shown to produce AuNPs (Larios-Rodriguez et al. 2011) (Wei et al. 2011; Larios-Rodriguez et al. 2011) .

HEK-293 (embryonic cell line) HeLa and SiHa (cervical epithelial cancer cell lines) and SKNSH (neoblastoma cell line) were recently examined on their ability to biosynthesize AuNPs (Anshup et al. 2005). The authors incubated the cell lines at 80% confluency with 1mM HAuCl₄ in 1X PBS. They found that AuNPs were detected in the conditioned media for all cell lines after 55 hours. After 96 hours, the cells were lysed and it was found that the lysate contained more AuNPs than the spent media. AuNPs present in the spent medium was found to be the highest in HEK 293 cell line and lowest in the SKNSH cell line. The observation of higher AuNP abundance in the cell lysate suggests that the cells accumulated Au (III) ions and then AuNPs were formed in the intracellular environment and are exported to the conditioned media. An important point to note is they state that the samples from the spent media were diluted by a

dilution factor of 1:5, however it is not clear if the lysate was also diluted. Further they found that the SPR band of the AuNPs was shifted to a longer wavelength and broadened for the cell lysates, indicating that large, widely dispersed AuNPs were not exocytosed by the cells. TEM analysis of the cells confirms that large AuNPs are located in the cytosol which aggregate, possibly due to the presence of various salts. TEM images also show that AuNPs located in the nucleus are smaller than those found in the cytosol, which suggests that the nucleus has greater reducing ability (Anshup et al. 2005).

The finding that non tumor cells produce more AuNPs than tumor cells is contradictory of another recent study study of AuNP biosynthesis *in vitro* using HepG2 (human hepatocarcinoma) and K562 (leukemia). These cell lines were exposed to 0.0001, 0.001, 0.01, 0.1, 1.0 mM Au for 48 hours, which showed greater AuNP production than the non-tumor control cell line, L02 (human embryo liver cell strand), which did not produce AuNPs. TEM analysis also suggests that AuNPs are synthesized in the cytoplasm and migrate to the nucleus during the experiment. The report also shows that it is possible to synthesize AuNPs *in-vivo* using a BALB/c athymic nude mouse model. AuNP synthesis occurred specifically in tumors. From this the authors propose using the AuNP generation ability of tumor cells as a diagnostic tool to detect cancerous cells (Wang et al. 2013). The disagreement the studies on the ability of non-tumor cell lines may be due the difference in media, as Wang utilized DMEM, while Anshup used 1X PBS in their study, which would indicate that buffer choice influences AuNP biosynthesis.

5.1.3 Oxidative Stress Response by Vascular Cells

Au³⁺ has been reported to induce oxidative stress response genes in microbes such as *Rhizopus oryzae* (Das et al. 2012). Oxidative stress occurs when the balance between reactive oxygen species (ROS) and anti oxidants is disrupted in favor of ROS. Increased production of ROS has been implicated in pathogenesis of cardiovascular diseases such as arteriosclerosis, restenosis, hypertension, diabetic vascular complications and heart failure (Cai 2005). Studies of oxidative stress on vascular cells mainly utilize hydrogen peroxide, which has been reported to induce a variety of effects such as vascular endothelial cell (VEC) and vascular smooth muscle cell (VSMC) proliferation and migration, activation of inflammatory signals such as NF-κB

and formation of peroxynitrite (ONOO^-) (Coyle and Kader 2007). Fig. 5.2 illustrates the general response of VECs to H_2O_2 induced oxidative stress, and shows that low concentrations of H_2O_2 induces cell growth and proliferation, while high H_2O_2 induces apoptosis.

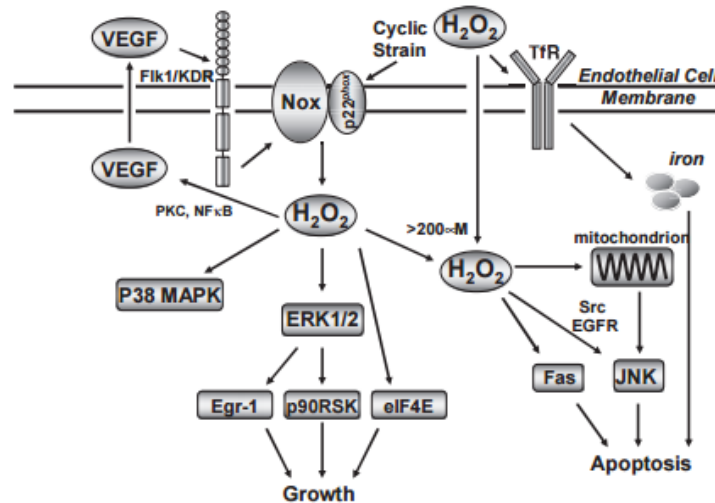


Figure 5.2: General scheme of the response of VECs to oxidative stress imposed by H_2O_2 . H_2O_2 depending on concentration may promote growth or induce apoptosis (Cai 2005).

Porcine aortic endothelial cells (PAEC) exposed to $100\mu\text{M}$ H_2O_2 for 1.5 hours increased the numbers of dihydro-ethidium (DHE) positive stained nuclei increased from $1.6 \pm 0.9\%$ (control) to $50.3 \pm 4.1\%$, indicating O_2^- production. Further when cells were transfected to over express SOD2 and exposed to a Tiron (a non enzymatic superoxide scavenger), DHE fluorescence upon H_2O_2 exposure dropped to $26.4 \pm 3.2\%$ and $16.2 \pm 7.6\%$ respectively. This demonstrates that oxidative stress such as H_2O_2 induces PAEC synthesis of O_2^- as an oxidative stress response. Further eNOS overexpression did not show any change in the DHE staining, while treatment with the NOS inhibitor, N^G -nitro- L-arginine methyl ester (L-NAME) with $100\mu\text{M}$ H_2O_2 , showed a drop in DHE fluorescence from $54.6 \pm 10.3\%$ to $24.9 \pm 8.9\%$, suggesting NOS contribution to H_2O_2 induction of O_2^- synthesis. Apocynin treatment (an inhibitor of NADPH oxidase) with $100\mu\text{M}$ H_2O_2 decreased DHE fluorescence from $54.6 \pm 10.3\%$ to $25.3 \pm 4.7\%$, which indicates that NADPH is an enzymatic source of O_2^- (Coyle and Kader 2007). Tsaryk et al reported that human dermal microvascular endothelial cells (HDMEC) grown on PS and Ti6Al4V substrate and treated with 0.25mM and 0.5mM H_2O_2 for 1 hour showed an increase in DCF fluorescence. Further

HDMEC grown on Ti6Al4V and exposed to 0.5mM H₂O₂ produced higher DCF fluorescence than HDMEC grown on PS, which indicates higher ROS formation and suggests the strength of the oxidative stress response is dependent on the substrate (Tsaryk et al. 2007).

Although Au has not been examined for O₂⁻ production by vascular cells, the heavy metal lead (Pb) has been shown to increase cellular O₂⁻ and H₂O₂ of human coronary artery endothelial cells (HCAEC) and human vascular smooth muscle cells (HVSMC) exposed to 30μM Pb for 30 hours by flow cytometry. Long term exposure (60 days) resulted in cellular O₂⁻ levels dropping back to the basal level, while H₂O₂ remained high. Further western blot analysis shows that the abundance of Cu Zn SOD increased upon Pb exposure for HVSMC and HCAEC (NI et al. 2004) . Interestingly while Ni et al did not detect glutathione peroxidase induction upon Pb exposure. SOD activity for HDMEC on PS increased upon exposure to 0.5mM H₂O₂ for 24 hours, while catalase activity increased for HDMEC on PS upon exposure to 0.25mM H₂O₂, however this decreased at exposure to 0.5mM H₂O₂, SOD or catalase activity did not change for HDMEC grown on Ti6Al4V substrates (TSARYK et al. 2007) .

Glutathione is an important antioxidant in the cell, and is synthesized in a two step process, as shown in. In the first step γ-glutamylcysteine synthetase (γ-GCS) combines glutamate and cysteine to form gamma-glutamyl cysteine (γ-EC). Glutathione synthetase (GS) catalyzes the condensation reaction between the γ-EC and glycine (Gly) to form reduced glutathione (GSH). To maintain a health redox homeostasis, the balance between GSH and oxidized glutathione (GSSG) is strictly maintained. Upon the introduction of oxidative stress by ROS, glutathione peroxidases utilize GSH to neutralize the the ROS, which in turn converts GSH to GSSG) (Liu et al. 2015) .

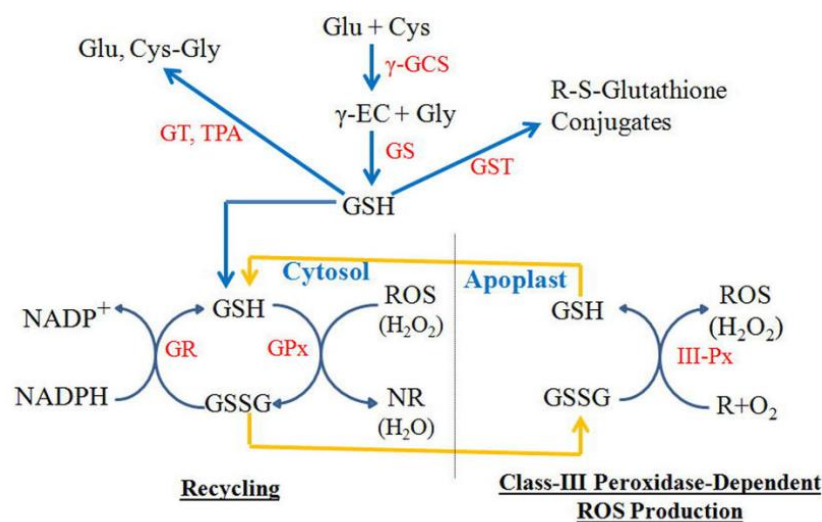


Figure 5.3: Glutathione synthesis and recycling (Liu et al. 2015) .

Interestingly Ni et al western blot analysis of HVSMC and HCAECs exposed to Pb shows that the level of glutathione peroxidase 1 (GPX-1) did not change, while upregulation of the gp91^{phox} subunit of NADPH oxidase occurred in the HCAEC but not HVSMC, as HVSMC does not express gp91^{phox} (NI et al. 2004) . This may imply that the production of the enzyme is not upregulated, but it's activity may increase. Tsaryk et al showed that GPX activity was increased for HDMEC exposed to 0.5mM H₂O₂ PS but not Ti6Al4V substrate, suggesting that GSH response may be context specific (Tsaryk et al. 2007) .

Méthy et al demonstrated using Fe³⁺ + -8-hydroxyquinoline complex (FHQ) induced oxidative stress of rat cerebromicrovascular endothelial cells (RCEC) that for 30 minutes of mild oxidative stress (10:20 μ M FeCl₃/8-HQ) increased manganese superoxide dismutase (MnSOD) mRNA levels up to 4 hours post treatment eventually declining to basal (vehicle control) after 6 hours, while the MnSOD protein abundance increased 6 hours post treatment and dropped below the control at 24 hours, possibly due to proteolysis. Mild oxidative stress increased heme-oxygenase-1 (HO-1) mRNA levels and protein abundance up to 6 hours post treatment, however the HO-1 protein concentration decreased after 24 hours post treatment, but still remained above the control. However for 30 minutes of moderate oxidative stress (20:40 μ M FeCl₃/8-HQ) did not significantly affect MnSOD mRNA levels or protein abundance, it down regulated HO-1 mRNA and protein levels. HO-1 mRNA levels did recover after 6 hours, the abundance of the HO-1 protein however did not increase after 6 hours, in

fact it was not detectable after 24 hours post treatment, possibly inhibition of its transcription factor to bind and proteolysis due to the oxidative environment (Méthy et al. 2004) .

5.1.6 Aims

The aim of this chapter is to optimize the cell culture conditions for AuNP synthesis by bovine vascular cells, and thoroughly characterize the AuNPs produced. Finally we aim to develop a synthetic mechanism for AuNP biosynthesis by vascular cells *in-vitro*.

5.2 Materials and Methods

All methods were conducted in accordance with standard protocols and materials were of the highest grade possible (See Appendices 2).

5.2.1 Cell Culture

All cell culture techniques was performed as described in Chapter 2, such as mammalian cell culture in Section 2.1.5 and subculture in Section 2.1.6.

5.2.2 AuNP Biosynthesis

AuNP biosynthesis experiments were carried out as described in Chapter 2, Section 2.3.3, with the exception of cell culture optimisation optimisation. For the media optimisation, the BAECs were exposed to 0, 0.5, 0.075, 1, 1.5 and 2mM HAuCl₄ in either DMEM, without phenol red or glucose or 1X PBS, supplement with 1% v/v FBS and incubated for 48 hours at 37°C and 5% CO₂.

For FBS optimisation the BAECs and BASMCs were exposed to 0.75mM HAuCl₄ in 1X PBS and supplemented with 0, 0.5, 1, 1.5 and 2% v/v FBS and incubated for 48 hours at 37°C and 5% CO₂.

5.2.3 AuNP Isolation and Analysis

AuNPs were isolated as described and analysed via U.V. visible spectrophotometry, DLS TEM, HR-TEM, SAED, XRD and FTIR as described in Chapter 2, Section 2.4.

5.2.4 Pre-treatments

BAECs and BASMCs were pretreated with 0, 1 and 2mM BSO in full RPMI-1640 media for 16 hours at 37°C and 5% CO₂. AuNP biosynthesis experiments were carried out as described in Chapter 2, Section 2.3.3, isolated and analysed by U.V. spectrophotometry as described in Chapter 2, Section 2.4.1 and Section 2.4.2.

BAECs and BASMCs were also pretreated with 0, 0.01, 0.05, 0.1, 0.5, 1 and 2mM H₂O₂ in full RPMI-1640 media for 24 hours at 37°C and 5% CO₂. AuNP biosynthesis experiments were carried out as described in Chapter 2, Section 2.3.3, isolated and analysed by U.V. spectrophotometry as described in Chapter 2, Section 2.4.1 and Section 2.4.2

5.3 Results:

5.3.1 Optimisation

Cell culture media is necessary for the maintenance of cell lines; however they contain a variety of salts and nutrients which may complex or reduce Au³⁺ ions. DMEM media lacking in glucose (which reduces Au³⁺ ions) and phenol red (which absorbs light at 560nm, which is in the range of AuNPs) was first examined as a synthesis buffer. DMEM was found to be unsuitable as a synthesis buffer (Fig 5.4A and Fig. 5.4C), as sterile DMEM incubated with high Au³⁺ concentrations (1.5mM and 2mM Au) after 48 hours at 5% CO₂ and 37°C produced AuNPs without BAECs. PBS was then utilised as a synthesis buffer, as it is relatively simple in composition. Incubation of Au³⁺ ions with sterile 1X PBS did not result in the abiotic production of AuNPs (Fig. 5.4D). However when 1X PBS containing 0.5mM-2mM Au was incubated with BAECs, AuNPs were produced after 48 hours. This demonstrates that PBS is suitable for synthesis buffer, as it does result in the abiotic production of AuNPs and does not inhibit biosynthesis of AuNPs.

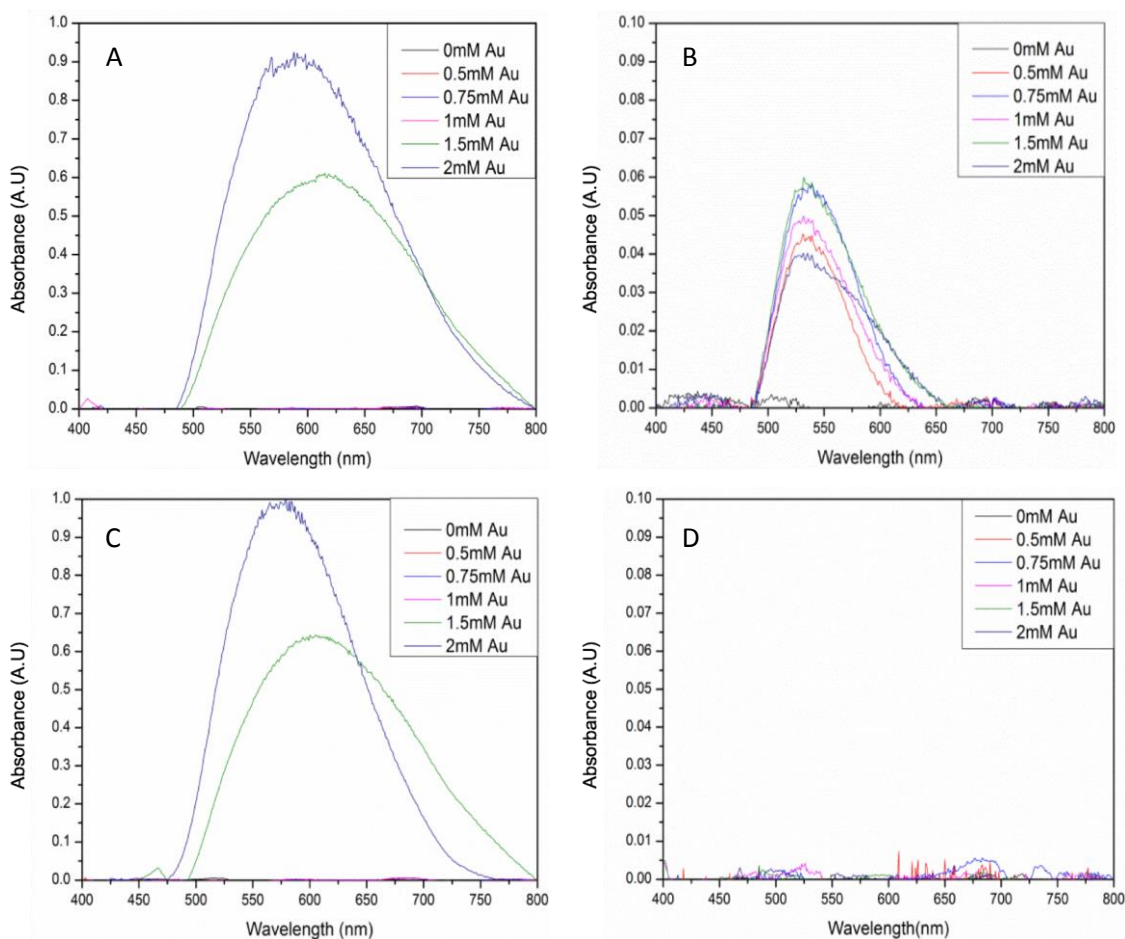


Figure 5.4: U.V. visible spectra of the AuNP isolated from BAECs which were exposed to various concentrations of Au in (a) DMEM (no phenol red or glucose) and (b) 1X PBS for 48 hours at 37⁰C and 5% CO₂ under static conditions. Both were supplement with a low concentration of FBS (1%). Detached cells were removed by centrifugation at 5,000 rcf for 10 minutes at 4⁰C and AuNPs isolated by centrifugation at 13,500 rcf for 30 minutes. The AuNP pelleted was then re-suspended in 2 mL of DI water. Experiments without BAECs (abiotic) were also performed for (c) DMEM and (d) 1 X PBS as before.

FBS is an important essential supplement in mammalian cell culture media, deprivation of which induces apoptosis. However, serum proteins such as albumin may complex or bind Au ions from solution. Therefore, the concentration of FBS should be minimised to increase AuNPs formation. Results show that the optimal FBS concentration is 1% w/w (Fig. 5.5). At this concentration, the height of the cell-bound AuNPs peak in the spectrophotometry at 530 nm is maximum. At lower FBS values, BAEC and BASMCs are less metabolically active, thus producing less AuNPs, at higher FBS concentration serum proteins bind to Au³⁺ ions, preventing AuNPs formation.

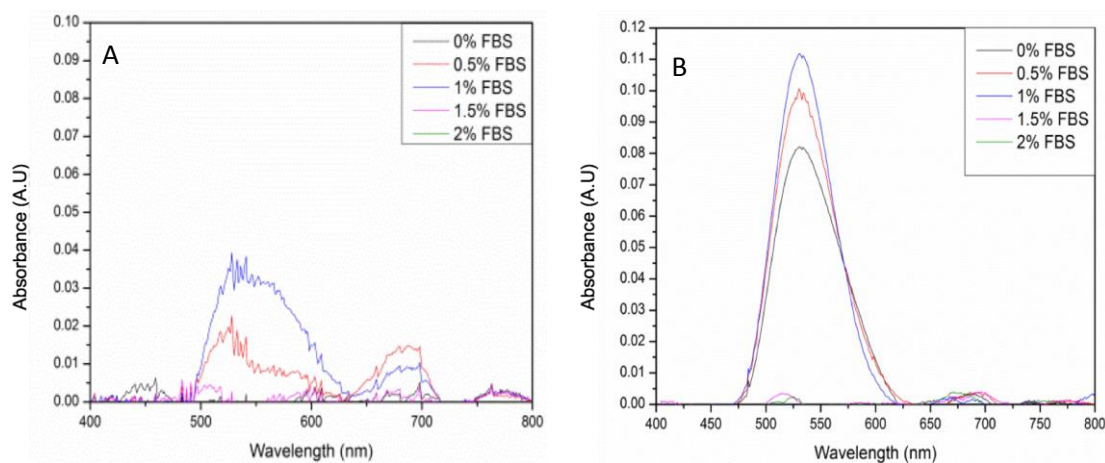


Figure 5.5: U.V. visible spectra of the AuNP isolated from (a) BAECs and (b) BASMCs which were exposed to 0.75mM Au in 1X PBS for 48 hours at 37⁰C and 5% CO₂ under static conditions. Detached cells were removed by centrifugation at 5,000 rcf for 10 minutes at 4⁰C and AuNPs spun down at 13,500 rcf for 30 minutes. The AuNP pellet was re-suspended in 2 mL of deionized water.

Au³⁺ is toxic to the BAEC and BASMCs at high concentrations. Therefore, the optimal Au³⁺ concentration for the AuNPs biosynthesis process needs to be determined. Figure 5.6 shows the spectrum of the AuNPs located in the spent media after 48 hours of the biosynthesis process. The Au peak at 525 nm increases with Au concentration up to 0.75-1.5mM. Further increase of Au concentration to 2mM Au decreases SPR peak intensity. Interestingly, the BASMCs appear to produce a greater abundance of AuNPs than the BAECs.

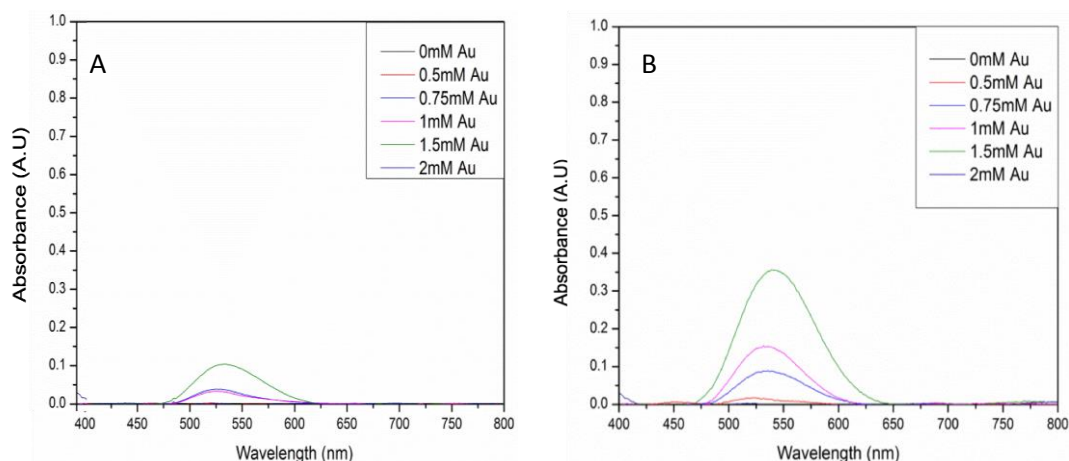


Figure 5.6: U.V. visible spectra of the AuNP isolated from BAECs and BASMC which were incubated with various concentrations of Au in 1X PBS supplemented with 1% FBS for 48 hours at 37⁰C and 5% CO₂. AuNPs were isolated from detached cells by centrifugation at 5,000 rcf for 10 minutes at 4⁰C and AuNPs spun down at 13,500 rcf for 30 minutes. The AuNP pellet was then re-suspended in DI water.

BAECs and BASMCs were examined by phase contrast microscopy to examine the effect of the Au salt on the cell lines. Fig. 5.7 and Fig 5.8 show that BAECs and BASMCs detach in the 0mM Au control , but did not for the solutions containing Au⁺³ ions. There is less detachment for the BASMCs than the BAECs.

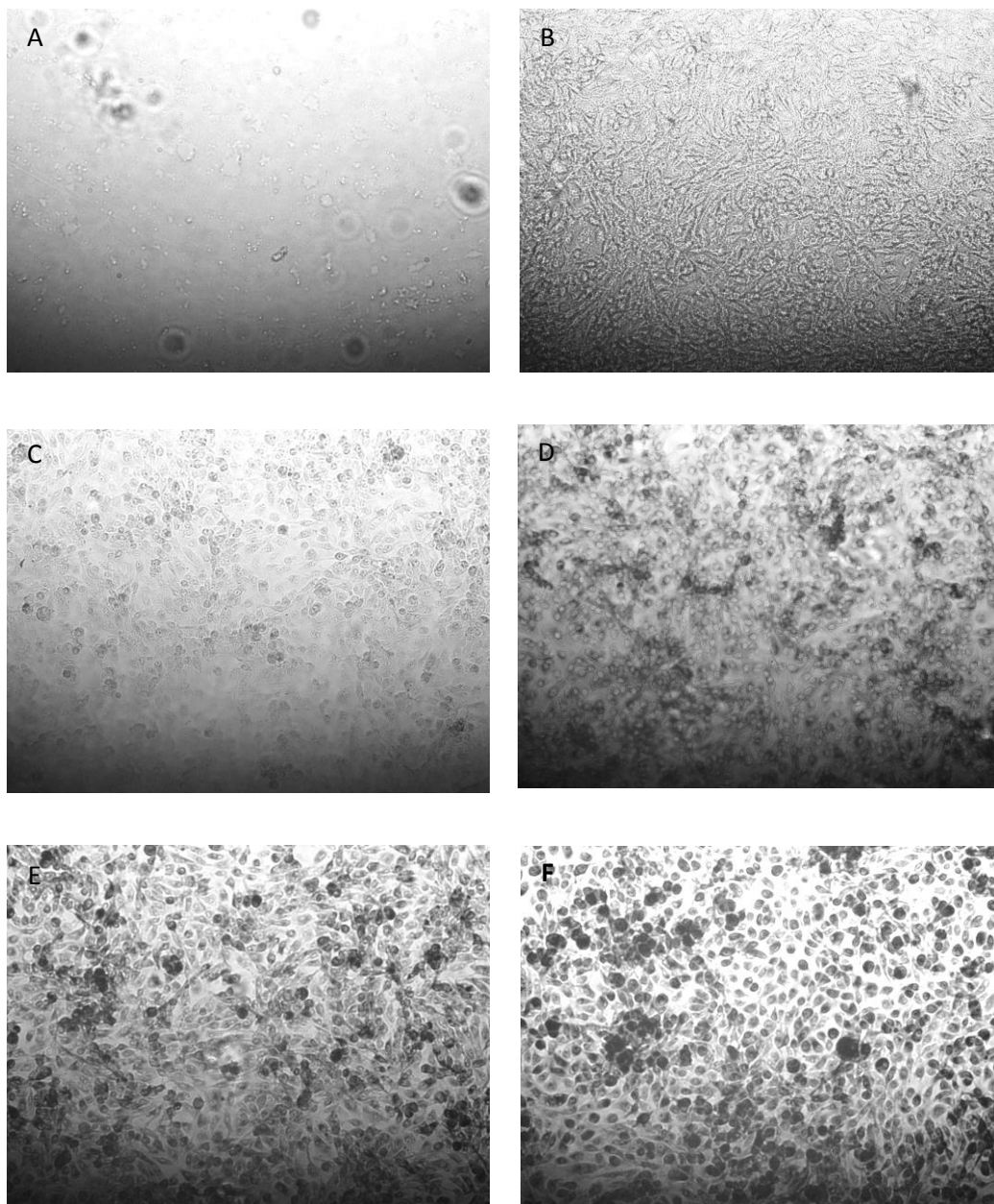


Figure 5.7: Phase contract microscope images of BAECs exposed to (A) 0mM Au, (B) 0.5mM Au, (C) 0.75mM Au, (D) 1mM Au, (E) 1.5mM Au and (F) 2mM Au in 1X PBS and 1% FBS with 1mM Ca and Mg for 48 hours at 37⁰C and 5% CO₂. Cells were examined using phase contrast light microscopy at 100X magnification

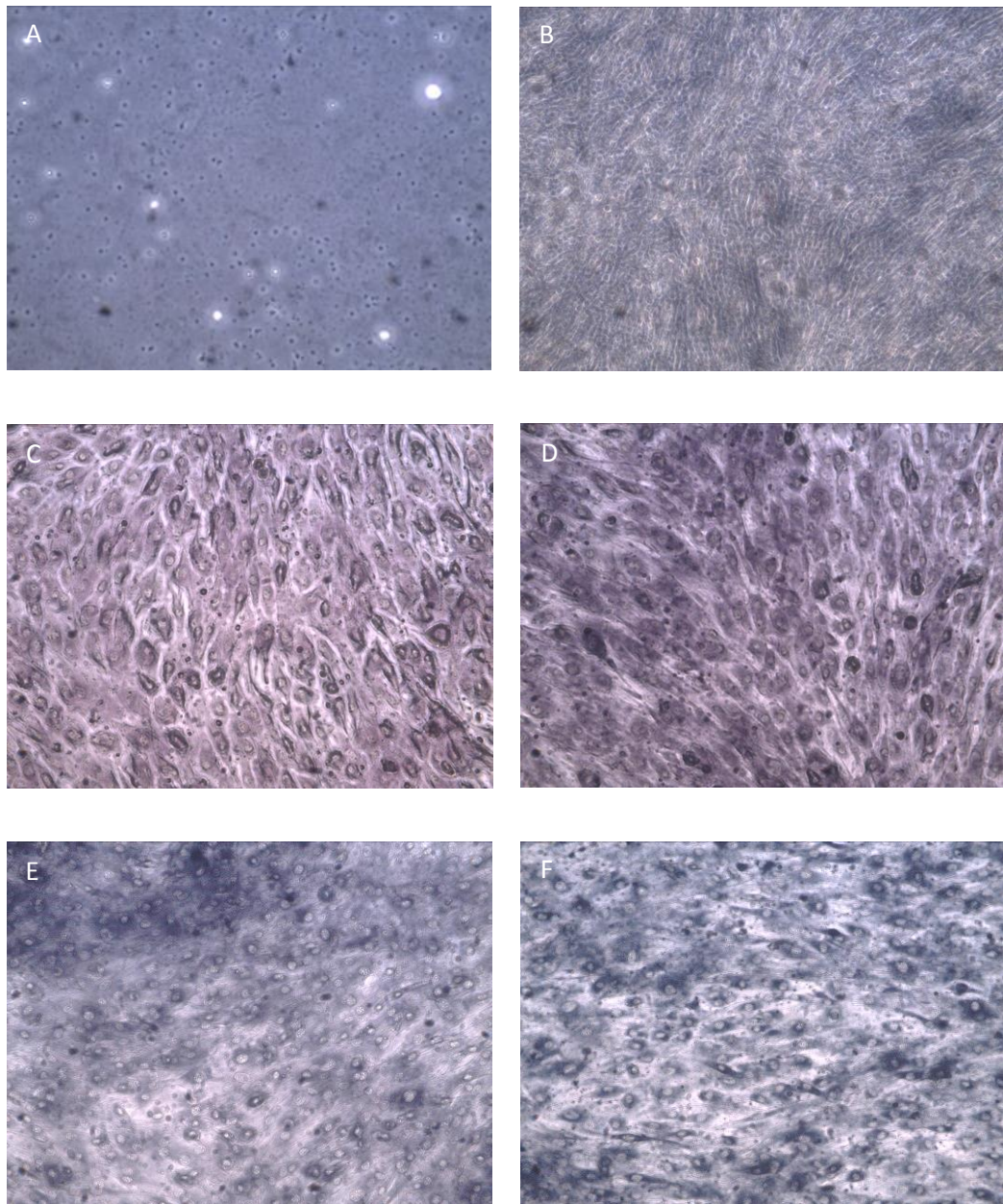


Figure 5.8: Phase contract microscope images of BASMCs exposed to (A) 0mM Au, (B) 0.5mM Au (C) 0.75mM Au, (D) 1mM (E) 1.5mM Au and (F) 2mM Au in 1X PBS and 1% FBS for 48 hours at 37⁰C and 5% CO₂. Cells were examined using phase contrast light microscopy at 100X magnification.

PBS lacks Ca and Mg ions, which is an important allosteric regulator of the adhesion proteins of BAECs and BASMCs. Upon supplementing the synthesis buffer with 1mM MgSO₄ and 1mM CaCl₂, the SPR peak increased by approximately a factor of 1/3 (Fig. 5.9).

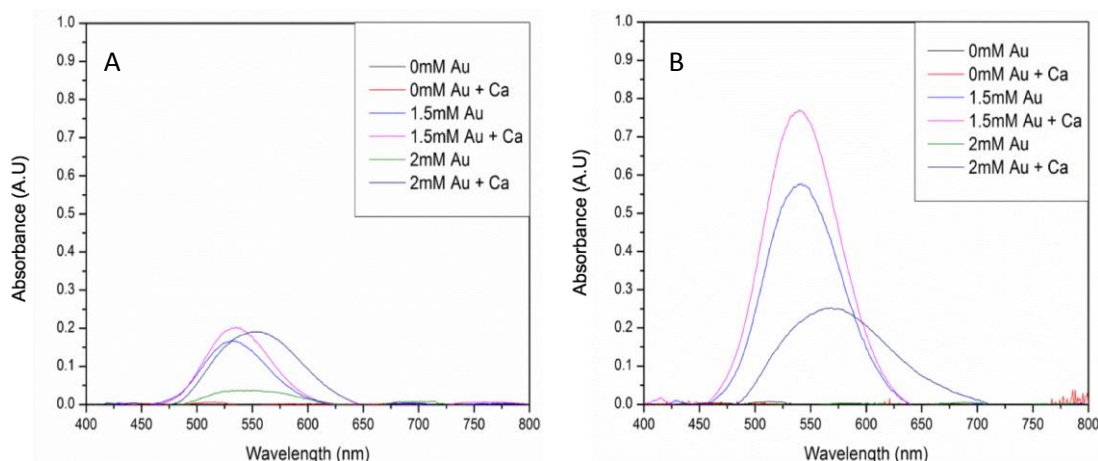


Figure 5.9: Addition of 1mM Ca and Mg to (A) BAEC and (B) BASMC culture. Confluent BAEC were exposed to 0, 1.5 or 2mM of Au with or without 1mM Ca and Mg ions.

Stability of AuNPs generated by the BAECs and BASMCs is unknown at present, therefore to examine cell associated AuNPs, the cells were washed with 1X PBS twice to remove loosely bound AuNPs and dead cells and spectra obtained by using a plate reader. Fig. 5.9 shows that AuNPs concentration is much lower than the cell associated AuNPs and does not significantly change upon Ca and Mg supplementation. As the examining secreted biosynthesized AuNPs in the spent media is easier to obtain, much more cost effective, less destructive on the AuNPs and shows a greater response in treatment than the cell associated fraction, we will compare AuNP abundance in the spent media as an indicator of AuNP biosynthesis.

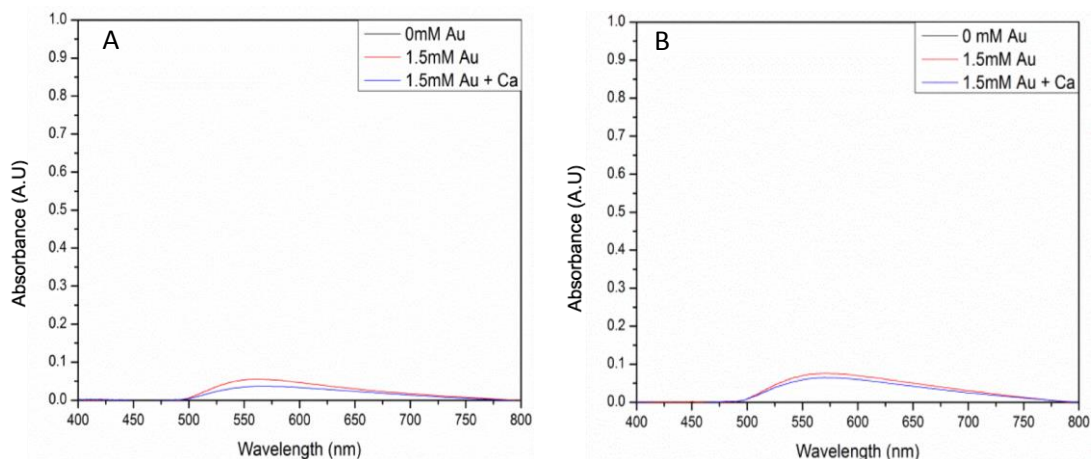


Figure 5.10: Examination of cell associated AuNPs produced by BAECs and BASMCs. Confluent BAECs and BASMC plates were incubated with various concentrations of Au in 1X PBS, 1mM MgSO₄ and 1% FBS for 48 hours at 37⁰C and 5% CO₂. Loosely bound AuNPs and detached cells were removed from the cells by washing with 1XPBS. Intracellular AuNPs were measured by Tecan Infinite M200 Plate reader.

The BAECs and BASMCs were also examined by phase contrast microscopy to ensure that the cells remain attached to the cell culture plate. Fig 5.11 and Fig. 5.12 show that BAECs and BASMCs remain attached to the surface of the well after 48 hours incubation with and with Au³⁺ upon the introduction of 1mM Ca and Mg ions into the synthesis buffer.

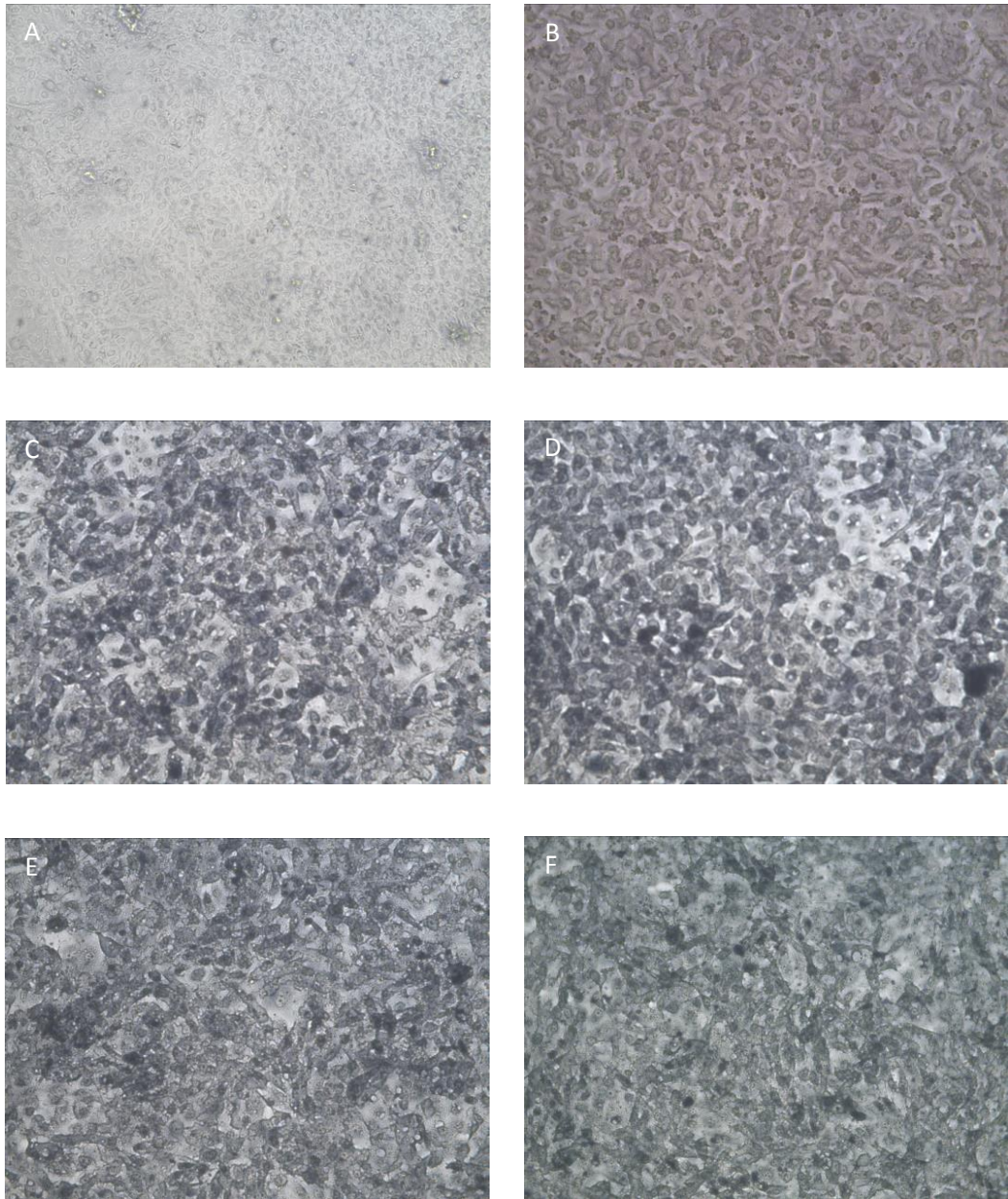


Figure 5.11: Phase contract microscope images of BAEC exposed to (A) 0mM Au without CaCl_2 and MgSO_4 (B) 0mM Au with 1mM CaCl_2 and 1mM MgSO_4 (C) 1.5mM Au without CaCl_2 and 1mM MgSO_4 , (D) 1.5mM Au with 1mM CaCl_2 and 1mM MgSO_4 (E) 2mM Au without CaCl_2 and MgSO_4 and (F) 2mM Au with 1mM CaCl_2 and 1mM MgSO_4 in 1X PBS and supplemented with 1% FBS for 48 hours at 37°C and 5% CO_2 . Cells were examined using phase contrast light microscopy at 100X magnification.

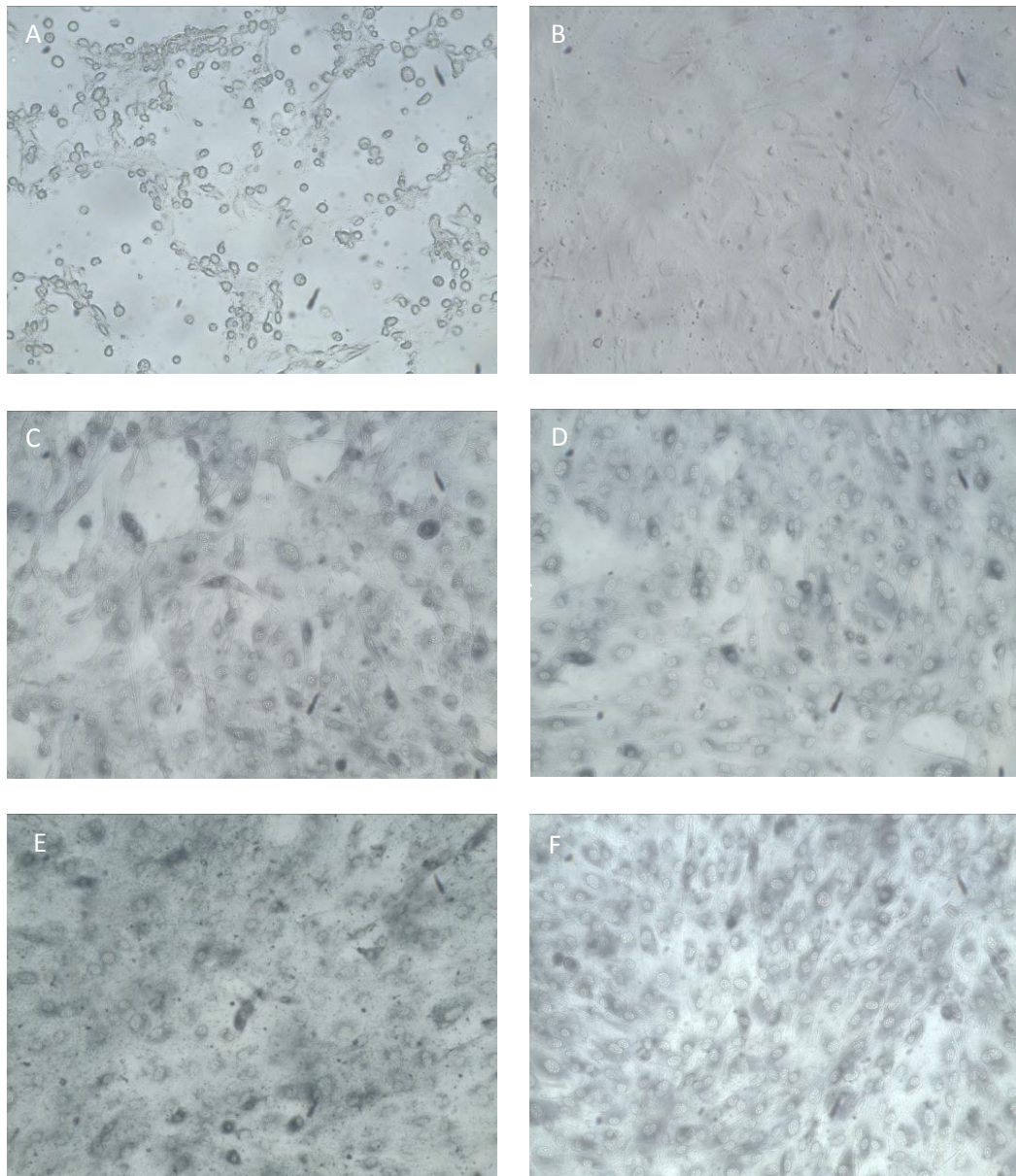


Figure 5.12: Phase contract microscope images of BASMCs exposed exposed to (A) 0mM Au without CaCl_2 and MgSO_4 (B) 0mM Au with 1mM CaCl_2 and 1mM MgSO_4 (C) 1.5mM Au without CaCl_2 and 1mM MgSO_4 , (D) 1.5mM Au with 1mM CaCl_2 and 1mM MgSO_4 (E) 2mM Au without CaCl_2 and MgSO_4 and (F) 2mM Au with 1mM CaCl_2 and 1mM MgSO_4 in 1X PBS and supplemented with 1% FBS for 48 hours at 37°C and 5% CO_2 . Cells were examined using phase contrast light microscopy at 100X magnification.

4.3.2 AuNP Characterisation

AuNPs were characterised in terms of their size, shape, crystallinity and surface chemistry. Fig. 5.13 below shows that AuNPs produced by BAECs and BASMCs are mostly small spheres. The SAED shows that the AuNPs produced by the BASMCs possess more crystal faces than the BAEC produced AuNPs.

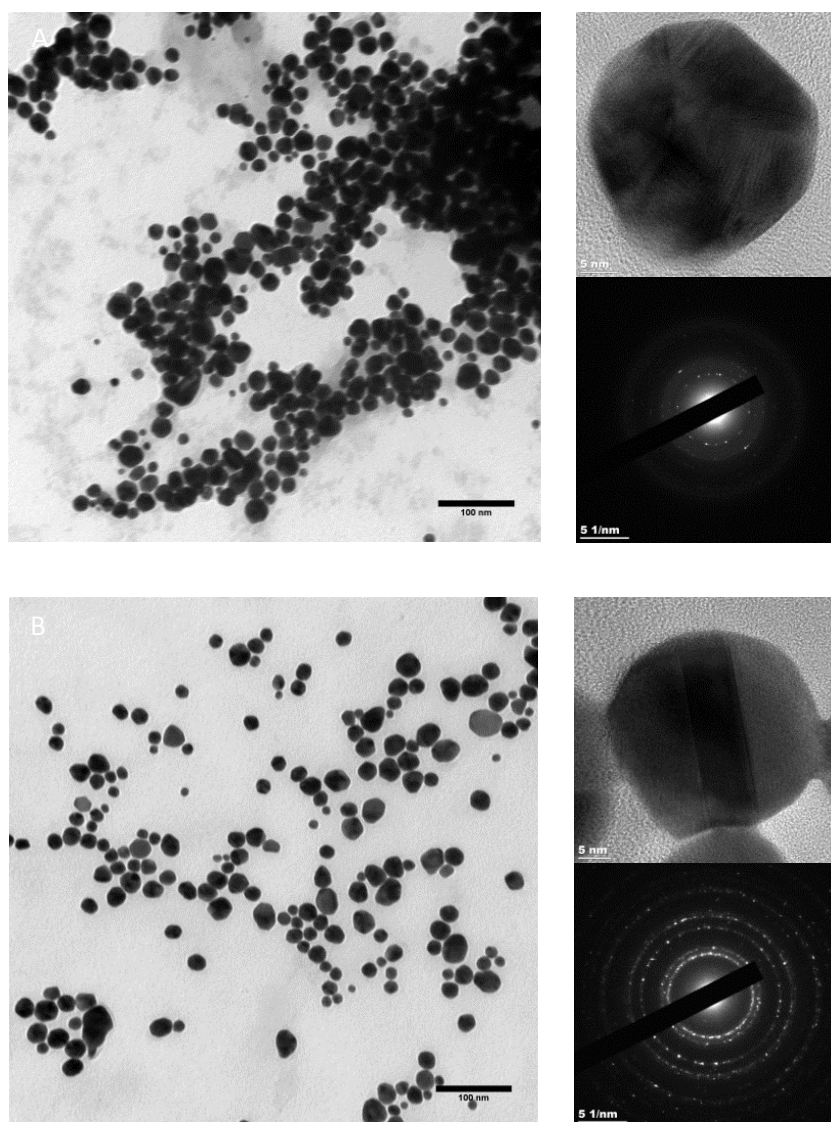


Figure 5.13: SAED and HR-TEM of AuNPs produced by BAECs (A) and BASMC (B) Analysis by Yina Guo.

Fig. 5.14 shows the size distribution of the AuNPs produced by BAECs and BASMCs plotted on a histogram. It reveals that AuNPs although similar, possess subtle differences. The AuNPs produced by BAECs are skewed towards the smaller AuNP size, while the BASMC produced AuNPs are skewed towards the larger AuNPs. Further the size distribution is slightly narrower for the BASMCs than the BAECs.

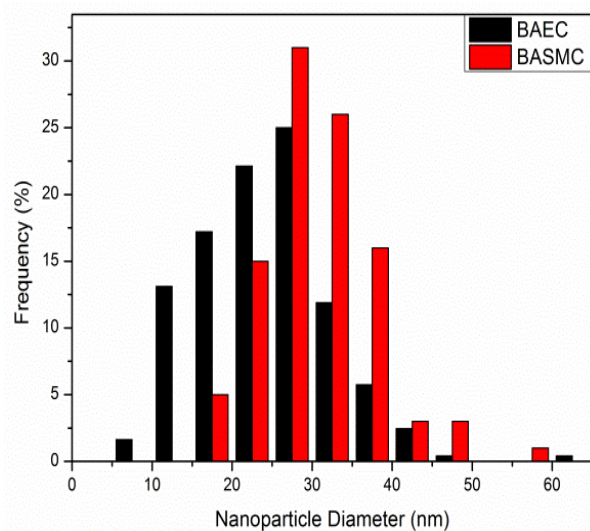


Figure 5.14: Histogram of AuNP particle sizes (measured by TEM) produced by BAECs and BASMCs

XRD analysis of AuNPs produced by BAEC and BASMCs (Fig. 5.15), showed that AuNPs produced by BAECs have Au (111), Au (220) planes, while the AuNPs produced by BASMC have Au (111), Au (220) and Au (311) planes.

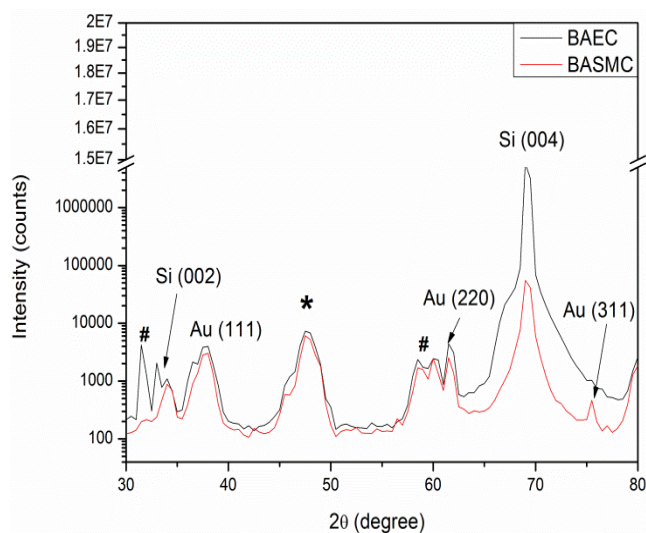


Figure 5.15: XRD of AuNPs isolated from the spent media of BAECs and BASMCs (n=3). * is due to the adhesive tape and # arises from XRD Cu K β and tungsten L α radiations from the X-ray tube. XRD analysis performed by Saikumar Inguva.

Table 5.1: Hydrodynamic sizes (DLS), particle size (TEM), d spacing and crystal size of the AuNPs produced by BAECs and BASMCs (n=3).

	DLS (nm)	TEM (nm)	d spacing (Å)	Crystal size (nm)
BAEC	75 ± 5	23 ± 2	2.3 ± 1	6 ± 1
BASMC	74 ± 6	23 ± 4	2.3 ± 2	5 ± 1

The lattice spacing (d spacing) of the AuNPs were calculated using Image j analysis, and used to calculate the crystal size along with the data for the Au (111) facet detected by XRD. Table 5.2 shows that that d spacing of the AuNPs produced by both cell phenotypes. However the crystal size is much lower than the particle size calculated by TEM.

FTIR analysis reveals bands at 3,400-3180, 2,914, 1,059 and 9,38cm⁻¹, which in the literature has been ascribed to NH or OH function groups, aldehydic C-H stretching Amide I bands, aliphatic C-N and D-H deformation (Kitching et al. 2014) . These bands are similar between cell phenotypes.

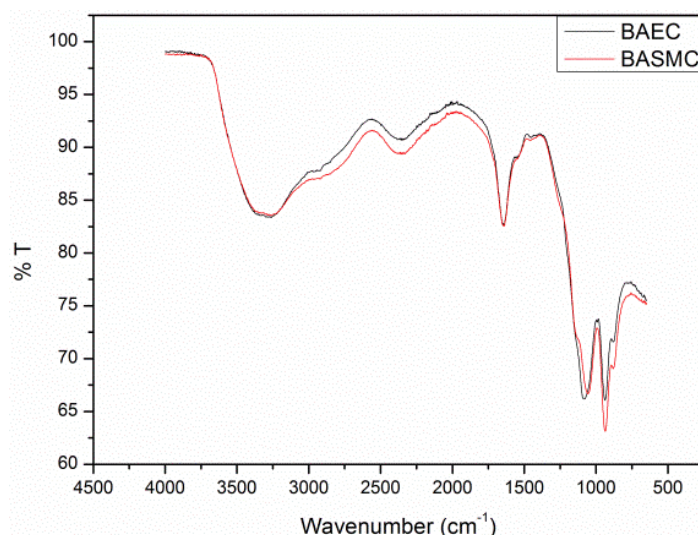


Figure 5.16: FTIR of powdered AuNPs produced by BAECs and BASMCs

4.3.3 Mechanism of Synthesis

In the media optimisation experiments, for low concentrations of Au^{3+} there were no AuNPs produced in DMEM but there were produced in PBS. A key difference between PBS and DMEM is the osmotic pressure; DMEM is isotonic while PBS is hypotonic. The effect of the osmotic pressure on AuNP biosynthesis was examined by alteration of the salt concentration by adding various amounts of NaCl. Fig. 5.17 shows that adding NaCl had no clear effect on AuNP biosynthesis.

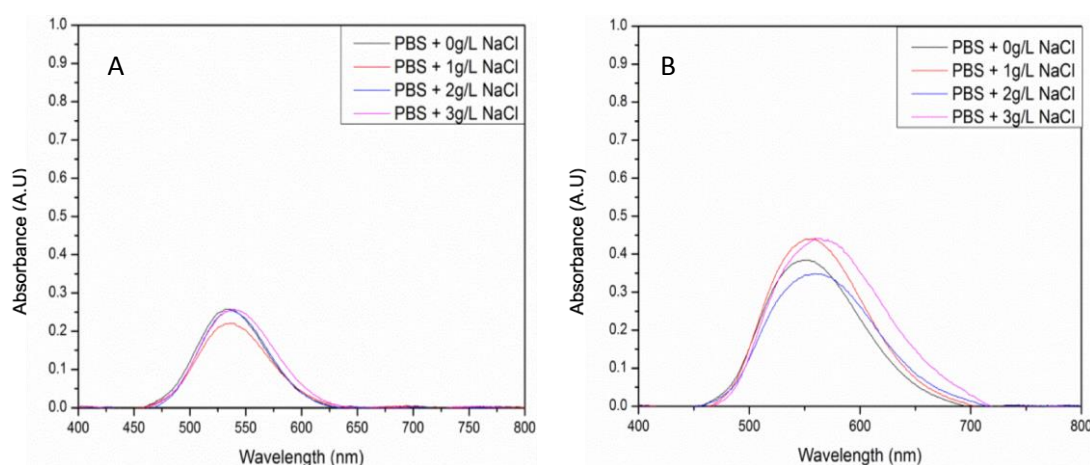


Figure 5.17: Effect of salt concentration on AuNP biosynthesis by (A) BAECs and (B) BASMCs

As osmotic strength does not play a clear role in AuNP, the oxidative stress response was then examined. The oxidative stress assay (Fig. 5.18) showed that the addition of Au did not induce oxidative stress, however the assay relied on the detection of H₂O₂ as a marker of oxidative stress, it is possible that AuNPs produced catalysed the decomposition of H₂O₂, as reported previously (He et al. 2012) .

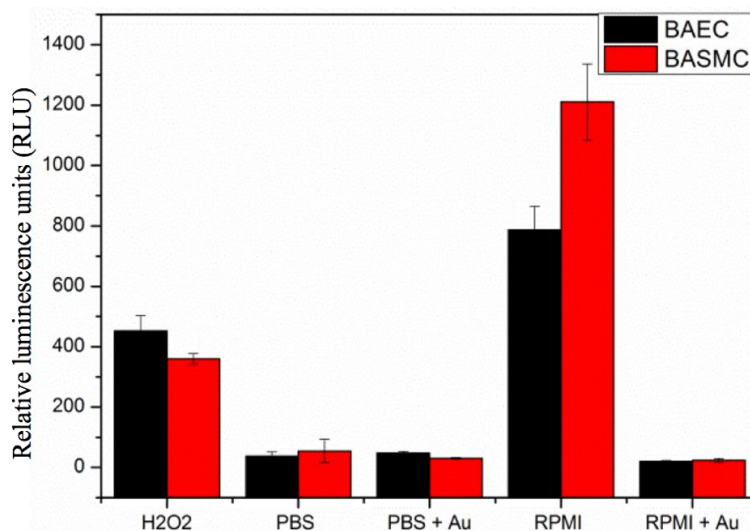


Figure 5.18: Oxidative stress assay of BAECs and BASMCs exposed to 1.5mM Au in PBS and RPMI. H₂O₂ was utilised as a control experiment.

Glutathione (GSH) is an important regulator of oxidative stress in the cell, and is important for tumour cell resistance to cis-platin. Buthionine sulphoximine (BSO) is an irreversible inhibitor of gamma-glutamylcysteine synthetase, and consequently lowers cellular GSH levels. BAECs and BASMCs were pretreated for 16 hours with 1 and 2mM BSO before Au³⁺ exposure to determine the role of GSH on AuNP biosynthesis. Fig. 5.19 shows that BSO pre-treatment did not affect AuNP biosynthesis.

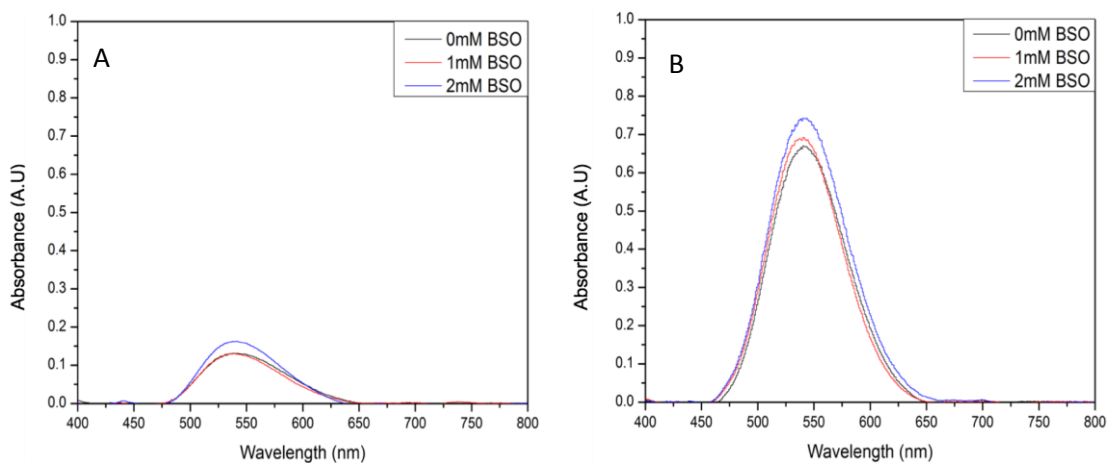


Figure 5.19: U.V. visible of AuNPs isolated from BAECs and BASMCs pretreated with 1 and 2mM BSO for 15 hours and then exposed to 1.5mM Au in 1 X PBS with 1mM Ca and Mg ions supplemented with 1% FBS.

BSO pre-treatment does not appear to have an effect in AuNP biosynthesis by BAECs and BASMCs, however the ROS produced by oxidative stress may play a role in AuNP biosynthesis. To induce the ROS production, BAECs and BASMCs were pretreated with various concentrations of H_2O_2 for 24 hours before Au^{3+} exposure. Fig. 5.20 shows that for BAECs, low levels of H_2O_2 (up to 0.05mM) do not induce AuNP biosynthesis, however above this concentration, the abundance of AuNPs increases significantly. For BASMCs, there is an increase at 0.05mM H_2O_2 , however this drops at 1mM H_2O_2 , possibly due to H_2O_2 toxicity.

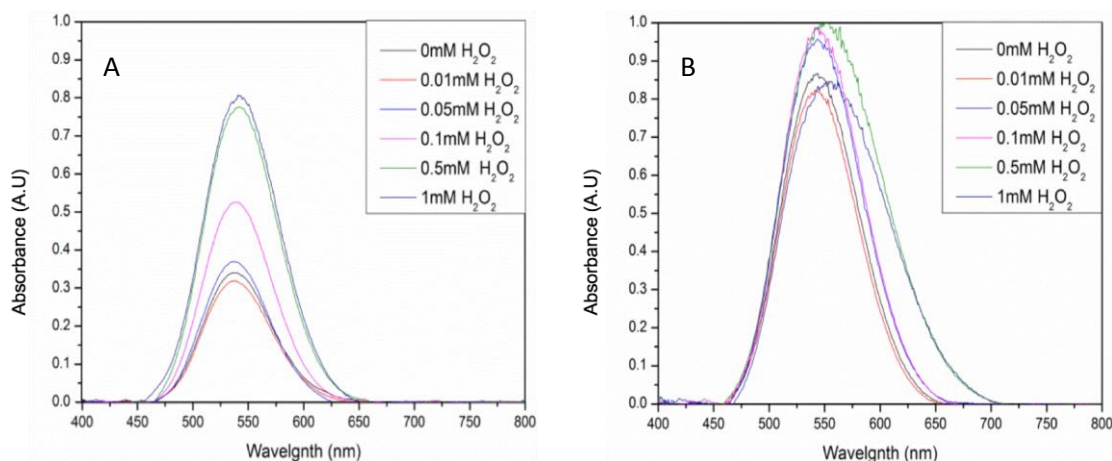


Figure 5.20: U.V. visible of AuNPs isolated from BAECs and BASMCs pretreated with various concentrations of H_2O_2 for 24 hours and then exposed to 1.5mM Au in 1 X PBS with 1mM Ca and Mg ions supplemented with 1% FBS.

5.4 Discussion

AuNP biosynthesis appears to be influenced by media selection, FBS and presence of Ca and Mg ions, which indicate that the cell is actively involved in the AuNP production. AuNPs were not produced in the cell culture media (DMEM) at low Au³⁺ concentrations, but AuNPs were produced at high levels of Au³⁺, which were indistinguishable from the abiotic control. Further AuNPs were produced at all concentrations of Au³⁺ for the PBS for the biotic experiment, but not for the control. This suggests that either DMEM contains Au³⁺ binding components or that the BAEC must be under stress to produce the AuNPs. The optimal FBS concentration is low for cell culture (1% v/v), which is not unexpected as although FBS is important to maintain cell metabolism and prevent apoptosis, however FBS also contains anti oxidants and metal binding proteins. In other studies focusing on oxidative stress, FBS is usually kept low, for example Takahashi et al used 2% FBS when examining the effect of BSO on methylglyoxal induced apoptosis of BAECs (Takahashi et al. 2010). The role Ca and Mg ions on the role of AuNP biosynthesis may be due to their role in cell adhesion, as they act as allosteric regulators of cell surface adhesions. Interestingly, Au³⁺ ions may also play a role in cell adhesion, however the mechanism of how Au³⁺ aids in cell attachment *in-vitro* is not understood at present.

AuNPs produced by BAECs and BASMCs SPR peak position was 530nm, which is characteristic of AuNPs size of 30nm (Agarwal et al. 2014) , however the TEM images show that the particle sizes were $23 \pm 2\text{nm}$ and $23 \pm 4\text{nm}$ respectively. This disagreement possibly arose from the large size distribution of the AuNPs, and some amount of AuNP aggregation. DLS analysis shows a large hydrodynamic size, however biogenic AuNPs are capped by biomolecules such as proteins which increases the particle hydrodynamic size. The size distribution of the biogenic AuNPs is wide for both BAEC and BASMC, between 5-60nm, which is typical for AuNP biosynthesis (Kitching et al. 2014) . Wang et al, showed that AuNPs produced by HepG2 had a diameter of 2nm and a range between 2-3nm, which suggests a higher intracellular concentration of ROS produces smaller AuNPs (Anshup et al. 2005). Although the mean size both AuNPs produced for both BAECs and BASMCs are similar, the histogram of the AuNP sizes are either skewed towards the either small AuNPs for BAEC or large AuNPs for BASMC, which suggest that cell phenotype has a subtle influence on AuNP biosynthesis, possibly due to the difference in the level of ROS production.

XRD analysis of the AuNPs show that AuNPs produced by BASMC have an Au (111), Au (220) and Au (311) plane, while BAEC produce AuNPs are missing the Au (311) plane. SAED analysis confirms that the BASMCs have the Au (111), Au (220) and Au (311) plane and BAECs are indeed missing the Au (311) plane. XRD analysis on the intracellular AuNPs produced by HEK-293 and HeLa cells showed Au (111), Au (200), Au (220) planes and were missing the Au (311) plane. As with this report the Au (111) plane is the most dominant in the XRD analysis of the AuNPs produced by HEK-293 and Hela (Anshup et al. 2005). These results suggest that cell phenotype may have a subtle effect of AuNP crystallisation.

HRTEM analysis shows that the d spacing for the AuNPs is $2.3 \pm 1 \text{ \AA}$ for BAEC and $2.3 \pm 2 \text{ \AA}$ for BASMC, which was used along with the data for the Au (111) plane to calculate crystal size (as Au crystals have a cubic structure, the Au (111) plane is sufficient). The crystal size is much smaller than the particle size, and along with the wide XRD peaks demonstrate that the particles are semi crystalline in nature, due to the ambient temperature of their synthesis.

FTIR suggests that proteins are the main capping ligand and that cell phenotype does not affect AuNP capping. However FTIR is a broad characterisation technique, and would not be able to show the differences in proteins that make up the capping layer.

Also media selection influenced AuNP biosynthesis, we hypothesized that the PBS induced some sort of stress response, which also produce AuNPs. A key difference between the DMEM and the PBS, is that PBS has a lower osmotic strength than DMEM, which induces hypotonic stress. This hypotonic stress has been shown to induce ERK1/2, SPAK/JNK in a spontaneously immortalized human keratinocyte cell line (HaCaT) by in vitro kinases assay. The authors also found that hypotonicity also led to a rapid dose dependent phosphorylation of elk-1, PKB/Akt and upregulation of E-cadherin mRNA and protein levels (Kippenberger et al. 2005) . The upregulation of ERK1/2 and JNK kinases has also been reported to also be induced by H₂O₂ (Romero and Lamas 2014) . This would suggest that hypotonic stress and oxidative stress share a subset of cell signalling pathways. However when we altered the osmotic strength of the buffer, we found that AuNP biosynthesis was not affected. This suggests that 1.5mM Au³⁺ alone is enough to induce a cell response.

BSO pretreatment, which has been reported to promote oxidative stress and cell death upon methylglyoxal exposure, did not produce AuNPs, which suggests that GSH may have no role in AuNP biosynthesis in BAECs or BASMCs or this result may suggest that the GSH levels in BAECs and BASMCs prior to Au³⁺ exposure is sufficient to produce AuNPs, as GSH may be recycled from GSSG rather than synthesized new GSH from the condensation reaction between γ -EC and glycine.

H₂O₂ induces ROS generation, such as O₂⁻ and H₂O₂ which may reduce Au³⁺ ions and produce AuNPs. H₂O₂ pretreatment did appear to induce AuNP biosynthesis at high H₂O₂ concentrations. This finding supports the conclusion of Wang et al, that the increased levels of ROS production in cancer cells increased AuNP biosynthesis (Anshup et al. 2005).

5.5 Conclusions

AuNP biosynthesis in mammalian cells is optimised in 1X PBS, 1% FBS with 1mM Ca and Mg ions, which is a balance of mammalian cell activity and concentration of Au complexing agents. AuNP particle size is not affected by cell type, however cell type does affect AuNP abundance and crystallinity. This difference may be due to the different Au³⁺ reduction rate between the cell types.

5.6 Future Work

Future work should examine the cell associated AuNPs in terms of size and crystallinity. As the mechanism of AuNP synthesis remains unclear, future work should focus on understanding the mechanism of AuNP biosynthesis.

Chapter 6 Concluding Remarks

This thesis examined noble metal nanoparticle biosynthesis from 3 different organisms, bacteria, fungi and mammalian cells. Due to the wide variety in the response mechanisms these cell types employ in response to metal ion toxicity, MNP biosynthesis in each organism has its associated pros and cons.

The application of a mild electrochemical potential increased the synthesis rate of AgNPs by *Shewanella oneidensis* biofilms. AgNPs produced were expected to be under 10nm in diameter with a small size distribution, as reported for extracellular synthesized AgNPs produced by planktonic cell *S. oneidensis* cultures (Wang et al. 2009, Suresh et al. 2010). However, the AgNPs produced were large ($45 \pm 1\text{nm}$) and had a broad size distribution which only increased with decreasing applied potential. Further optimisation is needed to improve particle size and distribution before this technique is viable for scale up. MNP synthesis may be improved by the application of an oxidation-reduction cycle and examination of other electroactive bacterial species, such as *Geobacter* and utilisation of other materials as a working electrode.

The fungal cell surface protein extracts produced small spherical AuNPs of approximately 20nm, with a narrower size distribution; with the exception of the SDS protein extract synthesized AuNPs. Future work should optimise the ratio of protein concentration to initial Au^{3+} concentration, to improve AuNP mean size and size distribution.

Bovine aortic endothelial cells (BAECs) produced a lower abundance of the AuNPs than the Bovine aortic smooth muscle cells (BASMCs). The distribution of the AuNPs produced by BAECs favours larger AuNP synthesis compared to the BASMC, which suggests a faster reduction rate. Subtle differences in AuNP crystallinity may also be due the difference in the metal reduction rate. The mechanism of AuNP synthesis in mammalian cells remains elusive, although the generation of ROS may be involved. Future mechanistic study should focus on protein extracts to eliminate variables inherent in live cell experiments.

Overall MNPs synthesis is affected by biomass concentration and buffer selection. MNP physicochemical properties such as size and aggregation are dependent on cell type and reducing potential. However, crystallinity is subtly affected by protein

structure, cell type and reducing potential, possibly due to the temperature of the synthesis being the predominant factor in MNP crystallisation. Particle of the bioelectrochemically synthesized AgNPs suggests that a faster reduction rate increases MNP size. MNP shape was not altered significantly by the reducing potential or cell type, however denatured proteins did produce large nanoflowers.

The high cost of mammalian cell culture is a major drawback, especially when the physicochemical properties of the Triton X-100 extract synthesized AuNPs are identical to the BASMC synthesised AuNPs. Further the protein extracts offer a more controllable biosynthesis of the MNPs than using viable mammalian cells. Therefore, fungi may be the most suitable host for the biosynthesis of MNPs at an industrial scale. However, mammalian cell synthesis may offer to produce AuNPs with lower immunogenicity. Future experiments for mammalian cell AuNP synthesis should examine Chinese Hamster Ovary (CHO) cultures, as due to their relative low cost of culture are already utilised in the synthesis for other biopharmaceutical products in industrial scale.

Bibliography

Agarwal, S., Mishra, P., Shivange, G., Kodipelli, N., Moros, M., Fuente, J. and Anindya, R. 2014. Citrate-capped gold nanoparticles for the label-free detection of ubiquitin C-terminal hydrolase-1. *Analyst*.

Amoruso, S., Nedyalkov, N.N, Wang, X., Ausanio, G., Bruzzese, R. and Atanasov, P.A. (2013). Ultrashort-pulse laser ablation of gold thin film targets: Theory and experiment. *Thin Solid Films*. **550**.

Anil-Kumar, S., Abyaneh, M.K., Gosavi, S.W., Kulkarni, S.K., Pasricha, R., Ahmad, A. and Khan, M.I. (2007) Nitrate reductase-mediated synthesis of silver nanoparticles from AgNO₃. *Biotechnology Letters*. **29** (3), 439-445.

Anshup, Venkataraman, S., Subramaniam, C., Kumar, R., Priya, S., Kumar, S., Omkumar, John, A. and Pradeep (2005). Growth of Gold Nanoparticles in Human Cells. *Langmuir* **21**(25),11562-11567.

Bargar, J.R., Bernier-Latmani, R., Giammar, D.E. and Tebo, B.M. (2008). Biogenic Uraninite Nanoparticles and Their Importance for Uranium Remediation. *Elements*. **4** (6), 407412.

Bazylnski, D. & Frankel, R. (2004) Magnetosome formation in prokaryotes. *Nature Reviews Microbiology*. **2** (3), 217–230.

Beaufort, L. Couapel, M., Buchet, N., Claustre, H. and Goyet, C. (2008) Calcite production by coccolithophores in the south east Pacific Ocean. *Biogeosciences*. **5** (4), 1101–1117.

Bhambure, R., Bule, M., Shaligram, N., Kamat, M. and Singhal. R. (2009) Extracellular Biosynthesis of Gold Nanoparticles using *Aspergillus niger* – its Characterization and Stability. *Chemical Engineering & Technology*. **32** (7), 10361041.

Binupriya, A.R., Sathishkumar, M. and Yun, S.I. (2010) Biocrystallization of silver and gold ions by inactive cell filtrate of *Rhizopus stolonifer*. *Colloids and surfaces. B, Biointerfaces*. **79** (2), 531534.

Bornhorst, J. & Falke, J. (2000) Purification of proteins using polyhistidine affinity tags. *Methods in enzymology*. **326**, 245–254.

Breuer, M., Rosso, K. M., Blumberger, J., & Butt, J. N. (2015). Multi-haem cytochromes in *Shewanella oneidensis* MR-1 : structures , functions and opportunities. *Interface*. **12** (102).

Cai, H. 2005. Hydrogen peroxide regulation of endothelial function: Origins, mechanisms, and consequence. *Cardiovascular Research*. **68**. 26–36.

Carmona-Martinez, A., Harnisch, F., Fitzgerald, L.A., Biffinger, J.C., Ringeisen, B.R. and Schröder, U. (2011). Cyclic voltammetric analysis of the electron transfer of *Shewanella oneidensis* MR-1 and nanofilament and cytochrome knock-out mutants. *Bioelectrochemistry*. **81** (2), 74–80.

Castro-Longoria, E., Vilchis-Nestor. A.R. and Avalos-Borja, M. (2010) Biosynthesis of silver, gold and bimetallic nanoparticles using the filamentous fungus *Neurospora crassa*. *Colloids and Surfaces B: Biointerfaces*. **83** (1), 42–48.

Chauhan, A., Zubair, S., Tufail, S., Sherwani A., Sajid M., Raman S.C., Azam A. and Owais M. (2011). Fungus-mediated biological synthesis of gold nanoparticles: potential in detection of liver cancer. *International Journal of Nanomedicine*. **6**, 2305–2319.

Cheng, S. & Logan, B. (2011) High hydrogen production rate of microbial electrolysis cell (MEC) with reduced electrode spacing. *Bioresource Technology*. **102** (3), 3571-3574.

Congeevaram, S., Dhanarani, S., Park, J., Dexilin, M. and Hamaraiselvi, K. (2007) Biosorption of chromium and nickel by heavy metal resistant fungal and bacterial isolates. *Journal of Hazardous Materials*. **146** (1-2), 270277.

Cordas, C.M., Guerra L.T, Xarier, C. and Moura, J.J.G. (2008) Electroactive biofilms of sulphate reducing bacteria. *Electrochimica Acta*. **54** (1), 2934.

Corte, S., Hennebel, T., Fitts, J.P., Sabbe, T., Biliznuk, V., Verschuere, S., van der Lelie, D., Verstrate, W. and Boon, N. (2011) Biosupported bimetallic Pd-Au nanocatalysts for dechlorination of environmental contaminants. *Environmental science & technology*. **45** (19), 8506–8513.

Corte, S., Hennebel, T., Verschuere, S., Cuvelier, C., Verstraete, W. and Boon, N. (2011) Gold nanoparticle formation using *Shewanella oneidensis*: a fast biosorption and slow reduction process. *Journal of Chemical Technology and Biotechnology*. **86** (4), 547-553.

Coyle, C. and Kader, K. 2007. Mechanisms of H₂O₂-Induced Oxidative Stress in Endothelial Cells Exposed to Physiologic Shear Stress. *ASAIO Journal*. **53** (1), 1722.

Croesea, E., Jeremiase, A.W., Marshall, I.P.G., Spormann, A.M., Euverink, G.J.W., Geelhoed, J.S., Stams, A.J.M. and Plugge, C.M. (2014) Influence of setup and carbon source on the bacterial community of biocathodes in microbial electrolysis cells. *Enzyme and microbial technology*. **61** (62), 67–75.

Dai, H. (2002) Carbon Nanotubes: Synthesis, Integration, and Properties. *Accounts of Chemical Research*. **35** (12), 1035–1044.

Das, S., Liang, J., Schmidt, M., Laffir, F. and Marsili, E. (2012) Biomineralization mechanism of gold by zygomycete fungi *Rhizopus oryzae*. *ACS nano*. **6** (7), 6165–6173.

Das, S., Das, A.R. and Guha, A.K. (2009). Gold nanoparticles: microbial synthesis and application in water hygiene management. *Langmuir : the ACS journal of surfaces and colloids*. **25** (14), 8192–8199.

Das, S., Dickinson, C., Lafir, F., Brougham, D.F. and Marsili, E. (2012) Synthesis, characterization and catalytic activity of gold nanoparticles biosynthesized with *Rhizopus oryzae* protein extract. *Green Chemistry*. **14** (5), 1322.

- Du, L., Xian, L. and Feng, J.X. (2010) Rapid extra-/intracellular biosynthesis of gold nanoparticles by the fungus *Penicillium* sp. *Journal of Nanoparticle Research*. **13** (3), 921-930.
- Durán, N., Marcato P.D., Durán M., Yadav A., Gade A. and Rai M. (2011) Mechanistic aspects in the biogenic synthesis of extracellular metal nanoparticles by peptides, bacteria, fungi, and plants. *Applied microbiology and biotechnology*. **90** (5), 1609–1624.
- Epifanio, M., Inguva, S., Kitching, M., Mosnier, J.P. and Marsili, E. (2015) Effects of atmospheric air plasma treatment of graphite and carbon felt electrodes on the anodic current from *Shewanella* attached cells. *Bioelectrochemistry*. [Online]
- Fernández-Blanco, Colina, A., Heras, A., Ruiz, V. and López-Palacios, J. (2012) Multipulse strategies for the electrosynthesis of gold nanoparticles studied by UV/Vis spectroelectrochemistry. *Electrochemistry Communications*. **106**, 186-193.
- Flexer, V., Marque, M. Donose, B.C., Viridis, B. and Keller, J. (2013) Plasma treatment of electrodes significantly enhances the development of anodic electrochemically active biofilms. *Electrochimica Acta*. **108**, 566- 574.
- Gao H., Obraztova A., Stewart N., Popa R., Fredrickson J.K., Tiedje J.M., Nealson K.H. and Zhou J. (2006) *Shewanella loihica* sp. nov., isolated from iron-rich microbial mats in the Pacific Ocean. *International Journal of Systematic and Evolutionary Microbiology*. **56** (8), 1911–1916.
- Geim, A. & Novoselov, K. (2007) The rise of graphene. *Nature Materials*. **6** (3), 183–191.
- Ghodake G., Deshpande N.G., Lee Y.P. and Jin E.S. (2010) Pear fruit extract-assisted room-temperature biosynthesis of gold nanoplates. *Colloids and Surfaces B: Biointerfaces*. **75** (2), 584–589.
- Ghosh, P., Han, G., De, M., Kim, C.K. and Rotello, V.M. (2008) Gold nanoparticles in delivery applications. *Advanced Drug Delivery Reviews*. **60** (11), .

Girard, V., Dieryckx, C., Job, C., and Job, D. (2013) Secretomes: the fungal strike force. *Proteomics*. **13**, 597–608.

Gu, H. Ho, P.L., Tong, E., Wang, L. and Xu, B. (2003) Presenting Vancomycin on Nanoparticles to Enhance Antimicrobial Activities. *Nano Letters*. **3** (9), 1261-1263.

Gupta, S., Devi, S. and Singh, K. (2011) Biosynthesis and characterization of Au-nanostructures by metal tolerant fungi. *Journal of Basic Microbiology*. **51** (6), 601–606.

Harnisch, F., Wirth, S. and Schröder, U. (2009) Effects of substrate and metabolite crossover on the cathodic oxygen reduction reaction in microbial fuel cells: Platinum vs. iron(II) phthalocyanine based electrodes. *Electrochemistry Communications*. **11** (11), 2253-2256.

Huang, J., Li, Q., Sun, D., Lu, Y., Su, Y., Yang, X., Wang, H., Wang, Y., Shao, W. and He, N. (2007) Biosynthesis of silver and gold nanoparticles by novel sundried *Cinnamomum camphora* leaf. *Nanotechnology*. **18** (10), 105104.

He, W., Zhou, Y.-T., Wamer, W., Hu, X., Wu, X., Zheng, Z., Boudreau, M. and Yin, J.-J. 2012. Intrinsic catalytic activity of Au nanoparticles with respect to hydrogen peroxide decomposition and superoxide scavenging. *Biomaterials*. **34** (3), 765–773.

He, Y., Liu, S.P., Kong, L. and Liu, Z.F. (2005) A study on the sizes and concentrations of gold nanoparticles by spectra of absorption, resonance Rayleigh scattering and resonance non-linear scattering. *Spectrochimica Acta Part A: Molecular and Biomolecular Spectroscopy*. **61** (13-14), 2861-2866.

Huang, S.H. (2007) Gold nanoparticle-based immunochromatographic assay for the detection of *Staphylococcus aureus*. *Sensors and Actuators B: Chemical*. **127** (2), 335-340.

Huang C., Moosmann M., Jin J., Heiler T., Walheim S. and Schimmel, T. (2012) Polymer blend lithography: A versatile method to fabricate nanopatterned self-assembled monolayers. *Beilstein journal of nanotechnology*. **3**, 620–628.

Huang X., Jain P.K., El-Sayed I.H. and El-Sayed M.A. (2007) Plasmonic photothermal therapy (PPTT) using gold nanoparticles. *Lasers in Medical Science*. **23** (3), 217–228.

Icopini G., Lack J.G., Hersman L.E., Neu M.P. and Boukhalifa H. (2009) Plutonium(V/VI) Reduction by the Metal-Reducing Bacteria *Geobacter metallireducens* GS-15 and *Shewanella oneidensis* MR-1. *Applied and environmental microbiology*. **75** (11), 3641–3647.

Inguva, S., Vijayaraghavan, R.K., McGlynn, E. and Mosnier, J.P. (2015) Highly transparent and reproducible nanocrystalline ZnO and AZO thin films grown by room temperature pulsed-laser deposition on flexible Zeonor plastic substrates. *Materials Research Express*. **2** (9), 096401.

Kalathil, S., Lee, J. and Cho, M.H. (2011) Electrochemically active biofilm-mediated synthesis of silver nanoparticles in water. *Green Chemistry*. **13** (6), 1482.

Kalishwaralal K., Deepak V., Ram Kumar Pandian S., Kottaisamy M., Barathmani Kanth S., Kartikeyan B. and Gurunathan S. (2010) Biosynthesis of silver and gold nanoparticles using *Brevibacterium casei*. *Colloids and surfaces. B, Biointerfaces*. **77** (2), 257–262.

Kholoud M.M., El-Nour, A., Eftaiha, A., Al-Warthan, A. and Ammar, A.A. (2010) Synthesis and applications of silver nanoparticles. *Arabian Journal of Chemistry*. **3** (3).

Kim D.H., Viventi J., Amsden J.J., Xiao J., Vigeland L., Kim Y.S., Blanco J.A., Panilaitis B., Frechette E.S., Contreras D., Kaplan D.L., Omenetto F.G., Huang Y., Hwang K.C., Zakin M.R., Litt B. and Rogers J.A. (2010) Dissolvable films of silk fibroin for ultrathin conformal bio-integrated electronics. *Nature Materials*. **9** (6), 511–517.

Kim J.S., Kuk E., Yu K.N., Kim J.H., Park S.J., Lee H.J., Kim S.H., Park Y.K., Park Y.H., Hwang C.Y., Kim Y.K., Lee Y.S., Jeong D.H. and Cho M.H. (2007) Antimicrobial effects of silver nanoparticles. *Nanomedicine: Nanotechnology, Biology and Medicine*. **3** (1), 95101.

Kipf E., Koch J., Geiger B., Erben J., Richter K., Gescher J., Zengerle R. and Kerzenmacher S. (2013) Systematic screening of carbon-based anode materials for microbial fuel cells with *Shewanella oneidensis* MR-1. *Bioresource technology*. **146** 386–392.

Kippenberger, S., Loitsch, S., Guschel, M., Müller, J., Kaufmann, R. and Bernd, A. 2005. Hypotonic stress induces E-cadherin expression in cultured human keratinocytes. *FEBS letters* **579** (1), 207–14.

Kitching, M., Ramani, M. and Marsili, E. (2014) Fungal biosynthesis of gold nanoparticles: mechanism and scale up. *Microbial Biotechnology*. **8** (6), 904-917.

Krieg, T., Sydow, A., Schröder, U., Schrader, J. and Holtmann D.. (2014) Reactor concepts for bioelectrochemical syntheses and energy conversion. *Trends in biotechnology*. **32** (12), 645–655.

Klis, F.M., de Jong, M., Brul, S. and de Groot, P.W. (2007) Extraction of cell surface-associated proteins from living yeast cells. *Yeast* (Chichester, England). **24** (4), 253–258.

Larios-Rodriguez, Rangel-Ayon, Castillo, Zavala and Herrera-Urbina 2011. Bio-synthesis of gold nanoparticles by human epithelial cells, in vivo. *Nanotechnology*. **22** (35), 355601.

Learman, D.R., Yi, H., Brown, S.D., Martin, S.L., Geesey, G.G., Stevens, A.M. and Hochella, M.F. Jr. (2009) Involvement of *Shewanella oneidensis* MR-1 LuxS in Biofilm Development and Sulfur Metabolism. *Applied and Environmental Microbiology*. **75** (5), 1301–1307.

Lemire, J.A., Harrison, J.J. and Turner, R.J. (2013) Antimicrobial activity of metals: mechanisms, molecular targets and applications. *Nature reviews. Microbiology*. **11** (6), 371–384.

Li, L. and Weng, J (2010). Enzymatic synthesis of gold nanoflowers with trypsin. *Nanotechnology*, **21**.

Li, Q., Lu, B., Zhang, L. and Lu, C. (2012). Synthesis and stability evaluation of size-controlled gold nanoparticles via nonionic fluorosurfactant-assisted hydrogen peroxide reduction. *J. Mater. Chem.* **22**, 13564-13570.

Lilly, B. (2014). We Have Contact: Endothelial Cell-Smooth Muscle Cell Interactions. *Physiology*. **29** (4), 234–241.

Liu, X., Zhang, S., Whitworth, R., Stuart, J. and Chen, M.-S. 2015. Unbalanced Activation of Glutathione Metabolic Pathways Suggests Potential Involvement in Plant Defense against the Gall Midge *Mayetiola destructor* in Wheat. *Scientific Reports*. **5**.

Lo, C.-H., Tsung, T.T. and Lin, H.M. (2007) Preparation of silver nanofluid by the submerged arc nanoparticle synthesis system (SANSS). *Journal of Alloys and Compounds*. **434-435**, 659-662

Logan, B.E., Hamelers, B., Rozendal, R., Schröder, U., Keller, J., Freguia, S., Aelterman, P., Verstraete, W. and Rabaey, K. (2006) Microbial fuel cells: methodology and technology. *Environmental science & technology*. **40** (17), 5181–5192.

Lower, B.H., Shi, L., Yongsunthon, R., Droubay, T.C., McCready, D.E. and Lower, S.K. (2007) Specific Bonds between an Iron Oxide Surface and Outer Membrane Cytochromes MtrC and OmcA from *Shewanella oneidensis* MR-1. *Journal of Bacteriology*. **189** (13), 4944-4952.

Lu, L., Ren, N., Zhao, X., Wang, H., Wi, D. and Xing, D. (2011) Hydrogen production, methanogen inhibition and microbial community structures in psychrophilic single-chamber microbial electrolysis cells. *Energy & Environmental Science*. **4** (4), 1329–1336.

Mackey, M.A., Ali, M.R., Austin, L.A., Near, R.D., El-Sayed, M.A. (2014) The Most Effective Gold Nanorod Size for Plasmonic Photothermal Therapy: Theory and In Vitro Experiments. *The Journal of Physical Chemistry B*. **118** (5), 1319–1326.

Mafuné, F., Kohno, J.Y., Takeda, Y. and Kondow, T. (2001) Formation of Gold Nanoparticles by Laser Ablation in Aqueous Solution of Surfactant. *The Journal of Physical Chemistry B*. **105** (22), 5114–5120.

Majesky, M., Dong, X., Hoglund, V., Mahoney, W. and Daum, G. 2011. The Adventitia: A Dynamic Interface Containing Resident Progenitor Cells. *Arteriosclerosis, Thrombosis, and Vascular Biology*. **31** (7), 1530-1539.

Marsili, E., Baron, D.B., Shikhare, I.D., Coursolle, D., Gralnick, J.A. and Bond, D.R. (2008) *Shewanella* secretes flavins that mediate extracellular electron transfer. *Proceedings of the National Academy of Sciences*. **105** (10), 3968–3973.

Marshall, M.J., Beliaev, A.S., Dohnalkova, A.C., Kennedy, D.W., Shi, L., Wang, Z., Boyanov, M.I., Lai, B., Kemner, K.M., McLean, J.S., Reed, S.B., Culley, D.E., Bailey, V.L., Simonson, C.J., Saffarini, D.A., Romine, M.F., Zachara, J.M. and Fredrickson, J.K. (2006) c-Type Cytochrome-Dependent Formation of U(IV) Nanoparticles by *Shewanella oneidensis*. *PLoS Biology*. **4** (8).

Martínez-Castañón, G., Niño-Martínez, N., Martínez-Gutierrez, F., Martínez-Mendoza, J.R. and Ruiz, F. (2008) Synthesis and antibacterial activity of silver nanoparticles with different sizes. *Journal of Nanoparticle Research*. **10** (8), 1343–1348.

Masih, S. A. (2012) Optimization of power generation in a dual chambered aerated membrane microbial fuel cell with *E. coli* as biocatalyst. *Journal of Scientific & Industrial Research*. **71**, 621–626.

Mathuriya, A. S. & Sharma, V. N. (2009) Bioelectricity production from paper industry waste using a microbial fuel cell by *Clostridium* species . *J Biochem Tech* . **1** (2), 49–52.

Méthy, D., Bertrand, N., Prigent-Tessier, A., Stanimirovic, D., Beley, A. and Marie, C. (2004). Differential MnSOD and HO-1 expression in cerebral endothelial cells in response to sublethal oxidative stress. *Brain research*. **1003**(1-2), 151-158.

Meussen, B.J., de Graaff, L.H., Sanders, J.P. and Weusthuis, R.A. (2012) Metabolic engineering of *Rhizopus oryzae* for the production of platform chemicals. *Applied Microbiology and Biotechnology*. **94** (4), 875–886.

Mishra, A.N, Bhadauria, S., Gaur, M.S. and Pasricha, R. (2010) Extracellular microbial synthesis of gold nanoparticles using fungus *Hormoconis resiniae*. *JOM*. **62** (11), 4548.

Mishra, A., Tripathy, S.K., Wahab, R., Jeong, S.H., Hwang, I., Yang, Y.B., Kim, Y.S., Shin H.S. and Yun, S.I. (2011) Microbial synthesis of gold nanoparticles using the fungus *Penicillium brevicompactum* and their cytotoxic effects against mouse mayo blast cancer C 2 C 12 cells. *Applied microbiology and biotechnology*. **92** (3), 617–630.

Mohanty, S., Mishra, S., Jena, P., Jacob, B., Sarkar, B. and Sonawane, A. (2011) An investigation on the antibacterial, cytotoxic, and antibiofilm efficacy of starch-stabilized silver nanoparticles. *Nanomedicine : nanotechnology, biology, and medicine*. **8** (6), 916–924.

Mukherjee, P., Ahmad, A., Mandal, D., Senapati, S., Sainkar, S.R., Khan, M.I., Ramani, R., Parischa, R., Ajayakumar, P.V., Alam, M., Sastry, M. and Kumar, R. (2001) Bioreduction of AuCl_4^- Ions by the Fungus, *Verticillium* sp. and Surface Trapping of the Gold Nanoparticles Formed. *Angewandte Chemie International Edition*. **40** (19), 3585.

Nadagouda, M. & Varma, R. (2008) Green Synthesis of Ag and Pd Nanospheres, Nanowires, and Nanorods Using Vitamin : Catalytic Polymerisation of Aniline and Pyrrole. *Journal of Nanomaterials*. **2008**.

Narayanan, K. & Sakthivel, N. (2011) Synthesis and characterization of nano-gold composite using *Cylindrocladium floridanum* and its heterogeneous catalysis in the degradation of 4-nitrophenol. *Journal of hazardous materials*. **189** (1-2), 519–525.

Newton, G.J., Mori, S., Nakamura, R., Hashimoto, K. and Watanabe, K. (2009) Analyses of Current-Generating Mechanisms of *Shewanella loihica* PV-4 and *Shewanella oneidensis* MR-1 in Microbial Fuel Cells. *Applied and Environmental Microbiology*. **75** (24), 7674–7681.

Ni, Z., Hou, S., Rton, C. and Vaziri, N. (2004). Lead exposure raises superoxide and hydrogen peroxide in human endothelial and vascular smooth muscle cells. *Kidney International*. **66** (6), 2329–2336.

Onodera, Y., Teramura, T., Takehara, T. and Fukuda, K. (2015) Hyaluronic acid regulates a key redox control factor Nrf2 via phosphorylation of Akt in bovine articular chondrocytes. *FEBS Open Bio*. **5**.

Pandya, S. & Kordesch, M. (2015) Characterization of InSb Nanoparticles Synthesized Using Inert Gas Condensation. *Nanoscale Research Letters*. **10** (1), 258.

Pawar, S.S., Vongkumpeang, T., Grey, C., van Niel, E.W. (2015) Biofilm formation by designed co-cultures of *Caldicellulosiruptor* species as a means to improve hydrogen productivity. *Biotechnology for Biofuels*. **8** (1), 19.

Pham, T.H., Boon, N., De Maeyer, K., Höfte, M., Rabaey, K. and Verstraete, W. (2008) Use of *Pseudomonas* species producing phenazine-based metabolites in the anodes of microbial fuel cells to improve electricity generation. *Applied Microbiology and Biotechnology*. **80** (6), 985–993.

Philip, D. (2009) Biosynthesis of Au, Ag and Au–Ag nanoparticles using edible mushroom extract. *Spectrochimica Acta Part A: Molecular and Biomolecular Spectroscopy*. **73** (2), 374–381.

Pierson, L. & Pierson, E. (2010) Metabolism and function of phenazines in bacteria: impacts on the behavior of bacteria in the environment and biotechnological processes. *Applied Microbiology and Biotechnology*. **86** (6), 1659–1670.

Pineiro, A., Han, D., Shih, W.M. and Yan, H. (2011) Challenges and opportunities for structural DNA nanotechnology. *Nature Nanotechnology*. **6** (12), 763–772.

Pirbadian, S., Barchinger, S.E, Leung, K.M., Byun, H.S., Jangir, Y., Bouhenni, R.A., Reed, S.B., Romine, M.F., Saffarini, D.A., Shi, L., Gorby, Y.A., Golbeck, J.H. and El-Naggar M.Y.. (2014) *Shewanella oneidensis* MR-1 nanowires are outer membrane and

periplasmic extensions of the extracellular electron transport components. Proceedings of the National Academy of Sciences. **111** (35), 12883–12888.

Pissuwan, D., Cortie, C.H., Valenzuela, S.M., Cortie, M.B. (2010) Functionalised gold nanoparticles for controlling pathogenic bacteria. Trends in Biotechnology. **28** (4), 207–213.

Plate, L. & Marletta, M. (2012) Nitric Oxide Modulates Bacterial Biofilm Formation through a Multicomponent Cyclic-di-GMP Signaling Network. Molecular Cell. **46** (4).

Prabhu, S. & Poulouse, E. (2012) Silver nanoparticles: mechanism of antimicrobial action, synthesis, medical applications, and toxicity effects. International Nano Letters. **2** (1), 32.

Qureshi, N., Annous, B.A., Ezeji, T.C., Karcher, P. and Maddox, I.S. (2005) Biofilm reactors for industrial bioconversion processes: employing potential of enhanced reaction rates. Microbial Cell Factories. **4** (1), 24.

Reith, F., Etschmann, B., Grosse, C., Moors, H., Benotmane, M.A., Monsieurs, P., Grass, G., Doonan, C., Vogt, S., Lai, B., Martinez-Criado, G., George, G.N., Nies, D.H., Mergeay, M., Pring, A., Southam, G. and Brugger, J. (2009) Mechanisms of gold biomineralization in the bacterium *Cupriavidus metallidurans*. Proceedings of the National Academy of Sciences. **106** (42), 17757–17762.

Rogers, K.R., Bradham, K., Tolaymat, T., Thomas, D.J., Hartmann, T., Ma, L. and Williams, A. (2012) Alterations in physical state of silver nanoparticles exposed to synthetic human stomach fluid. The Science of the total environment. **420**, 334–339.

Roldán, M, Pellegrini, N and de Sanctis, O. (2013) Electrochemical Method for Ag-PEG Nanoparticles Synthesis. Journal of Nanoparticles. **2013**.

Romero, R. B. & Lamas, S. (2014) Hydrogen peroxide signaling in vascular endothelial cells. Redox Biology. **2**.

- Rosche, B., Li, X.Z., Hauer, B., Schmid, A. and Buehler, K. (2009) Microbial biofilms: a concept for industrial catalysis? *Trends in Biotechnology*. **27** (11), 636-643.
- Rosenbaum, M., Cotta, M.A. and Angenent, LT. (2010) Aerated *Shewanella oneidensis* in continuously fed bioelectrochemical systems for power and hydrogen production. *Biotechnology and Bioengineering*. **105** (5), 880–888.
- Ross, D., Flynn J.M., Baron, D.B., Gralnick, J.A. and Bond, D.R. (2011). Towards Electrosynthesis in *Shewanella*: Energetics of Reversing the Mtr Pathway for Reductive Metabolism. *PLoS ONE*. **6** (2).
- Rozendal, R., Leone, E., Keller, J. and Rabaey, K. (2009) Efficient hydrogen peroxide generation from organic matter in a bioelectrochemical system. *Electrochemistry Communications*. **11** (9), 1752-1755.
- Saha, K., Agasti S.S., Kim, C., Li, X. and Rotello, V.M. (2012) Gold Nanoparticles in Chemical and Biological Sensing. *Chemical Reviews*. **112** (5), 2739–2779.
- Sakai, S. & Yagishita, T. (2007) Microbial production of hydrogen and ethanol from glycerol-containing wastes discharged from a biodiesel fuel production plant in a bioelectrochemical reactor with thionine. *Biotechnology and Bioengineering*. **98** (2), 340–348.
- Salehi-Khojin, A, Jhong, H.R.M, Rosen, B.A, Zhu, W. Ma, S., Kenis, P.J.A and Masel, R.I. (2013) Nanoparticle Silver Catalysts That Show Enhanced Activity for Carbon Dioxide Electrolysis. *The Journal of Physical Chemistry C*. **117** (4), 16271632.
- Sanghi, R., Verma, P. and Puri, S. (2011) Enzymatic Formation of Gold Nanoparticles Using *Phanerochaete Chrysosporium*. *Advances in Chemical Engineering and Science*. **1** (3), 154-162.
- Santos, K., Elias, W., Signori, A.M., Giacomelli, F.C., Yang, H., and Domingos, J.B. (2012) Synthesis and Catalytic Properties of Silver Nanoparticle–Linear Polyethylene Imine Colloidal Systems. *The Journal of Physical Chemistry C*. **116** (7), 4594-4604.

Sarkar, J., Ray, S., Chattopadhyay, D., Laskar, A. and Acharya, K. (2011) Mycogenesis of gold nanoparticles using a phytopathogen *Alternaria alternata*. *Bioprocess and Biosystems Engineering*. **35** (4), 637–643.

Sasaki, K., Morita, M., Sasaki, D., Matsumoto, N., Ohmura, N. and Igarashi, Y. (2012) Single-chamber bioelectrochemical hydrogen fermentation from garbage slurry. *Biochemical Engineering Journal*. **68**, 104 -108.

Sasaki, K., Morita, M., Sasaki, D., Ohmura, N. and Igarashi, Y. (2012) The membraneless bioelectrochemical reactor stimulates hydrogen fermentation by inhibiting methanogenic archaea. *Applied Microbiology and Biotechnology*. **97** (15), 7005-7013.

Shankar, S.S, Ahmad, A., Pasricha, R. and Sastry, M. (2003) Bioreduction of chloroaurate ions by geranium leaves and its endophytic fungus yields gold nanoparticles of different shapes. *Journal of Materials Chemistry*. **13** (7), 1822.

Shao, Y., Wang, J., Wu, H., Liu, J., Aksay, I.A. and Lim, Y. (2010) Graphene Based Electrochemical Sensors and Biosensors: A Review. *Electroanalysis*. **22** (10), 1027–1036.

Sheikhloo, Z., Salouti, M. and Katiraei, F. (2011) Biological Synthesis of Gold Nanoparticles by Fungus *Epicoccum nigrum*. *Journal of Cluster Science*. **22** (4), 661665.

Shi, C., Zhu, N., Cao, Y. and Wu, P. (2015) Biosynthesis of gold nanoparticles assisted by the intracellular protein extract of *Pycnoporus sanguineus* and its catalysis in degradation of 4-nitroaniline. *Nanoscale Research Letters*. **10** (1), 147.

Shi, L., Chen, B., Wang, Z., Elias, D.A., Mayer, M.U., Gorby, Y.A., Ni, S., Lower, B.H., Kennedy, D.W., Wunschel, D.S., Mottaz, H.M., Marshall, M.J., Hill, E.A., Beliaev, A.S., Zachara, J.M., Fredrickson, J.K. and Squier, T.C. (2006) Isolation of a High-Affinity Functional Protein Complex between OmcA and MtrC: Two Outer Membrane Decaheme c-Type Cytochromes of *Shewanella oneidensis* MR-1. *Journal of Bacteriology*. **188** (13), 47054714.

Shi, L. Richardson, D.J., Wang, Z., Kerisit, S.N., Rosso, K.M., Zachara, J.M. and Fredrickson, J.K. (2009) The roles of outer membrane cytochromes of *Shewanella* and *Geobacter* in extracellular electron transfer. *Environmental Microbiology Reports*. **1** (4), 220–227.

Singaravelan, R. & Alwar, S. (2015) Electrochemical synthesis, characterisation and phyto-genic properties of silver nanoparticles. *Applied Nanoscience*. **5** (8), 983-991.

Singh, N. & Khanna, P. (2007) In situ synthesis of silver nano-particles in polymethylmethacrylate. *Materials Chemistry and Physics*. **104** (2-3), 367-372.

Singh, R., Paul, D. and Jain, R.K. (2006) Biofilms: implications in bioremediation. *Trends in microbiology*. **14** (9), 389–397.

Slocik, J., Naik, R.R., Stone, M.O. and Wright, D.W. (2004) Viral templates for gold nanoparticle synthesis. *Journal of Materials Chemistry*. **15** (7), 749.

Starowicz, M., Stypula, B. and Banaś, J. (2006) Electrochemical synthesis of silver nanoparticles. *Electrochemistry Communications*. **8** (2), 227230.

Storhoff, J. J., Marla, S.S., Bao, P., Hagenow, S., Mehta, H., Lucas, A., Garimella, V., Patno, T., Buckingham, W., Cork, W. and Müller U.R. (2004) Gold nanoparticle-based detection of genomic DNA targets on microarrays using a novel optical detection system. *Biosensors and Bioelectronics*. **19** (8), 875–883.

Sun, M.-Y., Yang, J., Lin, T. and Du, X.W. (2012) Facile synthesis of SnS hollow nanoparticles via laser ablation followed by chemical etching. *RSC Advances*. **2** (20), 7824–7828.

Suresh, A., Yang, J., Lin, T. and Du, X.W. (2011) Biofabrication of discrete spherical gold nanoparticles using the metal-reducing bacterium *Shewanella oneidensis*. *Acta biomaterialia*. **7** (5), 2148–2152.

Suresh, A., Doktycz, M.J., Wang, W., Moon, J.W., Gu, B., Meyer, H.M. 3rd, Hensley D.K., Allison, D.P., Phelps, T.J. and Pelletier, D.A. (2011) Monodispersed biocompatible silver sulfide nanoparticles: facile extracellular biosynthesis using the γ -proteobacterium, *Shewanella oneidensis*. *Acta biomaterialia*. **7** (12), 4253–4258.

Suresh, A., Pelletier, D.A., Wang, W., Moon, J.W., Gu, B., Mortensen, N.P., Allison, D.P., Joy, D.C., Phelps, T.J. and Doktycz, M.J. (2010) Silver nanocrystallites: biofabrication using *Shewanella oneidensis*, and an evaluation of their comparative toxicity on gram-negative and gram-positive bacteria. *Environmental science & technology*. **44** (13), 5210–5215.

Syed, A. & Ahmad, A. (2012) Extracellular biosynthesis of platinum nanoparticles using the fungus *Fusarium oxysporum*. *Colloids and surfaces. B, Biointerfaces*. **97**, 27-31.

Takahashi, K., Tatsunami, R., Oba, T. and Tampo, Y. (2010). Buthionine Sulfoximine Promotes Methylglyoxal-Induced Apoptotic Cell Death and Oxidative Stress in Endothelial Cells. *Biological and Pharmaceutical Bulletin*. **33** (4), 556–560.

Tigges, U., Komatsu, M. and Stallcup, W.B. (2012). Adventitial Pericyte Progenitor/Mesenchymal Stem Cells Participate in the Restenotic Response to Arterial Injury. *Journal of Vascular Research*. **50** (2), 134–144.

Thormann, K. M., Saville, R.M., Shukla, S., Pelletier, D.A. and Spormann, A.M. (2004) Initial Phases of Biofilm Formation in *Shewanella oneidensis* MR-1. *Journal of Bacteriology*. **186** (23), 8096–8104.

Tsaryk, R., Kalbacova, M., Hempel, U., Scharnweber, D., Unger, R.E., Dieter, P., Kirkpatrick, C.J. and Peters, K. (2007). Response of human endothelial cells to oxidative stress on Ti6Al4V alloy. *Biomaterials*. **28** (5) 806-813.

Tseng, K.-H., Chen, Y.C. and Shyue, J.J. (2010) Continuous synthesis of colloidal silver nanoparticles by electrochemical discharge in aqueous solutions. *Journal of Nanoparticle Research*. **13** (5), 1865-1872.

Villano, M., Aulenta, F. and Majone, M. (2012) Perspectives of biofuels production from renewable resources with bioelectrochemical systems. *Asia-Pacific Journal of Chemical Engineering*. **7** (S3), S263–S274.

Wang, H., Law N., Pearson, G., van Dongen, B.E., Jarvis, R.M., Goodacre, R. and Lloyd, J.R. (2009) Impact of silver(I) on the metabolism of *Shewanella oneidensis*. *Journal of bacteriology*. **192** (4), 1143–1150.

Wang, J., Zhang, G., Li, Q., Jiang, H., Liu, C., Amatore, C. and Wang, X. (2013). In vivo self-bio-imaging of tumors through in situ biosynthesized fluorescent gold nanoclusters. *Scientific Reports*. **3**, 1157.

Wang, J., Dong, B., Chen, B., Jiang, Z. and Song, H. (2012) Selective photothermal therapy for breast cancer with targeting peptide modified gold nanorods. *Dalton Transactions*. **41** (36), 11134–11144.

Wang, X., Liu, L.H., Ramström, O. and Yan, M. (2009) Engineering Nanomaterial Surfaces for Biomedical Applications. *Experimental Biology and Medicine*. **234** (10), 1128-1139.

Wei, H., Wang, Z., Zhang, J., House, S., Gao, Y.-G., Yang, L., Robinson, H., Tan, L., Xing, H., Hou, C., Robertson, I., Zuo, J.-M. and Lu, Y. 2011. Time-dependent, protein-directed growth of gold nanoparticles within a single crystal of lysozyme. *Nature nanotechnology*. **6** (2),93–97.

Whitesides, G. M. (2005) Nanoscience, Nanotechnology, and Chemistry. *Small*. **1** (2), 172–179.

Windt, W. , Aelterman, P. and Verstraete, W. (2005) Bioreductive deposition of palladium (0) nanoparticles on *Shewanella oneidensis* with catalytic activity towards reductive dechlorination of polychlorinated biphenyls. *Environmental Microbiology*. **7** (3), 314–325.

- Wu, R., Cui, L., Chen, L., Wang, C., Cao, C. Sheng, G., Yu, H. and Zhao, F. (2013) Effects of Bio-Au Nanoparticles on Electrochemical Activity of *Shewanella oneidensis* Wild Type and Δ omcA/mtrC Mutant. *Scientific Reports*. **3**
- Wu, X., Zhao, F., Rahunen, N., Varcoe, J.R., Avignone-Rossa, C., Thumser, A.E., and Slade, R.C. (2011) A Role for Microbial Palladium Nanoparticles in Extracellular Electron Transfer. *Angewandte Chemie International Edition*. **50** (2), 427–430. 3
- Xu, B. , Jahic, M., Blomsten, G., Enfors, S.O. (1999) Glucose overflow metabolism and mixed acid fermentation in aerobic large scale fed batch processes with *E. coli*. *Appl Microbiol Biotechnol.* **51** (5), 564–571.
- Yan, L., Zhang, S., Chen, P., Liu, H., Yin, H. and Li, H. (2012) Magnetotactic bacteria, magnetosomes and their application. *Microbiological Research*. **167** (9), 507-509.
- Young, J. (2003) Biomineralization Within Vesicles: The Calcite of Coccoliths. *Reviews in Mineralogy and Geochemistry*. **54** (1), 189–215.
- Yong J., Min S., Yao Z., Guoqiang Z., Yong T. and Daping L. (2013) Bioelectrochemical systems for simultaneously production of methane and acetate from carbon dioxide at relatively high rate. *International Journal of Hydrogen Energy*. **38** (8), 3497-3502.
- Zhan, G., Li, D., Tao, Y., Zhu, X., Zhang, L., Wang, Y. and He, Y. (2014) Ammonia as carbon-free substrate for hydrogen production in bioelectrochemical systems. *International Journal of Hydrogen Energy*. **39** (23), 11854-11859.
- Zhang, X., He, X., Wang, K. and Yang, X. (2011) Different Active Biomolecules Involved in Biosynthesis of Gold Nanoparticles by Three Fungus Species. *J. Biomed Nanotechnol.* **7** (2), 245–254.

Appendices

Appendix 1 Visit to Singapore Centre on Life Science Engineering

In the first year of this PhD project, I was a visiting student in the Singapore Centre on Life Science Engineering in Nanyang Technology University, Singapore for three months. During my visit, I was trained in basic electrochemical techniques and nanoparticle biosynthesis by both my external supervisor Dr. Enrico Marsili and Assistant Prof. Cao Bin. Also I began the preliminary work in the bioelectrochemical synthesis of silver nanoparticles (see Chapter 3), where I investigated the effect of electrochemical potential on the biosynthesis of silver nanoparticles by *Shewanella oneidensis* MR-1 biofilms grown on carbon felt working electrodes.

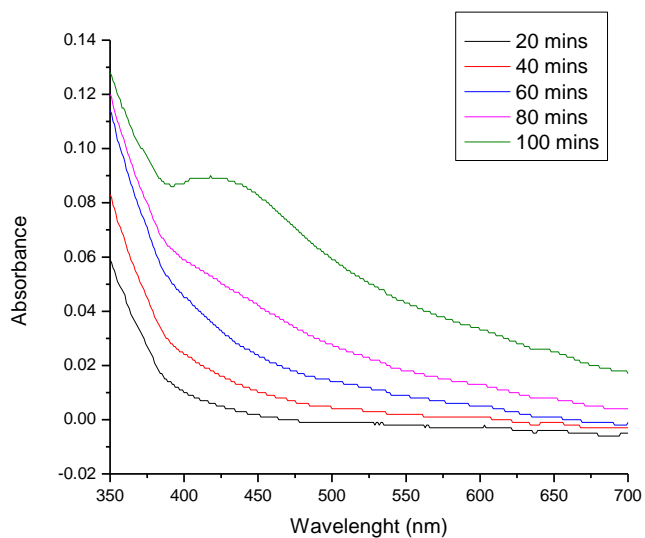
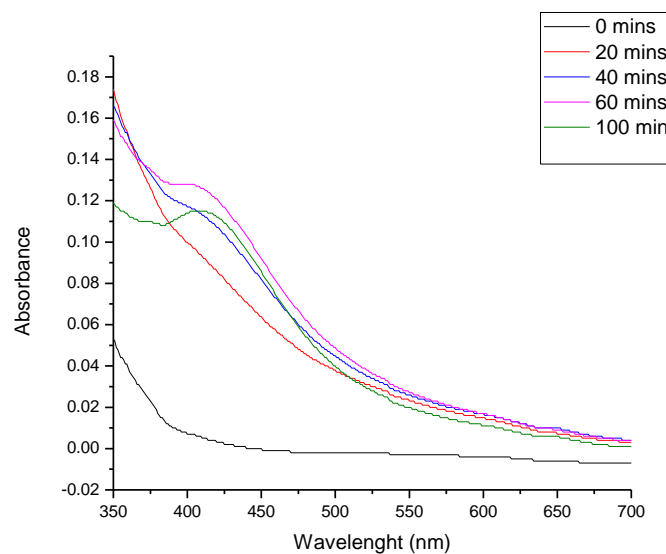
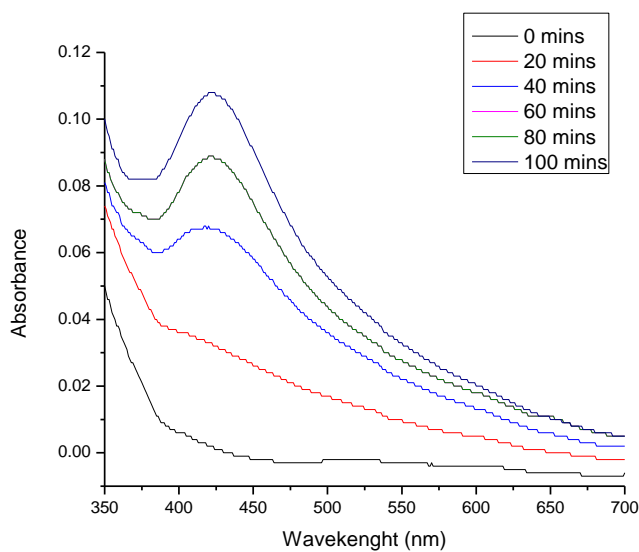
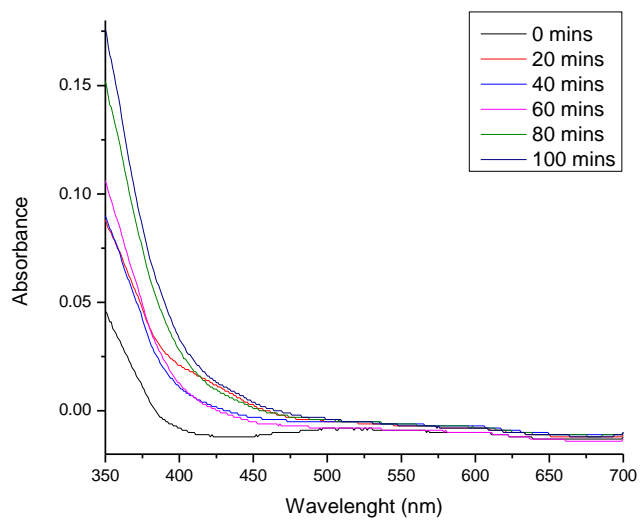
A**B****C****D**

Figure 1: UV visible spectra of 10mM HEPES buffer with 1M Ag⁺ at 30°C with a young *Shewanella oneidensis* biofilm in a bio-electrochemical cell at (a) 0V, (b) -0.2V, (c) -0.4V and (d) -0.6V over the course of 100 mins.

Appendix 2 Materials and Regents

All chemicals (Table 2.3), cell culture reagents (Table 2.4) , assay kits (Table 2.5) and primers used (Table 2.4) were of the highest quality available, expiry date routinely checked before use and cell culture grade where appropriate.

Table 2.3: Chemicals used and their suppliers

Chemicals	Supplier
Agar	Oxoid
Aluminum potassium sulphate	Acros Organics
Aminobenzoic acid	Fluka
Ammonia chloride	Fisher
Arginine	Lancaster
Biotin	Acros Organics
B nicotinic acid	Acros Organics
Boric acid	Acros Organics
Bovine Serum Albumin	Sigma Aldrich
Calcium chloride	Merck
Colbalt chloride	Sigma Aldrich
Copper sulphate	Sigma Aldrich
DAPI	Sigma Aldrich
Dextrose	Santa Cruz
Dithiothreitol	Thermo Scientific
Dimethyl sulfoxide	BDH Chemicals
d-pantothenic acid	Fisher
Folic acid	Acros Organics
Glutaraldehyde	Sigma Aldrich
Glutamine	Merck
Glycerol	Fisher
Hydrochloric acid	Fisher
HEPEs	Santa Cruz
Hydrogen tetrachloaurate trihydrate	Fisher
Iron citrate	Fisher
Iron sulphate	Fisher
Magnessium sulphate	BDH Chemicals

Manganese sulphate	BDH Chemicals
Nitilotriacetic acid	Fisher
Nitric acid	Fisher
Phosphate buffer saline tablets	Fisher
Phosphate buffer tablets	Fisher
Potassium chloride	Fisher
Potato extract	Sigma Aldrich
Pyridoxine	Acros Organics
Riboflavin	Acros Organics
SDS	Santa Cruz
Serine	Merck
Silver nitrite	Fisher
Sodium chloride	Fisher
Sodium dihydrogen phosphate	Merck
Sodium hydroxide	Merck
Sodium lactate (60% w/w)	Fisher
Sodium molybdate	Acros Organics
Sodium tungstate	Fisher
Thiamine HCl hydrate	Acros Organics
Thioctic acid	Acros Organics
Tris-HCl	Sigma Aldrich
Triton X-100	Fisher
Tryptone	Sigma Aldrich
Yeast extract	Oxoid
Zinc chloride	Acros

Table 2.3: Cell Culture Reagents

Reagent	Supplier
FBS	Sigma Aldrich
Penicillin/streptomycin cocktail	Sigma Aldrich
RPMI 1640	Sigma Aldrich
DMEM	Sigma Aldrich
Trypsin 10X	Sigma Aldrich

Table 2.4: Assay kits

	Supplier
BCA assay	Pierce
ROS Glo Oxidative Stress assay	Promega